Sodium Magnetic Resonance Imaging at 9.4 Tesla

Dissertation

der Mathematisch-Naturwissenschaftlichen Fakultät

der Eberhard Karls Universität Tübingen

zur Erlangung des Grades eines

Doktors der Naturwissenschaften

(Dr. rer. nat.)

vorgelegt von

Christian Carlo Mirkes

aus Luxemburg / Luxemburg

Tübingen

2015

Gedruckt mit Genehmigung der Mathematisch-Naturwissenschaftlichen Fakultät der Eberhard Karls Universität Tübingen.

Tag der mündlichen Qualifikation:	15.12.2015
Dekan:	Prof. Dr. Wolfgang Rosenstiel
1. Berichterstatter:	Prof. Dr. Klaus Scheffler
2. Berichterstatter:	Prof. Dr. Reinhold Kleiner

TABLE OF CONTENTS

1 SUMMARY

The motivation to perform magnetic resonance imaging (MRI) at ultra-high field strength (UHF) ($B_0 \geq 7$ Tesla) is primarily driven by the increased sensitivity compared to low field MRI. This is especially true for nuclei which exhibit intrinsically a low signal-to-noise ratio (SNR) either due to their physical properties or their small in vivo concentrations. The aim of this thesis was to establish the measurement techniques required for sodium magnetic resonance imaging at 9.4 Tesla and to overcome some of the limitations faced at lower field strengths. For this purpose, the hardware as well as the software used for the acquisition of the MR signal were designed and adapted to each other with great care in order to harness the full potential offered by UHF MRI.

In the first part of this thesis, a novel coil setup consisting of a single-tuned sodium birdcage coil and a proton patch antenna was used to acquire high-resolution quantitative sodium images of several healthy volunteers. This setup provided a satisfactory sensitivity at the sodium frequency and offered at the same time the possibility to acquire the proton signal for anatomical localization and B_0 shimming. Correction methods for inhomogeneities of the B_0 and radio-frequency (RF) transmit field (B_1) were implemented and partial volume effects were mitigated by the reduced voxel size, which enabled a more accurate quantification of the sodium concentration in the human brain. However, the spatial resolution was insufficient to completely avoid quantifications errors at tissue boundaries, although the achieved sensitivity was considerably higher compared to previous studies.

The second part of the thesis focused on further increasing the sensitivity of the coil setup at the sodium frequency without sacrificing the proton imaging capability. The final coil design was made up of an assembly of three coils arranged in layers. The innermost layer consisted of a multi-channel receiver array to boost the sensitivity for sodium imaging. The middle layer comprised the sodium transmit array and the outer layer was formed by a dipole array to

enable proton imaging. It could be shown that the proposed coil setup possessed all the required features needed for efficient multi-nuclear MRI at UHF and enabled the acquisition of sodium images having a quality not previously achieved.

In the last part of the thesis, the high sensitivity provided by the multi-channel coil array and the strong static magnetic field was used to perform sodium triple quantum filtered (TQF) imaging, which is known to be an SNR-critical application. The latter allows differentiating between intra- and extracellular sodium, which might be valuable information for disease diagnosis and monitoring. Apart from the low SNR, the high power deposition rates associated with this type of imaging technique are challenging, especially at UHF. To overcome this problem, at least partially, a modulation of the flip angles of the TQ preparation module was proposed and shown to improve the sensitivity by about 20%.

2 ZUSAMMENFASSUNG

Das Bestreben Magnetresonanztomographie (MRT) bei ultra-hohen Feldstärken (UHF) ($B_0 \geq 7$ Tesla) durchzuführen kann in erster Linie mit der deutlich erhöhten MR-Empfindlichkeit im Gegensatz zu niedrigeren Feldstärken erklärt werden. Dies gilt insbesondere für die Bildgebung mit Kernen, die an sich schon ein niedriges Signal-Rausch-Verhältnis (SNR) ausweisen; dies entweder aufgrund ihrer physikalischen Eigenschaften oder ihrer geringen In-vivo-Konzentrationen. Das Ziel dieser Arbeit war es die erforderlichen Messverfahren für die Natriumbildgebung bei 9,4 Tesla zu erarbeiten und einige Einschränkungen, die bei niedrigeren Feldstärken auftreten, zu überwinden. Zu diesem Zweck wurde maßgeschneiderte Hard- und Software für die Erfassung des MR-Signals entwickelt und aufeinander abgestimmt um das volle Potential, das UHF-MRT bietet, zu nutzen.

Im ersten Teil der Arbeit wurde ein neuartiger Spulenaufbau, bestehend aus einer mono-resonanten Natrium-Birdcage-Spule und einer Protonen-Patch-Antenne, verwendet um hochauflösende quantitative Natriumbilder von mehreren gesunden Probanden aufzunehmen. Dieser Aufbau stellte eine zufriedenstellende Empfindlichkeit bei der Natriumfrequenz sicher und bot gleichzeitig die Möglichkeit das Protonensignal für anatomische Lokalisation und B_0-Shimming zu nutzen. Korrekturverfahren wurden implementiert und angewendet um Inhomogenitäten des B_0 und Radiofrequenz- (RF) Feldes (B_1) entgegenzuwirken. Durch die Reduzierung der Voxelgröße konnten Partialvolumeneffekte gemindert und eine genauere Quantifizierung der Natriumkonzentration im menschlichen Gehirn erreicht werden. Jedoch war die erreichte räumliche Auflösung unzureichend um Quantifizierungsfehler an Gewebegrenzen gänzlich zu vermeiden, obwohl die erzielte Empfindlichkeit deutlich höher war als bei vorhergehenden Studien.

Der zweite Teil der Arbeit konzentrierte sich auf eine weitere Erhöhung der Empfindlichkeit des Spulenaufbaus für die Natriumbildgebung ohne dabei die Möglichkeit der Protonenbildgebung zu verlieren. Der endgültige Messaufbau bestand aus drei in Schichten

angeordneten Spulen. Die innerste Schicht bildete eine Mehrkanalempfangsanordnung, welche eine möglichst hohe Empfindlichkeit für das Natriumsignal gewährleisten sollte. Die Natriumsendespule stellte die mittlere Schicht dar. Eine Dipolantennenanordnung bildete die äußerste Schicht und wurde für die Protonenbildgebung benutzt. Es konnte gezeigt werden, dass der vorgeschlagene Spulenaufbau alle erforderlichen Funktionen besitzt, die für eine effiziente Mehrkern-MRT-Messung bei ultra-hohem Feld benötig werden, und es erlaubt Natriumbilder mit einer vorher unerreichten Qualität aufzunehmen.

Im letzten Teil der Arbeit wurde die hohe MR-Empfindlichkeit, resultierend aus der Verwendung einer Mehrkanalspule und eines starken statischen Magnetfeldes, genutzt um Tripelquanten (TQ)-Kohärenzen zu messen, welche nur ein sehr geringes SNR aufweisen. Tripelquanten-gefilterte (TQF) Bilder ermöglichen die Unterscheidung zwischen intra- und extrazellulären Natrium und können möglicherweise wertvolle Informationen für die Diagnose und Überwachung von Krankheiten liefern. Abgesehen von dem niedrigen SNR, bereiten die hohen RF-Sendeleistungen, die für diese Bildgebungstechnik benötigt werden, Probleme insbesondere bei UHF. Um dieses Problem zumindest teilweise zu mindern wurde eine Modulation der Flipwinkel, welche die TQ-Kohärenzen erzeugen, vorgeschlagen und gezeigt, dass sich so die Sensitivität der TQ Sequenz um etwa 20% steigern lässt.

3 LIST OF PUBLICATIONS

This doctoral thesis is written as an integrated accumulation of publications, which are appended at the very end of this work.

3.1 Summarized publications

Publication 1:

Mirkes CC, Hoffmann J, Shajan G, Pohmann R, and Scheffler K

High-resolution quantitative sodium imaging at 9.4 Tesla.

Magn Reson Med, 2015, 73: 342–351.

Publication 2:

Shajan G, **Mirkes C**, Buckenmaier K, Hoffmann J, Pohmann R, and Scheffler K

Three-layered radio frequency coil arrangement for sodium MRI of the human brain at 9.4 Tesla.

Magn Reson Med, 2015, doi: 10.1002/mrm.25666

Publication 3:

Mirkes C, Shajan G, Bause J, Buckenmaier K, Hoffmann J, and Klaus Scheffler

Triple-Quantum-Filtered Sodium Imaging at 9.4 Tesla.

Magn Reson Med, 2015, doi: 10.1002/mrm.25688

3.2 Other publications

Publication 4:

Romanzetti S, **Mirkes CC**, Fiege D, Celik A, Felder J, and Shah NJ

Mapping tissue sodium concentration in the human brain: A comparison of MR sequences at 9.4 Tesla.

NeuroImage, 2014, 96: 44–53.

Publication 5:

Hoffmann J, **Mirkes C**, Shajan G, Scheffler K, and Pohmann R

Combination of a multimode antenna and TIAMO for traveling-wave imaging at 9.4 Tesla.

Magn Reson Med, 2015, doi: 10.1002/mrm.25614

Publication 6:

Heule R, Bär P, **Mirkes C**, Scheffler K, Trattnig S, *and* Bieri O

Triple-echo steady-state T_2 relaxometry of the human brain at high to ultra-high fields.

NMR in Biomedicine, 2015, 27*:* 1037–1045.

Publication 7:

Bause J, Ehses P, **Mirkes C**, Shajan G, Scheffler K, and Pohmann R

Quantitative and Functional Pulsed Arterial Spin Labeling in the Human Brain at 9.4 T.

Magn Reson Med, 2015, doi: 10.1002/mrm.25671

Publication 8:

Christian Mirkes, Štefan Zbýň, Grzegorz Chadzynski, Siegfried Trattnig, and Klaus Scheffler

Book chapter: ^{23}Na MRI.

Encyclopedia of Spectroscopy and Spectrometry, 3rd Edition. Elsevier Ltd. [in press]

4 INTRODUCTION

A short summary of the basics of (sodium) MRI is given in the following chapter. A more detailed description can be found for example in (1,2).

4.1 MRI basics

Magnetic resonance imaging is a powerful diagnostic tool commonly used in radiology. In contrast to other imaging techniques such as computed tomography (CT) or positron emission tomography (PET), it does not use any ionizing radiation. Instead, MRI relies on creating a net spin polarization with a strong static external magnetic field and the manipulation of the resulting magnetization with radio frequency and magnetic gradient fields.

Nuclei with a non-zero nuclear spin $\vec{S}$ are a prerequisite for MRI. According to the quantization rules postulated by quantum mechanics, the projection of the spin $\vec{S}$ onto an axis, say the z-axis, can only take $(2s+1)$ discrete values (3):

$$S_z = \hbar m_s, \quad \text{with} \quad m_s = -s, -s+1, \ldots, s-1, s \tag{4.1}$$

where s is the spin quantum number and $\hbar$ the reduced Planck constant. The nuclear magnetic moment is proportional to the spin angular momentum and given by:

$$\vec{\mu} = \gamma \vec{S}, \tag{4.2}$$

where γ is the gyromagnetic ratio. In the absence of an external field, the $(2s+1)$ eigenstates of the angular momentum are degenerate. If the nucleus is placed in a static magnetic field, e.g. $\overrightarrow{B_0} = B_0 \cdot \vec{z}$, the Zeeman splitting lifts this degeneracy. The energy difference between two adjacent eigenstates is then given by:

$$\Delta E = \gamma \hbar B_0 = \hbar \omega_0, \tag{4.3}$$

where ω_0 is the Larmor frequency. The actual state of a spin will generally be a superposition of all possible eigenstates and the expectation value of the magnetization vector $\langle \vec{\mu} \rangle$ will be time-depend and precess with the Larmor frequency about the direction of the external field:

$$\frac{d\langle\vec{\mu}\rangle}{dt} = \gamma B_0 \langle\vec{\mu}\rangle \times \vec{z} = \omega_0 \langle\vec{\mu}\rangle \times \vec{z}. \tag{4.4}$$

In case of MRI, the net magnetization $\vec{M}$ of an entire spin ensemble for a volume V is measured:

$$\vec{M} = \frac{1}{V}\sum_i \langle\vec{\mu_i}\rangle. \tag{4.5}$$

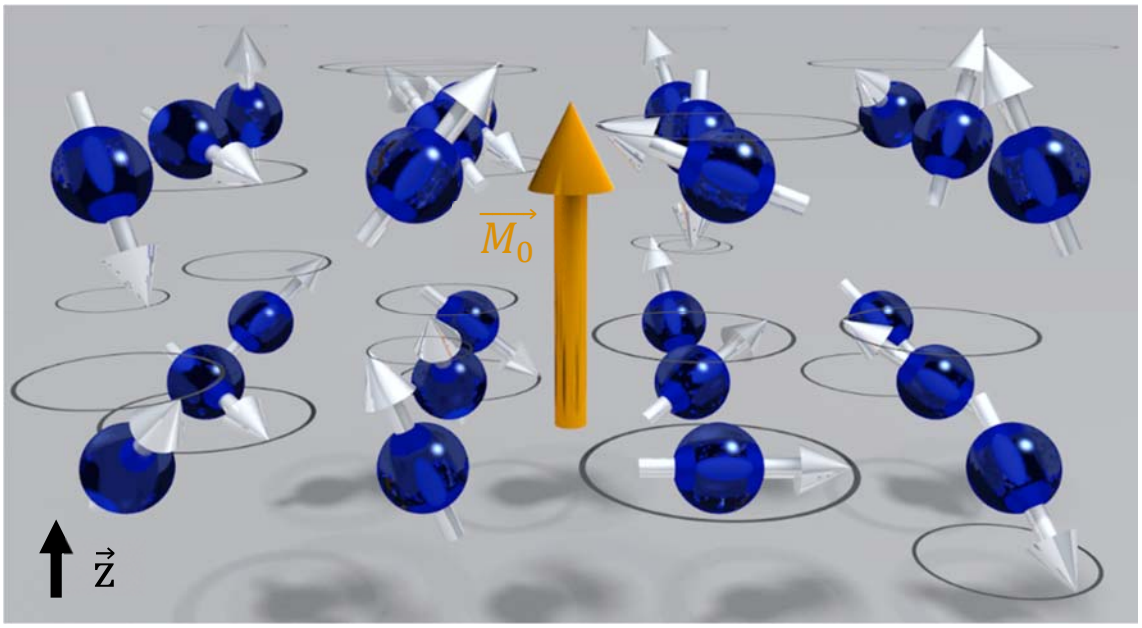

Figure 4-1. Precession of individual spins about an external magnetic field (B_0) parallel to the z-axis. The slight tendency of the spins to align with B_0 creates a net longitudinal magnetization (M_0). The total transverse magnetization is zero due to the incoherent precession.

It should be noted that "an MR measurement does not make the state of an ensemble collapse into single-particle eigenstates" (4). Hence each individual nucleus is not forced to be in one of the $(2s + 1)$ eigenstates. The distribution of the angular spin orientations can be described by the Boltzmann statistics and is more or less spherically symmetric because the thermal energies are large for the considered temperature range (body temperature: T = 310 K) compared to the energies associated with the spin orientation in the magnetic field. As a consequence, there is only a slight tendency of the spins to align with the external field (Figure 4-1). Yet, in most cases, the number of nuclei contained in a voxel (i.e. volume element) is so large that a useable longitudinal magnetization is created. The net transverse magnetization is zero due to the incoherent precession of the spins. It can be shown that the value of the longitudinal magnetization (M_0) in thermal equilibrium is proportional to B_0 (1) which provides a motivation for UHF MRI:

$$M_0 \cong \varrho_0 \frac{s(s+1)\gamma^2\hbar^2}{3k_B T} B_0, \qquad (\hbar\omega_0 \ll k_B T) \tag{4.6}$$

where ϱ_0 is the spin density and k_B the Boltzmann constant.

The longitudinal magnetization created by the spin polarization is not measured as such since the magnetic polarization associated with the electrons is several orders of magnitude larger (2). Instead, a time-dependent RF field with an angular frequency ω_0 is applied perpendicularly to B_0 (Figure 4-2a/b). This additional field produces a torque tilting the net magnetization from its equilibrium position into the transverse plane. The transverse magnetization (M_{xy}), which is precessing with the Larmor frequency as well, generates an alternating magnetic flux density, which can induce an electromotive force in a coil oriented parallel to the main static magnetic field.

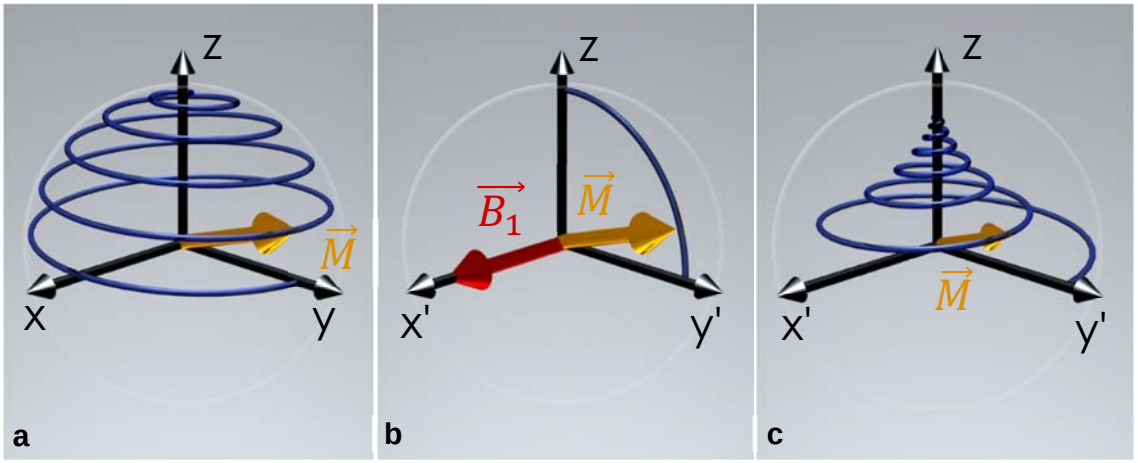

Figure 4-2. a: The longitudinal magnetization can be rotated into the transverse plane with an additional time-dependent magnetic field (B_1) which is perpendicular to B_0. In the laboratory frame the transverse magnetization precesses with ω_0 about the z-axis. **b:** In a frame rotating with ω_0, the B_1 field-vector is stationary and exerts a torque on the magnetization which is flipped into the transverse plane. **c:** Return of the magnetization into thermal equilibrium after an RF excitation in the laboratory frame.

Assuming for now that the magnetization is not returning to its equilibrium state through relaxation processes, the signal measured with a coil having a homogenous receive profile is obtained by integrating over the sample:

$$S(t) = \iiint M_{xy}(x,y,z)e^{-i\varphi(t,x,y,z)}\,dx\,dy\,dz, \tag{4.7}$$

where φ is the time- and position-dependent phase of the signal. The rate of change of the signal phase is equivalent to an angular frequency and given by:

$$\frac{d\varphi(t,x,y,z)}{dt} = \omega(t,x,y,z) = \gamma B_z(t,x,y,z), \tag{4.8}$$

where B_z is the sum of the main magnetic field and the contributions from time-varying magnetic field gradients $G_i(t)$ produced by additional coils fixed inside the scanner bore:

$$B_z(t,x,y,z) = B_0 + G_x(t)x + G_y(t)y + G_z(t)z. \tag{4.9}$$

Substitution of (4.9) into (4.8) and integration over time yields:

$$\varphi(t,x,y,z) = \gamma \int_0^t B_0\, d\tau + \gamma\left[\int_0^t G_x(\tau)\, d\tau\right] x + \gamma\left[\int_0^t G_y(\tau)\, d\tau\right] y + \gamma\left[\int_0^t G_z(\tau)\, d\tau\right] z. \quad (4.10)$$

Using the following abbreviations to define k-space

$$k_{x,y,z}(t) = \frac{\gamma}{2\pi}\int_0^t G_{x,y,z}(\tau)\, d\tau, \quad (4.11)$$

and passing over to the rotating frame, equation 4.7 becomes:

$$S(t) = \iiint M_{xy}\,(x,y,z) e^{-i2\pi k_x(t)}\, e^{-i2\pi k_y(t)} e^{-i2\pi k_z(t)}\, dx\, dy\, dz. \quad (4.12)$$

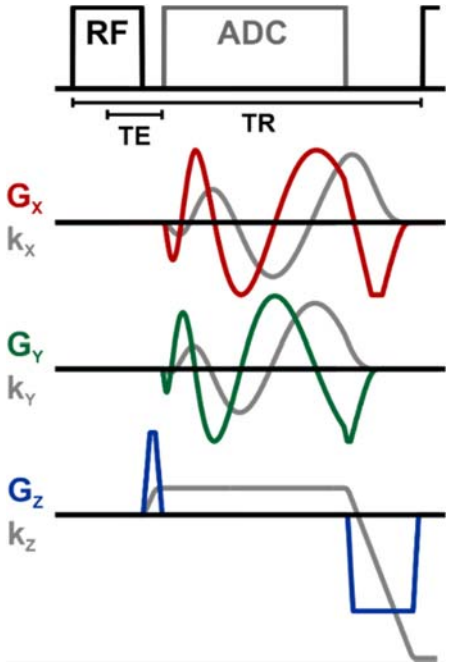

Figure 4-3. Basic sequence diagram showing the timing of the RF pulse, the analogue-to-digital converter (ADC), and the gradients. In this example, the echo time (TE) is defined as the time between the center of the RF pulse and the start of the signal acquisition. The repetition time (TR) describes the time between consecutive excitations.

The last equation is called 'signal equation' and demonstrates that the measured MR signal and the position-dependent magnetization are related via the Fourier transformation. The required spatial encoding of the signal can be performed by applying magnetic field gradients in each spatial dimension (Figure 4-3). Ample information about pulse sequence design can be found in (5).

After a spin excitation, the return of the magnetization into thermal equilibrium can be quantified by a longitudinal (T_1) and a transverse (T_2) relaxation time constant. The inverse of T_1 describes the rate with which the longitudinal magnetization grows back to its equilibrium value M_0. The T_2 relaxation time describes the loss of coherence of the different spins because

each spin experiences a slightly different nuclear environment and hence magnetic field. Additionally, inhomogeneities of the static magnetic field lead to a shorter apparent transverse relaxation time T_2^*:

$$\frac{1}{T_2^*} = \frac{1}{T_2} + \frac{1}{T_2'}. \tag{4.13}$$

A set of partial differential equations, introduced by Felix Bloch in 1946 (6), can be used to describe the evolution of the magnetization for spin-1/2 particles:

$$\begin{aligned}
\frac{dM_x(t)}{dt} &= \gamma B_z(t) M_y(t) - \gamma B_{1y}(t) M_z(t) - \frac{M_x(t)}{T_2}, \\
\frac{dM_y(t)}{dt} &= \gamma B_{1x}(t) M_z(t) - \gamma B_z(t) M_x(t) - \frac{M_y(t)}{T_2}, \\
\frac{dM_z(t)}{dt} &= \gamma B_{1y}(t) M_x(t) - \gamma B_{1x}(t) M_y(t) - \frac{M_z(t) - M_0}{T_1},
\end{aligned} \tag{4.14}$$

where B_{1x} and B_{1y} are the time-dependent transverse components of the RF transmit field generated by the coil. For nuclei with s>1/2 a full quantum mechanical treatment is required to describe all the observed phenomena (2,7).

4.2 Sodium MRI

Hydrogen is found in high concentrations (about 110 M) in the human body in the form of water and fat. Together with its favorable MR properties, the hydrogen nucleus is well suited for MRI and by far the most imaged nucleus. However, there are several other nuclei with non-zero spin (e.g. ^{17}O, ^{23}Na, ^{31}P) present in the human body, which can potentially provide additional information about metabolism, cellular integrity and disease progression, for example.

Sodium ions play a key role for a number of cellular and metabolic functions (8) and their concentration is highly regulated in the human body (9). In the nervous system, signal propagation relies on a depolarization of the axons caused by an influx of extracellular sodium ions. In the muscular system, a similar depolarization leads indirectly to a muscle contraction (8). Aside from its unique biological relevance, the sodium nucleus possesses additionally some interesting physical properties, which differ considerably from those of hydrogen. The most obvious difference is its spin-3/2 nature. As a consequence, the relaxation process is not dominated by dipole-dipole interactions as it is the case for hydrogen but rather by interactions of the electric quadrupole moment of the sodium nucleus with electric field gradients (EFG) generated by other ions in the vicinity. This fact leads amongst other things to very short bi-exponential relaxation times of several tens of milliseconds in tissue (10). The relaxation behavior can be described by the following functions (11):

$$M_z(t) = M_0\left(1 - 0.2\exp\left(-\frac{t}{T_{1f}}\right) - 0.8\exp\left(-\frac{t}{T_{1s}}\right)\right), \quad (4.15)$$

$$M_{xy}(t) = M_{xy}(0)\left(0.6\exp\left(-\frac{t}{T_{2f}}\right) + 0.4\exp\left(-\frac{t}{T_{2s}}\right)\right), \quad (4.16)$$

where $T_{1s/f}$ and $T_{2s/f}$ are the slow/fast longitudinal and transverse relaxation times.

Moreover, new quantum mechanical effects, such as triple quantum coherences (12–15), can be observed and exploited to gain supplementary information. A more detailed description of the physical properties and spin dynamics of the sodium nucleus can be found e.g. in (11,16,17).

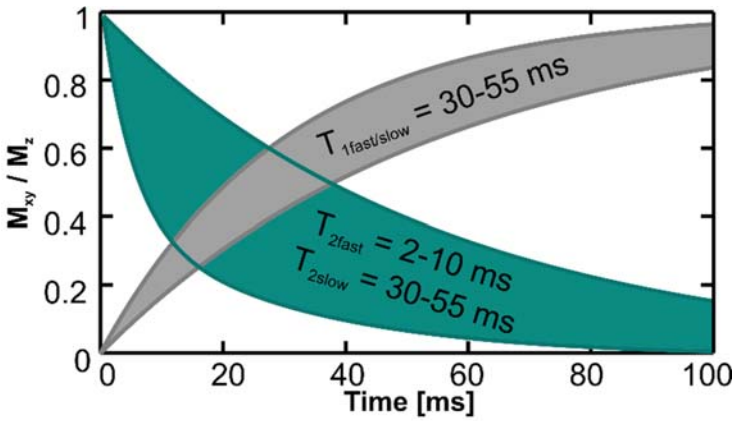

Figure 4-4. Typical longitudinal and transverse relaxation times for human tissue and fluids.

Even though ^{23}Na is the second most abundant MR-active nucleus in tissue, its concentration is small (30-150 mM)(18–21) compared to hydrogen. The low gyromagnetic ratio (γ_{23Na} = 11.26 MHz/T $\cong 1/4\,\gamma_{1H}$) and the short transverse relaxation times complicate further the application of sodium MRI in a clinical framework and require an adaptation of the imaging techniques commonly used for proton MRI. Early on (22), it was noted that ultra-short echo time sequences are needed to efficiently acquired the rapidly decaying signal. Since then, a multitude of sampling patterns has been presented in the literature for sodium imaging (23–27). Still, the reduced NMR sensitivity leads to long measurement times and enables the acquisition of images with only a coarse spatial resolution at low magnetic field strengths. The introduction of high and ultra-high field MR scanners during the last decades permitted increasing the achievable spatial resolution while maintaining the same SNR (28–31). However, new challenges arise when going to UHF such as reduced B_0 and B_1 field homogeneity or increased specific absorption rates (SAR).

4.3 Objectives

The first part of this thesis focused on the acquisition of high resolution quantitative sodium imaging of the human brain with the aim to decrease partial volume effects and consequently increase quantification accuracy. The main design criterion for the coil setup was a homogenous and efficient excitation at the sodium frequency, although the possibility to acquire proton images for anatomical localization and B_0 mapping was considered nearly equally important. For accurate quantitation, an ultra-short echo time sequence, which does not sample k-space uniformly, was implemented in order to limit the impact of relaxation on the measured signal. Since images acquired with non-Cartesian sequences are prone to off-resonance artefacts, adequate correction methods had to be applied to enhance the quality of the sodium images and the resulting tissue sodium concentration (TSC) maps. A more detailed description is given further down in the summary of **Publication 1**.

Although performing sodium MRI at 9.4 T leads already by itself to a substantial increase in sensitivity as compared to lower fields, the SNR can be increased further by using multi-channel coil arrays, which closely follow the anatomy of the human body part to be imaged. In the second stage of this thesis, a new combination of three different coils was implemented to meet the same requirements as specified for the previous setup but with the additional ability to acquire the sodium signal with numerous small receiver loops instead of a large volume coil. The setup consisted of a four-channel proton dipole array, a four-channel sodium transceiver coil and a 27-channel receiver array. In **Publication 2** the performance of the proposed coil arrangement was compared to the birdcage coil used in the previous imaging setup.

The high sensitivity provided by the three-layered sodium/proton coil and the high magnetic field strength were exploited in **Publication 3** to perform triple-quantum filtered sodium imaging, which intrinsically exhibits a low SNR. While challenging, this technique permits differentiating between signals from intra- and extra-cellular sodium and could potentially provide useful information for disease diagnosis and monitoring. However, the numerous RF pulses which are required for the TQ preparation lead to a high power deposition. In order to reduce the associated SAR and increase the efficiency of the TQF measurement, the possibility to modulate the flip angles of the RF pulses along the partition-encoding direction was investigated in the last part of the thesis.

5 PUBLICATION SUMMARIES

5.1 Publication 1:

High-resolution quantitative sodium imaging at 9.4 Tesla

The sodium concentration is highly regulated in the human body and a constant sodium concentration gradient is maintained by the Na^+/K^+ pump across the cell membrane. This leads to well defined intra- and extracellular sodium concentrations of about 12 and 40 mmol/L, respectively (9). Any deviation from this non-equilibrium state can be indicative of pathological changes induced by e.g. tumors (32), multiple sclerosis (21) or stroke (33). Hence, estimating the total sodium concentration might provide useful information for diagnostic purposes and monitoring the course of treatment. Unfortunately, the low sodium concentrations found in the human body limit the application of quantitative sodium imaging

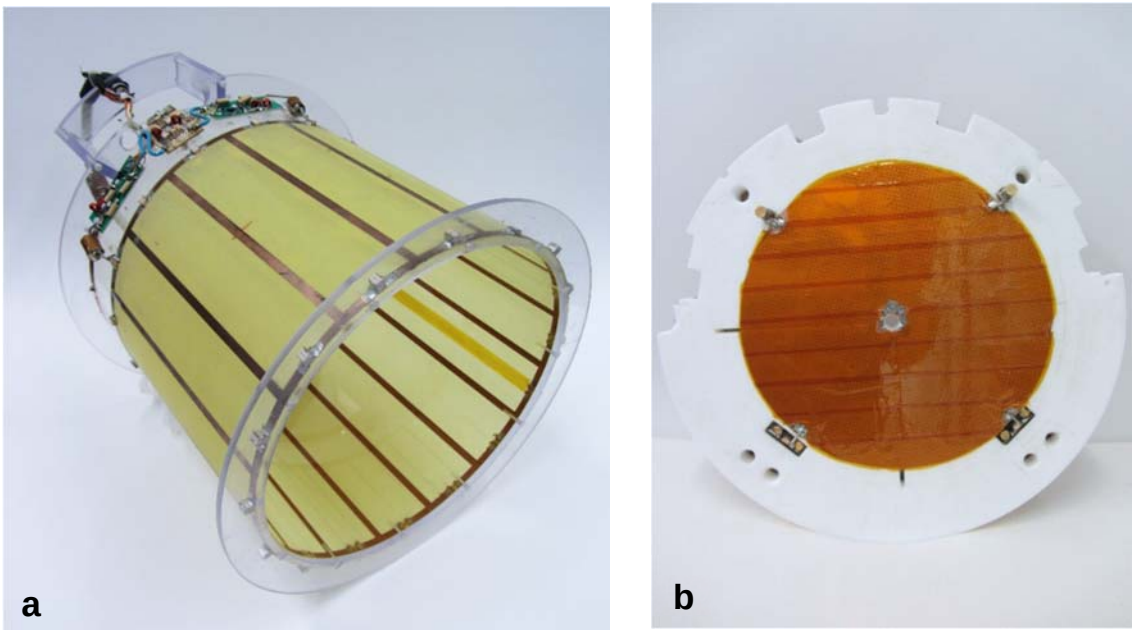

Figure 5-1. a: Quadrature-driven 16-rung high-pass sodium birdcage coil. **b:** Two-channel proton patch antenna.

at low magnetic field strengths. In order to maintain a clinically acceptable measurement time (≈30 min) and a satisfactory SNR, the resolution of the acquired tissue sodium concentration maps has to be increased to such an extent that partial volume effects cannot be neglected anymore. Consequently, under- or overestimation of the sodium content at tissue boundaries impedes an accurate estimation. At UHF strength, the increased NMR sensitivity permits reducing the voxel size considerably while maintaining the same SNR. The aim of this work was to design and implement a coil setup and the corresponding measuring techniques for high-resolution quantitative sodium imaging at 9.4 Tesla.

The sodium signal was acquired with a birdcage coil, which generated a sufficiently homogeneous transmit field even at 9.4 T due to the low resonance frequency of the sodium nucleus (105.6 MHz) (Figure 5-1a) (34). Although the sodium signal can be used for anatomical localization and B_0 shimming at UHF (35), it is preferable to accomplish these tasks via proton imaging due to the much higher achievable SNR. However, most UHF scanners do not possess a body coil, which could be used for proton imaging. Therefore, the ability to acquire the proton signal (399.7 MHz) had to be integrated into the coil setup as well. While it is possible to design a dual-tuned birdcage coil for proton and sodium imaging (36), the achievable transmit homogeneity at 400 MHz would be markedly inferior to the sophisticated multi-channel transmit arrays currently used for proton imaging at 9.4 T (37). The additional circuitry needed to support both frequencies would lead to a further decrease in transmit and receive efficiency for both nuclei. In this work, the sodium birdcage coil was combined with a proton patch antenna (38,39) (Figure 5-1b). The antenna was used to create a travelling wave within the bore of the scanner, which acted as a wave guide. It was shown that a large longitudinal coverage for proton imaging could be achieved in this way without having any negative effect on the transmit performance of the sodium coil.

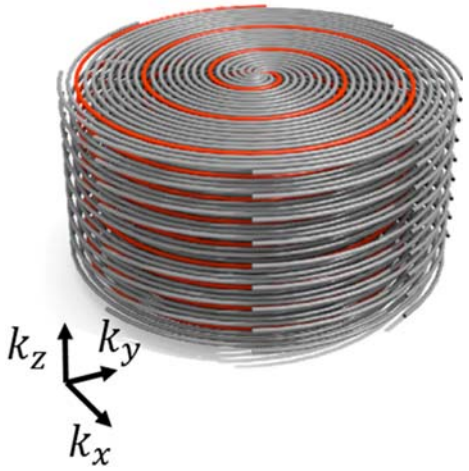

Figure 5-2. Stack of spirals used for the acquisition of sodium density weighted images.

For quantitative imaging the impact of the longitudinal and transverse relaxation on the received signal must be minimized. While T_1 weighting can be easily avoided by using repetition times (TR) much longer (about $5 \cdot T_1$) than the longitudinal relaxation time, the bias introduced by the short transverse relaxation time is much harder to eliminate. Standard Cartesian sampling schemes, which are normally used for proton MRI, are not well

suited for this task because the minimal echo time is limited by the duration of the phase encoding gradients. Instead, center-out sampling patterns such as radial lines and spirals, which permit achieving ultra-short echo times (< 1 ms), have to be used. In this work, an acquisition-weighted stack of spirals (25,40) was implemented for the acquisition of sodium density weighted images (Figure 5-2). However, compared to Cartesian imaging, such acquisition schemes are much more susceptible to off-resonance artefacts, which are even more pronounced at UHF as a result of the reduced B_0 homogeneity. To mitigate this problem, the additionally accrued phase of the signal due to B_0 offsets was approximated by Cebyshev polynomials (41). Together with a B_0 field map acquired with the patch antenna, a retrospective correction of blurring artifacts could be performed for all images acquired with non-Cartesian imaging sequences and resulted in an improved image quality. Inhomogeneities of the transmit field were corrected for by mapping the B_1 distribution (42) and dividing the images on a voxel-by-voxel basis by the sine of the achieved flip angle.

Signal calibration can be performed using either internal reference standards (vitreous humor or cerebrospinal fluid (CSF)) or external calibration phantoms. Since internal reference

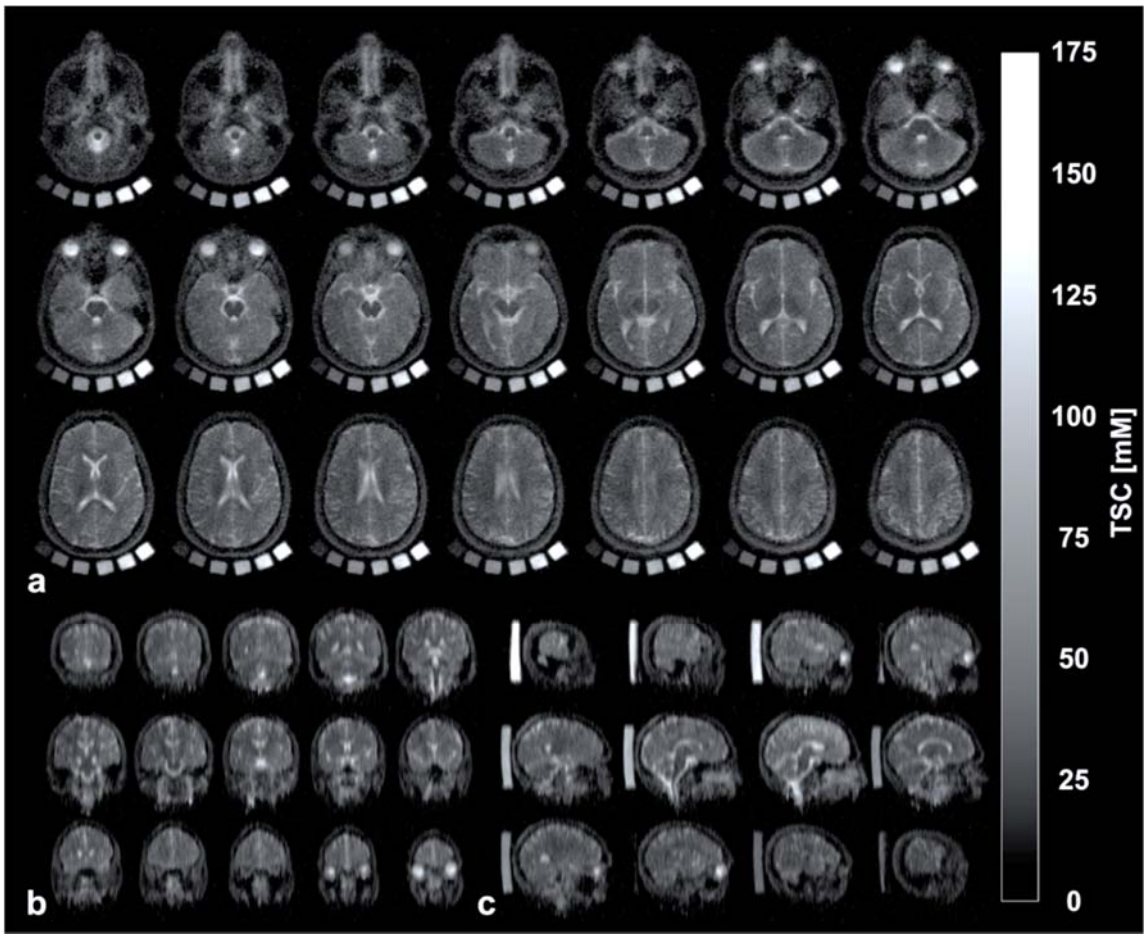

Figure 5-3. Transverse (**a**), coronal (**b**), and sagittal (**c**) TSC maps of a healthy volunteer. The reference cushion was placed below the subject's head to perform the signal calibration.

standards are limited in number and their concentrations are not well determined, a home-build reference cushion made of silicon-caoutchouc and containing agar gels with six different sodium concentrations was used in this study to relate the measured signal intensity to the underlying tissue sodium concentrations. The used correction and calibration techniques were validated by phantom measurements and used in five healthy human volunteers. Sodium density weighted images with a nominal resolution of 1x1x5 mm^3 were acquired and transformed after corrections into TSC maps. Simulations of the PSF showed that the actual voxel size was at least twice as large as the nominal resolution in each spatial direction. Nevertheless, a higher sensitivity (SNR per unit time) compared to previous studies could be achieved at 9.4 T. The measured sodium concentrations were similar to those previously reported in the literature (18,20,21): gray matter 36±2 mmol/L; white matter 31±1 mmol/L.

In conclusion, high-resolution quantitative imaging is feasible at 9.4 T and provides a much higher sensitivity as compared to lower fields. However, given the achievable actual spatial resolution partial volume effects are still affecting the determined sodium concentration values. This is especially true for gray matter because there is a large concentration difference between the CSF-filled sulci and brain tissue. Since a further increase in scanning time is not an option, the only way to reduce the voxel size while maintaining the same SNR is to perform signal reception with a multi-channel receiver array, which provides a higher sensitivity compared to a birdcage coil, at least close to the receive elements (see Publication 2).

Contributions

J. Hoffmann provided the proton patch antenna and helped combining it with the birdcage resonator, which was built by G. Shajan. I performed the setup testing and implemented the non-Cartesian sequences as well as the required reconstruction and correction algorithms. Furthermore, I built the reference cushion, performed the measurements, analyzed the data and wrote the manuscript. R. Pohmann and K. Scheffler gave advice on the study design and the manuscript.

5.2 Publication 2:

Three-layered RF Coil Arrangement for Sodium MRI of the Human Brain at 9.4 Tesla

It has been shown previously for proton imaging at 3 T (120 MHz), which is very close to the sodium resonance frequency at 9.4 T, that multi-channel arrays provide a higher SNR compared to single channel volume coils (43,44). The SNR increase is most pronounced close to the receiver array, while there is no substantial change to be expected in the center of the coil. The aim of this project was to increase the sensitivity further compared to the setup used for Publication 1.

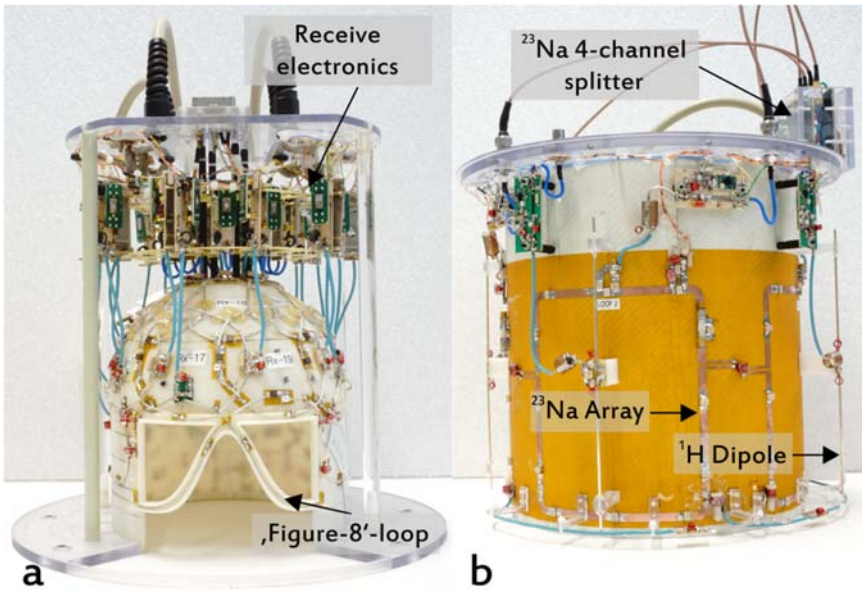

Figure 5-4. a: 27-channel receive helmet with receive electronics. **b:** Four-channel sodium transceiver array and four-channel proton dipole array.

The first attempt to place a multi-channel receiver array (Figure 5-4a) inside a birdcage coil and to use the patch antenna for RF transmission at the proton frequency proved to be unpromising. The numerous cables and the receive electronics belonging to the receiver array acted as an RF shield and prevented an efficient proton excitation and reception by the patch antenna. As a consequence, the latter was replaced by a four-channel dipole array (45), which was fixed as a third outer layer around the sodium coil. Since the rungs of the birdcage, which were parallel to the dipole antennas, also shielded the RF field, it was necessary to use a four-channel transceiver array for RF transmission at the sodium frequency (Figure 5-4b). Receive function was also incorporated into the latter in order to be able to

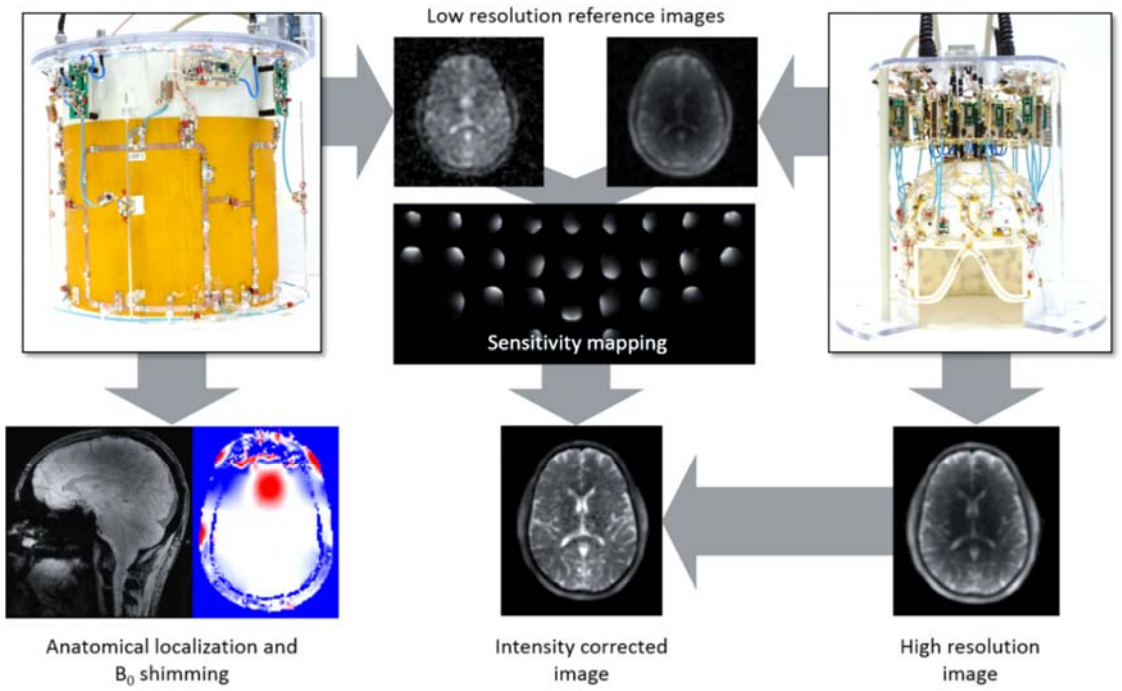

Figure 5-5. Tasks of the different coil components. The proton dipole array was used for anatomical localization and B_0 mapping. The helmet provided high SNR for sodium imaging. The sensitivity maps of the 27-channel array were calculated based on a homogenous reference image acquired with the four-channel sodium array.

acquire a more or less homogenous reference image with it as explained below (Figure 5-5). As the 9.4 T MRI system provided only 32 independent broadband receiver channels and four of those were already used up by the proton array, the signal from the four-channel sodium transceiver array was combined on the coil and fed to a single receive channel. The remaining 27 channels were used for the sodium receiver array (Figure 5-4a). The corresponding elements were arranged in four rows on a tight-fitting 3D printed helmet. The first two top rows comprised nine loops, which formed complete rings around the helmet. There were six elements and one figure-8 coil in the third row. The last row consisted of only two loops. The transmit efficiency of the transceiver array was reduced by about 5% due to the addition of the receive helmet, while the overall B_1^+ field distribution remained unchanged. In contrast, the B_1^+ field generated by the dipoles was visibly influenced by the cabling of the receiver array. A distortion of the B_1^+ pattern could be noticed, but the amplitude remained similar.

Phased arrays are characterized by an inhomogeneous receive profile (Figure 5-5). In order to correct for these intensity variations in the acquired images, a sensitivity map of each channel must be created. For proton imaging at low and high field, the body coil is normally used to acquire a reference image which exhibits low SNR but at the same time small

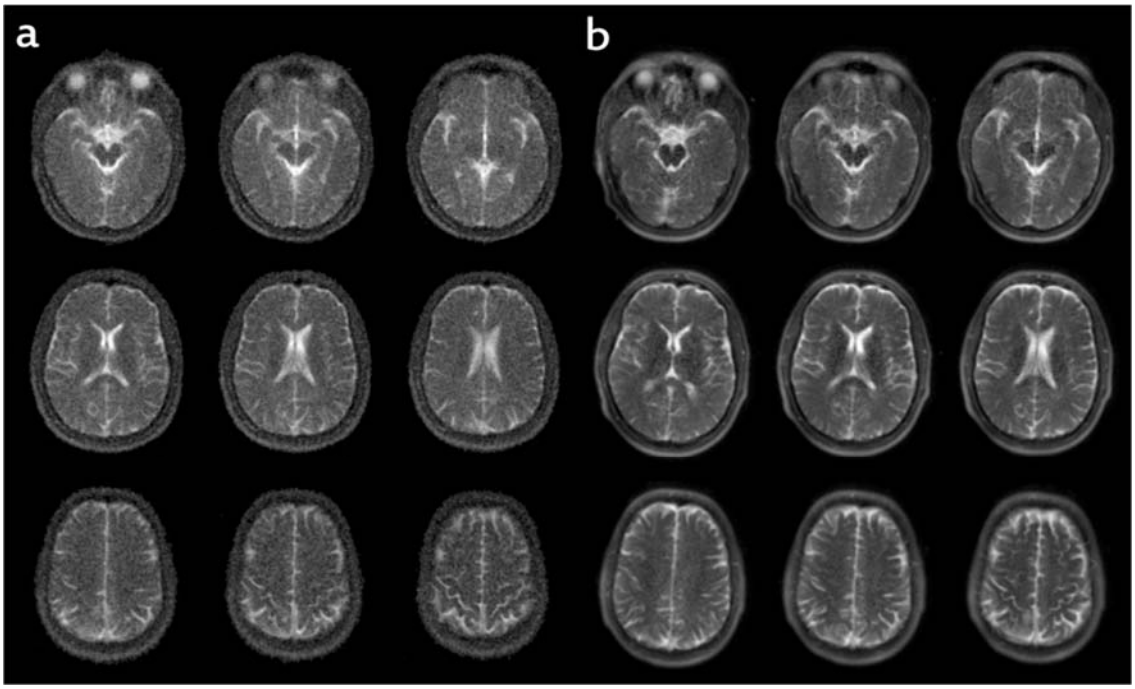

Figure 5-6. Sodium density weighted images of the same subject acquired with the birdcage (a) and the 27-channel receiver array (b) after intensity correction. The sequence parameters were: resolution 1x1x5 mm^3, TE 0.3 ms, TR 150 ms, readout duration 20 ms, measurement duration 30 min.

sensitivity variations. If the same image is acquired with a phased array, the sensitivity maps of the latter can be easily calculated by dividing both images and applying a smoothing algorithm (46). In case of X-nuclei imaging, an adequate substitute for the missing body coil is required. In the current coil setup, the four-channel sodium transceiver array provided this homogeneous reference image (Figure 5-5).

The performance of the setup was compared to the birdcage coil used for Publication 1. The transmit performance of the three-layered coil was about 17% weaker, which can be explained in part by the slightly smaller diameter of the birdcage coil and the absence of the additional circuitry needed for active detuning. Compared to the birdcage, the 27-channel receiver array provided a 2.8-fold SNR increase in the center of a slice passing through the top row of receive loops. The SNR gain was even more pronounced at the periphery. In the center of the coil, the performance was slightly lower, which can be explained by fact that the receive elements were not distributed evenly around the head but followed the anatomy of the brain. Sodium density weighted images of the same volunteer acquired with the birdcage coil and the 27-channel receiver array are shown for comparison in Figure 5-6. The imaging parameters were identical to those used for Publication 1.

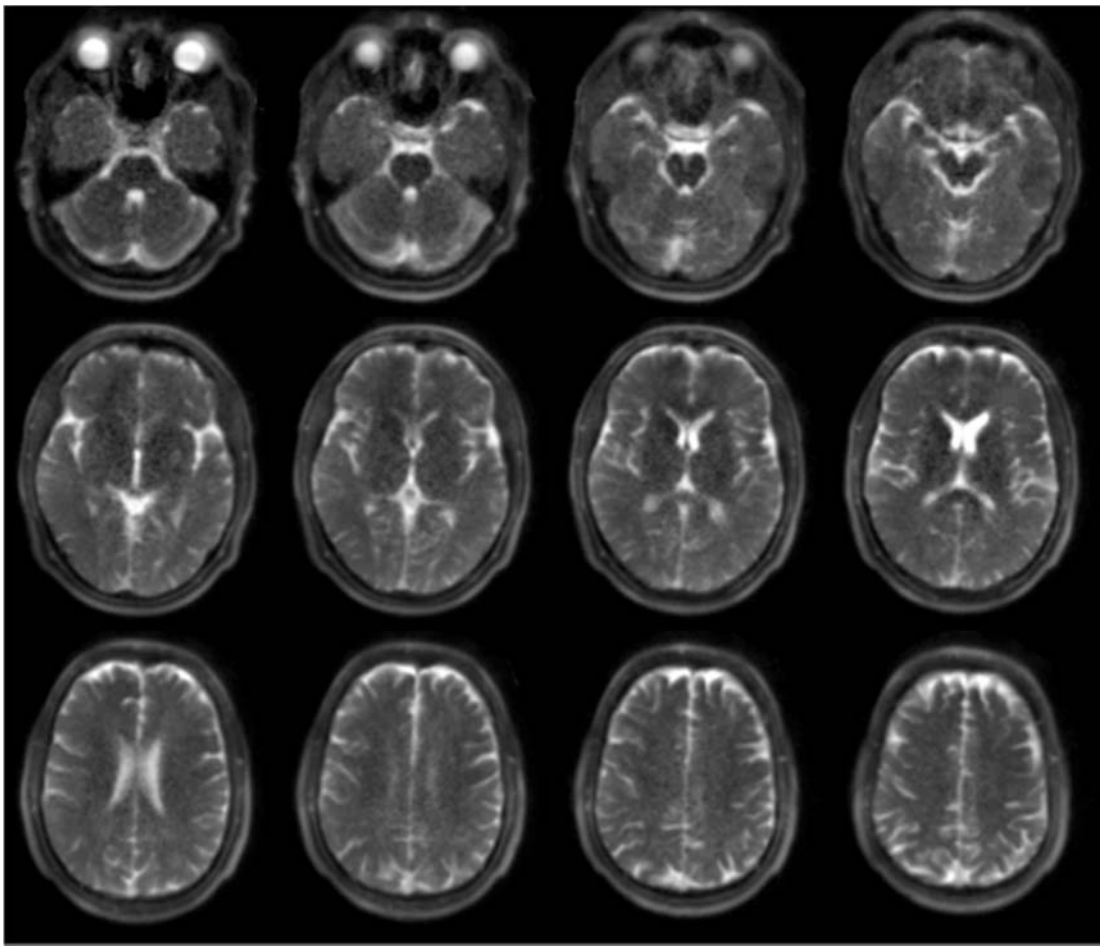

Figure 5-7. Balanced steady state free precession images from a healthy volunteer after intensity correction. Sequence parameters: resolution 1.5x1.5x4 mm^3, TE 1.5 ms, TR 11 ms, acquisition duration 11 min.

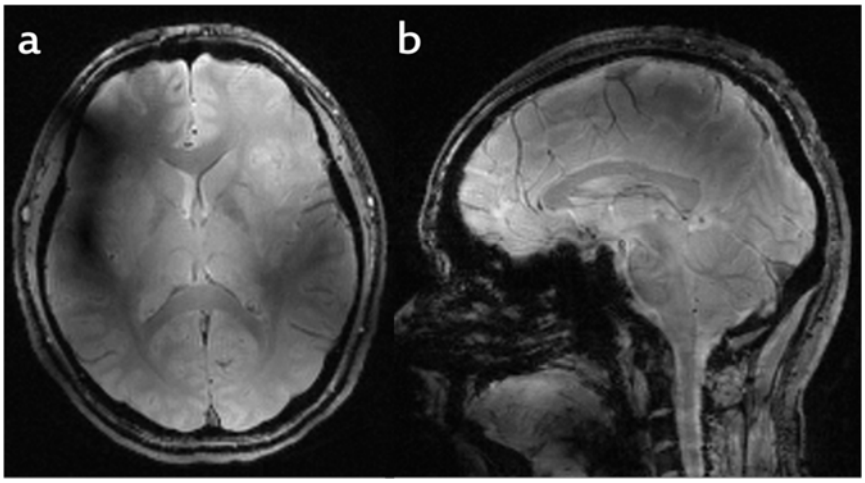

Figure 5-8. Transverse (**a**) and sagittal (**b**) proton images of a healthy volunteer demonstrating the large longitudinal coverage provided by the dipole array. Sequence parameters: resolution 1.1x1.1 mm^2, slice thickness 2 mm, TE 5 ms, TR 300 ms.

Excellent image quality could be achieved with the 27-channel receiver array in under 15 min. Fine anatomical details such as the CSF-filled sulci can be discerned in sodium balanced steady state free precession (bSSFP) images (47) (Figure 5-7). Intensity variations in the images could be removed by means of the sensitivity correction. The sagittal gradient echo images demonstrate the large longitudinal coverage provided by the proton dipole array. The axial proton images exhibit several signal dropouts, which were caused by interactions of the RF field with components of the sodium coil.

In summary, the coil setup described above fulfilled all the design criteria needed for efficient multi-nuclear imaging at 9.4 T. The dipole array allowed for anatomical localization and B_0 shimming and the 27-channel receiver array provided increased sensitivity at the sodium frequency.

Contributions

G. Shajan and I defined the design criteria for the sodium coil. He built the coil and performed all the bench measurements. Together, we tested and validated the coil arrangement. Moreover, I implemented the imaging sequences and algorithms for B_1^+ mapping and intensity correction. K. Buckenmaier and J. Hoffmann performed the numerical coil simulations for the SAR assessment. R. Pohmann and K. Scheffler gave advice on the manuscript.

5.3 Publication 3:

Triple-Quantum-Filtered Sodium Imaging at 9.4 Tesla

As a spin-3/2 particle, the sodium nucleus possesses an electric quadrupole moment, which makes it sensitive to electric field gradients. In the human body, fluctuating EFGs are generated by the thermal motion of other ions or macromolecules in the vicinity of the nucleus. In a magnetic field, the four distinct Zeeman eigenstates are perturbed by this quadrupolar interaction and the relaxation behavior of the sodium nucleus changes depending on the correlation time of these fluctuations (11). If the correlation time is short compared to the Larmor period, the relaxation is mono-exponential. If the fluctuations are slow and the correlation time is longer than the Larmor period, the relaxation is characterized by a bi-exponential decay.

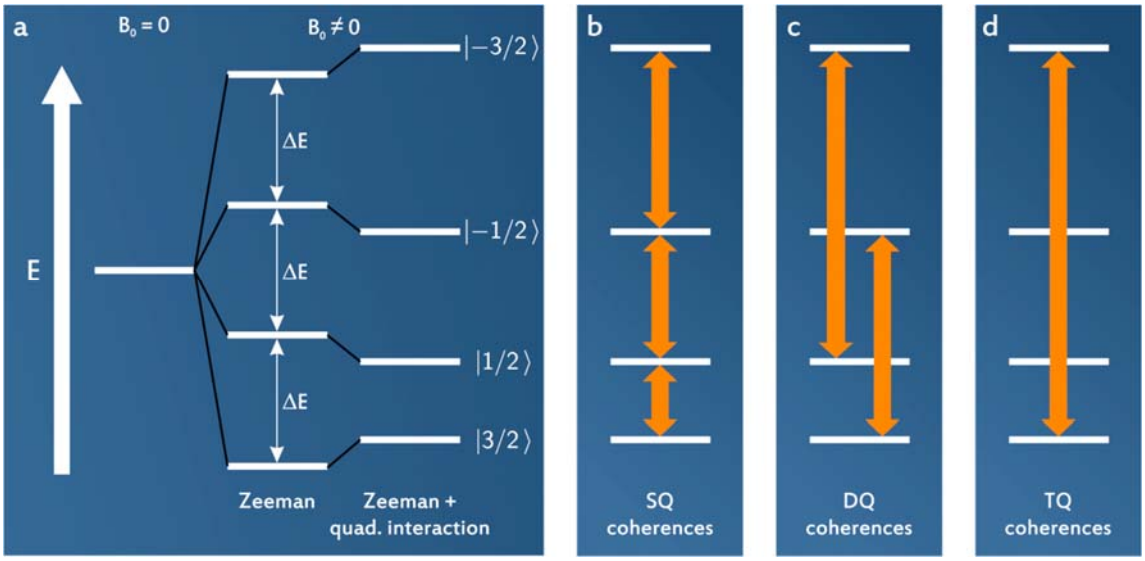

Figure 5-9. a: Zeeman splitting in an external magnetic field and perturbation of the energy levels of a spin-3/2 particle by the quadrupolar interaction. **b:** Single-quantum coherences, which are related to the observable transverse magnetization. **c:** Double-quantum coherences. **d:** Triple-quantum coherences.

For protons only single-quantum coherences, which are associated with transitions between the two energy states (m_s = ±1/2), can be realized. These transitions are related to the observable transverse magnetization. In case of a spin-3/2 particle, double (DQ) and triple-quantum coherences are in principle possible beside the single-quantum coherences. DQ and TQ coherences involve a change $\Delta m_s = \pm 2$ and $\Delta m_s = \pm 3$, respectively. These coherences are not related to an observable magnetization and can, as a consequence, not be measured directly. Moreover, these higher transitions are forbidden by coherence

transfer selection rules, which can only be violated in media with sufficiently slowly fluctuating EFGs (2).

In the human body, sodium ions experience different molecular environments in the intra- and extracellular compartment. Outside of the cell, the ions can be considered to be free and the fluctuations of the EFGs are so fast that no higher coherences can be created. Within the cells, the motion of the sodium ions is restricted and large tumbling macromolecules and the cell walls generate slowly varying EFGs, which permit the formation of triple-quantum coherences. Hence, the TQ coherences are closely related to intracellular sodium. However, it should be noted that higher coherences can also be generated in the extracellular compartment by the same mechanism, but to a much smaller extent (48,49).

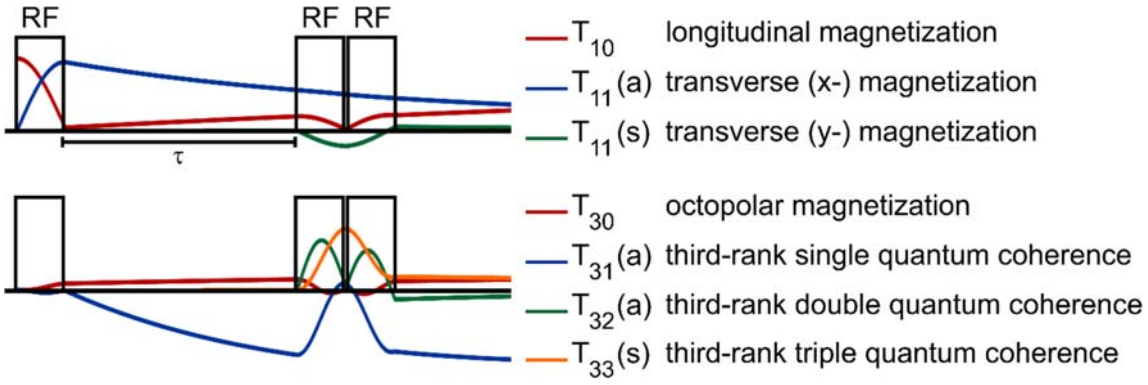

Figure 5-10. Three-pulse triple quantum preparation. The evolution of the polarization can be described by spherical tensor operators T_{lp}.

Since higher quantum coherences are not associated with an observable magnetization, they have to be created and then transformed back into measurable transverse magnetization. The pulse sequence to achieve this consists of at least three RF pulses (14) (Figure 5-10). The polarization of the nuclear ensemble can described by spherical tensor operators T_{lp}, where l is rank and p the order of the coherence (16). The first pulse creates SQ (first rank) coherences (T_{11}), i.e. transverse magnetization. The quadrupolar relaxation transforms the transverse magnetization into third-rank single quantum coherences (T_{31}) during the preparation time τ. The second pulse increases the order of the coherences and produces third-rank triple quantum coherences (T_{33}). The last pulse reduces the order again and the quadrupolar relaxation converts the coherences back into transverse magnetization. This three-pulse TQ preparation is the most common multiple-quantum filter used for human imaging. However, it is also possible to include an additional 180° pulse for refocussing and additional robustness again B_0 artefacts, however at the expense of a significantly increased power deposition (14,15,50).

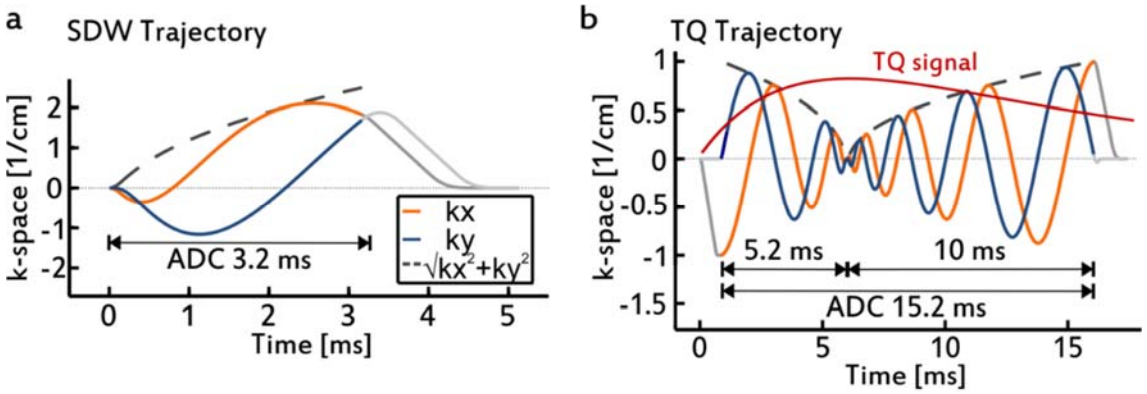

Figure 5-11. a: Spiral trajectory used for the acquisition of SDW images. **b:** Double-spiral sampling pattern used to acquire the TQ signal.

Each RF pulse creates a multitude of coherences but only coherence pathways which involve the formation of TQ coherences are of interest for TQ imaging. The selection of these pathways is accomplished by phase cycling. Phase cycling relies on the repetition of the TQ preparation with different phase settings of the RF pulses. If the phases are chosen adequately, only the desired pathways will contribute to the signal after summation of all phase cycling steps and all the other contributions will cancel out (14).

A major disadvantage of TQF imaging is the low achievable SNR. In fact, the TQ signal is only 10% of the already small SQ signal (15). UHF scanners and multi-channel receive coils can be used to increase the sensitivity. However, the implementation of the TQ preparation is challenging at 9.4 T due to the associated high SAR values. The decreased B_0 homogeneity is another issue which has to be taken into account because the TQ images are prone to off-resonance artefacts (51–54).

In the present study, a three-pulse preparation was used to generate multiple-quantum coherences. The TQ coherence pathways were filtered out with a two-times-six phase cycling scheme, which allowed performing a B_0 correction in post-processing (52,54). Since only SQ coherences are present immediately after the first RF pulse, sodium density weighted (SDW) images could be acquired with a stack of spirals during the preparation time (Figure 5-11a). A rephasing gradient was used to null the zeroth gradient moment before the application of the second RF pulse and prevent any perturbation of the TQ preparation (50). The TQF images were acquired after the third pulse with a stack of double-spirals. Only a few interleaves were required to cover the entire k-space. The center-in part of the spiral permitted sampling the MR signal also before the formation of the delayed TQ intensity peak (Figure 5-11b).

The highest TQ contrast is achieved if all flip angles of the TQ preparation are equal to 90°. The associated high power deposition requires at UHF either a decrease of the flip angles or an increase of the pulse duration and/or the repetition time. The first two options lead to a reduced TQ signal, while the last option results in a long and inefficient acquisition. In this work, the possibility to modulate the flip angles of the TQ preparation along the partition-encoding direction was investigated. The flip angles were smoothly reduced towards the edge of k-space. By doing so, SAR could be reduced while maintaining a high flip angle for the central partitions, which are most relevant for image contrast.

The flip angle modulation acts as a filter on k-space and reduces the spatial resolution along the partition-encoding direction. Phantom measurements and simulations showed that the spatial resolution of the SDW images was much less affected by the flip apodization than the TQF images. Nevertheless, the simulation of the sensitivity (SNR per unit time and volume) revealed that a more efficient acquisition is possible if the flip angles are modulated. This result could be validated by phantom measurements. Moreover, it was demonstrated that signal from sodium ions in free motion could be successfully suppressed irrespective of the amount of apodization used.

In vivo sequence parameter optimization was performed in one healthy human volunteer. The optimal preparation time was 5.5 ms, which is similar to values reported previously in the literature (14,15). The durations of the RF pulses were chosen to be 1.5 (1st pulse) and 1 ms (2nd and 3rd pulse) based on a compromised between SNR and efficiency of the B_0 correction,

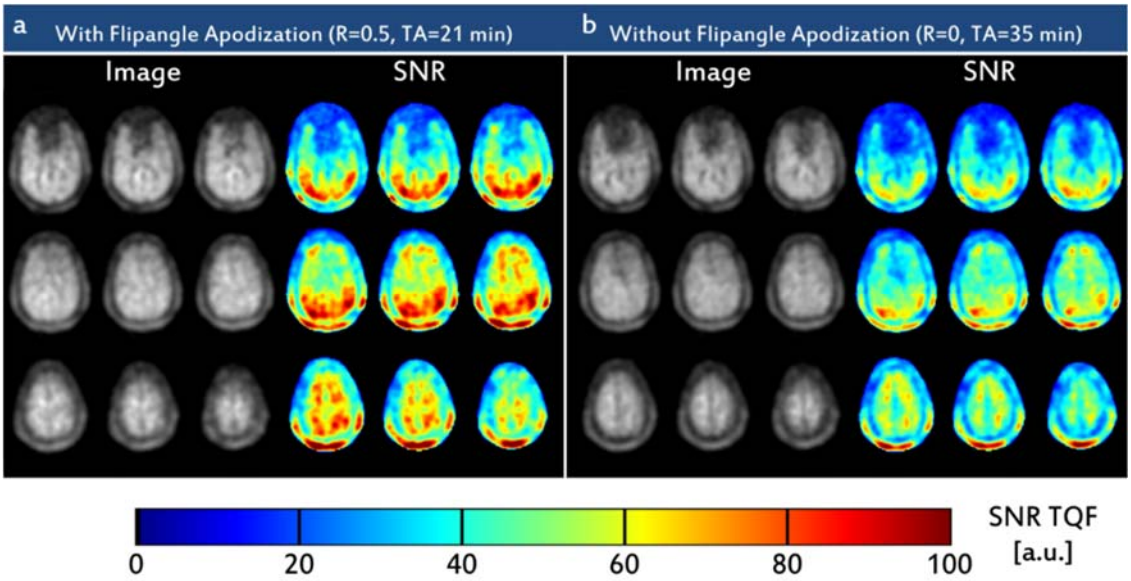

Figure 5-12. TQ images and corresponding SNR maps acquired with (**a**) and without (**b**) flip angle apodization. The SNR maps have been scaled by the square-root of the required measurement time to allow for a fair comparison.

which only works well for short RF pulses. The FoV (250 mm^2) and the number of partitions (52) were identical for the SDW and the TQF acquisition. Further imaging parameters for the SDW images were: nominal resolution 2x2x5 mm^3, TE_1 0.8 ms, RO 3.2 ms, 120 spiral interleaves per partition, and 1 average. The TQ images had a nominal resolution of 5x5x5 mm^3 and an echo time TE_2 of 6.5 ms was used. Ten double-spiral interleaves were needed to cover one partition. The measurment time was 21 min for a flip angle apodization of 50%. As for the phantom measurements, a sensitivity increase of about 20% compared to the standard TQ acquisition could be detected. The CSF was not fully suppressed in the in vivo images due to partial volume effects caused by the low spatial resolution. Moreover, signal dropouts above the nasal cavities could only be mitigated by the B_0 correction but not completely avoided.

To sum up, flip angle apodization permits to acquire conventional TQF images with a higher sensitivity. The combination of UHF MRI with a multi-channel receive array allowed reducing the measurement time to 21 min. The achieved resolution was insufficient to resolve small anatomical details, but TQF imaging might still be useful on a slightly larger scale.

Contributions

G. Shajan built the sodium coil. J. Bause assisted in the measurements. K. Buckenmaier and J. Hoffmann took care of the numerical simulations for SAR evaluation. K. Scheffler gave advice on the manuscript. I implemented the SDW/TQ sequence and the reconstruction algorithms. Moreover, I acquired and evaluated the data and wrote the manuscript.

6 CONCLUSION

Sodium MRI remains challenging even at 9.4 T due to the low intrinsic sensitivity. However, it could be shown that dedicated receive hardware and imaging sequences allow to achieve an unprecedented image quality. The use of a multi-channel receive coil provided the expected SNR gain close to the receive loops as known from proton imaging. This increase in sensitivity could be traded in a straightforward manner for higher spatial resolution or shorter acquisition times. A high spatial resolution is crucial for accurate TSC mapping because partial volume effects otherwise lead to over- or underestimation of the sodium concentration at tissue boundaries. At 9.4 T the latter issue could only be mitigated but not completely eliminated.

The ability to perform proton together with sodium imaging is a key requirement at ultra-high field because anatomical localization as well as B_0 shimming and mapping can be performed much more efficiently based on the proton than the sodium signal. In this thesis two novel coil combinations were developed, which provided this feature without reducing the transmit or receive performance of the sodium coil. The efficiency of the patch antenna or the dipole array was much lower as compared to a dedicated single-resonant proton coil. However, the performance of the two setups was sufficient for the intended purpose.

Ultra-high field MRI provides a higher sensitivity but at the same time it makes the acquisition of images slightly more complicated. While elevated specific absorption rates or B_0/B_1 inhomogeneities are in most cases only a minor issue at low field, they need to be addressed with adequate coping and correction strategies at UHF.

Although sodium imaging cannot compete with proton MRI regarding spatial resolution and SNR, the combination of the two modalities should allow increasing the diagnostic value of an MR examination. While only healthy volunteers were scanned within the framework of this thesis, the obtained results advocate the application of the implemented methods in patients in order to evaluate their potential regarding disease diagnosis and monitoring.

7 ACKNOWLEDGMENTS

This thesis would not have been possible without the support of many people to whom I would like to express in the following my sincere gratitude. First of all, I would like to thank my supervisor Klaus Scheffler for valuable discussions and advice and giving me the possibility to do my PhD at an institute with cutting-edge technology. I also thank Reinhold Kleiner for kindly agreeing to supervise this thesis.

A huge thank you to Shajan for building these amazing coils. Without him sodium imaging would not have been possible at 9.4 T. Thank you for all your ingenious ideas and the endless hours we spend in the lab and at the scanner trying to improve the coil performance even further. I really enjoyed working with you. A special thank you to Jonas for valuable discussions and help as scanner operator and co-pilot.

I would also like to thank my office mates and colleagues (present and past) David, Marlon, Andreas, Frank, Franziska, Grzegorz, Hildegard, Irena, Jens, Julia, Kai, Martin, Mihai, Philipp, Rolf, Tina and the rest of the MR group at the UKT and MPI. Thank all of you for support, trouble-shooting of hard- and software related problems, and the nice time I had with you at the institute. I am grateful for the time you spend with me in and out of the scanner as a subject or co-pilot.

Last but not least, I would like to thank my parents and my siblings for their support over all these years. I also thank my friends here in Tübingen and elsewhere for their friendship and distraction from work.

8 ABBREVIATIONS AND PHYSICAL CONSTANTS

8.1 Abbreviations

B_0	main static magnetic field
B_1	RF transmit field
bSSFP	balanced steady state free precession
CON	Cones trajectory
CSF	cerebrospinal fluid
DAR	density adapted radial projection imaging
DQ	double-quantum
EFG	electric field gradient
FoV	field of view
FWHM	full width at half maximum
GRE	gradient echo
MRI	magnetic resonance imaging
MRT	Magnetresonanztomografie
NMR	nuclear magnetic resonance
PSF	point-spread function
RAD	radial projection imaging
RF	radio frequency
RO	readout
SAR	specific absorption rate
SDW	spin density weighted
SNR	Signal-to-noise ratio
SQ	single-quantum
T_1	longitudinal relaxation time
T_2	transverse relaxation time
T_{2f}	fast T_2 component
T_{2s}	slow T_2 component

TE	echo time
TPI	twisted projection imaging
TQ	triple-quantum
TQF	triple-quantum filtering
TR	repetition time
TSC	tissue sodium concentration
UHF	ultra-high field

8.2 Physical Constants

γ_{1H}	42.58 MHz/T	Larmor constant ^{1}H
γ_{23Na}	11.26 MHz/T	Larmor constant ^{23}Na
k_B	1.38×10^{-23} J/K	Boltzmann constant
$\hbar$	1.05×10^{-34}	Reduced Planck constant

9 REFERENCES

1. Haacke EM, Brown RW, Thompson MR, Venkatesan R. Magnetic Resonance Imaging: Physical Principles and Sequence Design. Wiley-Liss; 1999.

2. Levitt MH. Spin Dynamics: Basics of Nuclear Magnetic Resonance, 2nd Edition. Wiley Chichester; 2008.

3. Demtröder W. Experimentalphysik 4. Springer; 2005.

4. Hanson LG. Is Quantum Mechanics Necessary for Understanding Magnetic Resonance? Concepts Magn. Reson. Part A 2008;5:329–340.

5. Bernstein MA, King KF, Zhou XJ. Handbook of MRI Pulse Sequences. Elsevier academic press; 2004.

6. Bloch F. Nuclear induction. Phys. Rev. 1946;70:460–474.

7. Bowden GJ, Hutchison WD, Khachan J. Tensor Operator Formalism for Multiple-Quantum NMR. J. Magn. Reson. 1986.

8. Pohl HR, Wheeler JS, Murray HE. "Chapter 2. Sodium and Potassium in Health and Disease". In: Interrelations between Essential Metal Ions and Human Diseases. Springer 2013. pp. 29–47.; 2013.

9. Boulanger Y, Vinay P, Desroches M. Measurement of a wide range of intracellular sodium concentrations in erythrocytes by 23Na nuclear magnetic resonance. Biophys. J. 1985;47:553–561.

10. Ouwerkerk R. Magnetic Resonance Neuroimaging. (Modo M, Bulte JWM, editors.). Humana Press; 2011.

11. Rooney WD, Springer CS. A comprehensive approach to the analysis and interpretation of the resonances of spins 3/2 from living systems. NMR Biomed. 1991;4:209–26.

12. Kharrazian R, Jakob PM. Dynamics of Na during completely balanced steady-state free precession. J. Magn. Reson. 2006;179:73–84.

13. Jaccard G, Wimperis S, Bodenhausen G. Multiple-quantum NMR spectroscopy of S=3/2 spins in isotropic phase: A new probe for multiexponential relaxation. J. Chem. Phys. 1986;85:6282.

14. Hancu I, Boada FE, Shen GX. Three-dimensional triple-quantum-filtered 23Na imaging of in vivo human brain. Magn. Reson. Med. 1999;42:1146–54.

15. Tsang A, Stobbe RW, Beaulieu C. Triple-quantum-filtered sodium imaging of the human brain at 4.7 T. Magn. Reson. Med. 2012;67:1633–43.

16. Hancu I, van der Maarel JR, Boada FE. A model for the dynamics of spins 3/2 in biological media: signal loss during radiofrequency excitation in triple-quantum-filtered sodium MRI. J. Magn. Reson. 2000;147:179–91.

17. Berendsen HJ, Edzes HT. The observation and general interpretation of sodium magnetic resonance in biological material. Ann. N. Y. Acad. Sci. 1973;204:459–85.

18. Qian Y, Zhao T, Zheng H, Weimer J, Boada FE. High-resolution sodium imaging of human brain at 7 T. Magn. Reson. Imaging 2012;68:227–33.

19. Lu A, Atkinson IC, Claiborne TC, Damen FC, Thulborn KR. Quantitative sodium imaging with a flexible twisted projection pulse sequence. Magn. Reson. Med. 2010;63:1583–93.

20. Atkinson IC, Lu A, Thulborn KR. Clinically constrained optimization of flexTPI acquisition parameters for the tissue sodium concentration bioscale. Magn. Reson. Med. 2011;66:1089–99.

21. Inglese M, Madelin G, Oesingmann N, Babb JS, Wu W, Stoeckel B, Herbert J, Johnson G. Brain tissue sodium concentration in multiple sclerosis: a sodium imaging study at 3 tesla. Brain 2010;133:847–57.

22. Ra JB, Hilal SK, Cho ZH. A method for in vivo MR imaging of the short T2 component of sodium-23. Magn. Reson. Med. 1986;3:296–302.

23. Boada FE, Gillen JS, Shen GX, Chang SY, Thulborn KR. Fast three dimensional sodium imaging. Magn. Reson. Med. 1997;37:706–15.

24. Nagel AM, Laun FB, Weber M-A, Matthies C, Semmler W, Schad LR. Sodium MRI using a density-adapted 3D radial acquisition technique. Magn. Reson. Med. 2009;62:1565–73.

25. Qian Y, Zhao T, Zheng H, Weimer J, Boada FE. High-Resolution Sodium Imaging of Human Brain at 7 T. Magn. Reson. Med. 2012;68:227–233.

26. Gurney PT, Hargreaves B a, Nishimura DG. Design and analysis of a practical 3D cones trajectory. Magn. Reson. Med. 2006;55:575–82.

27. Reetz K, Romanzetti S, Dogan I, Saß C, Werner CJ, Schiefer J, Schulz JB, Shah NJ. Increased brain tissue sodium concentration in Huntington's Disease - A sodium imaging study at 4T. Neuroimage 2012;63:517–524.

28. Qian Y, Zhao T, Zheng H, Weimer J, Boada FE. High-resolution sodium imaging of human brain at 7 T. Magn. Reson. Med. 2011;000:1–7.

29. Watts A, Stobbe RW, Beaulieu C. Signal-to-noise optimization for sodium MRI of the human knee at 4.7 Tesla using steady state. Magn. Reson. Med. 2011;66:697–705.

30. Atkinson IC, Renteria L, Burd H, Pliskin NH, Thulborn KR. Safety of human MRI at static fields above the FDA 8T guideline: Sodium imaging at 9.4T does not affect vital signs or cognitive ability. J. Magn. Reson. Imaging 2007;26:1222–1227.

31. Stobbe RW, Beaulieu C. Exploring and enhancing relaxation-based sodium MRI contrast. MAGMA 2014;27:21–33.

32. Ouwerkerk R, Bleich K, Gillen J. Tissue sodium concentration in human brain tumors as measured with 23 Na MR imaging. Radiology 2003;23:529–537.

33. Hussain MS, Stobbe RW, Bhagat Y a., et al. Sodium imaging intensity increases with time after human ischemic stroke. Ann. Neurol. 2009;66:55–62.

34. Hayes CE, Edelstein W a, Schenck JF, Mueller OM, Eash M. An Efficient , Highly Hokogeneous Radiofrequency Coil for Whole-Body NMR Imaging at 1 . 5 T. J. Magn. Reson. 1985;63:622–628.

35. Atkinson IC, Lu A, Thulborn KR. Preserving the accuracy and resolution of the sodium bioscale from quantitative sodium MRI during intrasubject alignment across longitudinal studies. Magn. Reson. Med. 2012;68:751–761.

36. Shen GX, Boada FE, Thulborn KR. Dual-frequency, dual-quadrature, birdcage RF coil design with identical B1 pattern for sodium and proton imaging of the human brain at 1.5 T. Magn. Reson. Med. 1997;38:717–725.

37. Shajan G, Kozlov M, Hoffmann J, Turner R, Scheffler K, Pohmann R. A 16-channel dual-row transmit array in combination with a 31-element receive array for human brain imaging at 9.4 T. Magn. Reson. Med. 2014;71:870–879.

38. Hoffmann J, Shajan G, Budde J, Scheffler K, Pohmann R. Human brain imaging at 9.4 T using a tunable patch antenna for transmission. Magn. Reson. Med. 2013;69:1494–1500.

39. Geschewski FH, Brenner D, Felder J, Jon Shah N. Optimum coupling and multimode excitation of traveling-waves in a whole-body 9.4T scanner. Magn. Reson. Med. 2013;69:1805–1812.

40. Qian Y, Boada FE. Acquisition-Weighted Stack of Spirals for Fast Echo Time MR Imaging. Magn. Reson. Med. 2008;60:135–145.

41. Chen W, Sica CT, Meyer CH. Fast conjugate phase image reconstruction based on a Chebyshev approximation to correct for B0 field inhomogeneity and concomitant gradients. Magn. Reson. Med. 2008;60:1104–11.

42. Stollberger R, Wach P, McKinnon G, Justich E, Ebner F. Rf-field mapping in vivo. In: Proceedings of the 7th Annual Meeting of ISMRM, San Francisco, California, USA, 1988. Abstract 106.

43. Roemer PB, Edelstein W a, Hayes CE, Souza SP, Mueller OM. The NMR phased array. Magn. Reson. Med. 1990;16:192–225.

44. Wiggins GC, Triantafyllou C, Potthast a., Reykowski a., Nittka M, Wald LL. 32-Channel 3 tesla receive-only phased-array head coil with soccer-ball element geometry. Magn. Reson. Med. 2006;56:216–223.

45. Wiggins G, Zhang B, Lattanzi R, Chen G, Sodickson D. The electric dipole arrray: an attempt to match the ideal current pattern for central SNR at 7 Tesla. In: In Proceedings of the 20th Annual Meeting of ISMRM, Melbourne, Australia, 2012. Abstract 541.

46. Pruessmann KP, Weiger M, Scheidegger MB, Boesiger P. SENSE: sensitivity encoding for fast MRI. Magn. Reson. Med. 1999;42:952–62.

47. Scheffler K, Lehnhardt S. Principles and applications of balanced SSFP techniques. Eur. Radiol. 2003;13:2409–2418.

48. Winter PM, Bansal N. TmDOTP5 – as a 23Na Shift Reagent for the Subcutaneously Implanted 9L Gliosarcoma in Rats. Magn. Reson. Med. 2001;45:436–442.

49. Seshan V, Sherry AD, Bansal N. Evaluation of Triple Quantum 23Na NMR Spectroscopy in the in Situ Rat Liver. Magn. Reson. Med. 1997;38:821–827.

50. Fiege DP, Romanzetti S, Mirkes CC, Brenner D, Shah NJ. Simultaneous single-quantum and triple-quantum-filtered MRI of 23Na (SISTINA). Magn. Reson. Imaging 2013;69:1691–6.

51. Tsang A, Stobbe RW, Beaulieu C. Evaluation of B0-inhomogeneity correction for triple-quantum-filtered sodium MRI of the human brain at 4.7 T. J. Magn. Reson. 2013;230:134–44.

52. Fleysher L, Oesingmann N, Inglese M. B0 inhomogeneity-insensitive triple-quantum-filtered sodium imaging using a 12-step phase-cycling scheme. NMR Biomed. 2010;23:1191–8.

53. Fiege DP, Romanzetti S, Tse DHY, Brenner D, Celik A, Felder J, Shah NJ. B0 insensitive multiple-quantum resolved sodium imaging using a phase-rotation scheme. J. Magn. Reson. 2013;228:32–6.

54. Matthies C, Nagel AM, Schad LR, Bachert P. Reduction of B(0) inhomogeneity effects in triple-quantum-filtered sodium imaging. J. Magn. Reson. 2010;202:239–44.

10 APPENDED PUPLICATIONS

PUBLICATION 1

PRECLINICAL AND CLINICAL IMAGING – Full Papers

Magnetic Resonance in Medicine 73:342–351 (2015)

High-Resolution Quantitative Sodium Imaging at 9.4 Tesla

Christian C. Mirkes,[1,2]* Jens Hoffmann,[2] G. Shajan,[2] Rolf Pohmann,[2] and Klaus Scheffler[1,2]

Purpose: Investigation of the feasibility to perform high-resolution quantitative sodium imaging at 9.4 Tesla (T).

Methods: A proton patch antenna was combined with a sodium birdcage coil to provide a proton signal without compromising the efficiency of the X-nucleus coil. Sodium density weighted images with a nominal resolution of $1 \times 1 \times 5$ mm^3 were acquired within 30 min with an ultrashort echo time sequence. The methods used for signal calibration as well as for B_0, B_1, and off-resonance correction were verified on a phantom and five healthy volunteers.

Results: An actual voxel volume of roughly 40 μL could be achieved at 9.4T, while maintaining an acceptable signal-to-noise ratio (8 for brain tissue and 35 for cerebrospinal fluid). The measured mean sodium concentrations for gray and white matter were 36 ± 2 and 31 ± 1 mmol/L of wet tissue, which are comparable to values previously reported in the literature.

Conclusion: The reduction of partial volume effects is essential for accurate measurement of the sodium concentration in the human brain. Ultrahigh field imaging is a viable tool to achieve this goal due to its increased sensitivity. **Magn Reson Med 73:342–351, 2015.**

Key words: sodium MRI; UTE imaging; sodium quantification; traveling wave

INTRODUCTION

Sodium (^{23}Na) is the second most abundant MR-active nucleus in the human body with intra- and extracellular concentrations of approximately 12 and 140 mM (1), respectively. It plays an important role in cellular ion homeostasis and cell viability. It has been shown previously that pathological changes of the sodium concentration in the human brain (2) and articular cartilage (3,4) can be monitored by means of ^{23}Na MRI. Unfortunately, the physical properties (5) of the sodium nucleus and the low in vivo concentrations lead to an inherently low sensitivity and complicate its use in clinical applications.

The signal-to-noise ratio (SNR) of the acquired tissue sodium concentration (TSC) maps can be increased in a straightforward manner either by decreasing the spatial resolution or by increasing the scanning time. While the latter option may lead to inacceptable measurement durations, a coarse spatial resolution leads to partial volume effects, which cause under- or overestimation of the sodium content at tissue boundaries. Fortunately, the SNR depends on additional parameters, such as k-space acquisition strategy, coil design, and magnetic field strength, which leave room for optimization. During the last decades, several ultrashort echo time (UTE) sequences (6–8) with non-Cartesian sampling patterns for sodium imaging have been presented in the literature and made it possible to trade some of the gained SNR for higher spatial resolution. The availability of MR scanners with ultrahigh magnetic field strength permits to increase the sensitivity even further, as the SNR scales approximately linearly with the main static magnetic field (B_0).

Because B_0 homogeneity decreases with increasing field strength, shimming and retrospective off-resonance correction are essential at ultrahigh field strength. In contrast to conventional MR systems, ultrahigh field scanners do normally not possess a proton body coil, which could be used for B_0 shimming and anatomical localization. While this can be done using the sodium signal, which has been shown to have a sufficiently high SNR at 9.4 Tesla (T) (9), proton imaging is still preferred due its higher sensitivity and consequently shorter acquisition times. In the past, dual-frequency coils (10) and nested-coil designs (11) were used to enable multinuclear imaging despite the fact that these setups almost inevitably compromise coil performance for both nuclei. In addition, due to the decreasing wavelength of the proton signal and the correspondingly strong B_1 inhomogeneity at 9.4T, highly complex multichannel transmit coils in combination with B_1-shimming would be required for acceptable image quality (12).

In this study, five healthy subjects were scanned at 9.4T to benefit from the higher NMR sensitivity compared with lower fields and to obtain sodium images of the human brain with a high spatial resolution, which should allow for more accurate sodium quantification due to reduced partial volume effects. A novel combination of a sodium birdcage coil with a proton patch antenna was used to preserve the efficiency of the X-nucleus coil while insuring a satisfactory coverage of the entire brain by proton imaging. Moreover, the impact of

[1]Department for Biomedical Magnetic Resonance, University of Tübingen, Tübingen, Germany.

[2]High-Field MR Center, Max Planck Institute for Biological Cybernetics, Tübingen, Germany.

*Correspondence to: Christian C. Mirkes, Dipl.-Phys., High-Field MR Center, Max Planck Institute for Biological Cybernetics, Spemannstr. 41, 72076 Tuebingen, Germany. E-mail: christian.mirkes@tuebingen.mpg.de

Received 2 July 2013; revised 4 December 2013; accepted 5 December 2013

DOI 10.1002/mrm.25096

Published online 16 January 2014 in Wiley Online Library (wileyonlinelibrary.com).

relaxation on the shape of the point-spread function (PSF) and the sodium quantification was evaluated through simulations.

METHODS

Technical Setup

All the measurements were performed on a Siemens (Erlangen, Germany) 9.4T whole-body MRI scanner equipped with a SC72 gradient system having a maximal amplitude of 40 mT/m and a maximal slew rate of 200 T/m/s. The sodium signal was acquired with a home-built 16-rung high-pass birdcage coil, which was driven in quadrature and had a resonance frequency of 105.7 MHz. The length and the diameter of the coil were 21 and 25 cm, respectively. A capacitively adjustable two channel patch antenna (13) placed closely behind the X-nucleus coil was used for excitation and reception of the proton signal (14).

Imaging Sequences

An acquisition weighted stack of spirals (AWSOS) (15) was used for the acquisition of sodium density weighted images. The nominal resolution of the sodium images was $1 \times 1 \times 5$ mm^3 and the readout duration was 20 ms. A rectangular RF pulse with a nominal flip angle of 90° and a duration of 500 μs was used for nonselective excitation of the sodium nuclei. Each partition-encoding gradient was prepared with the shortest possible duration and hence the time between the center of the RF pulse and the data acquisition varied between the chosen echo time (TE) of 0.30 ms for the central and 0.73 ms for the outermost partition. The repetition time (TR) was set to 150 ms to allow for a full recovery of the magnetization before each excitation. Further imaging parameters were: field of view (FOV) 240 mm^2, 44 partitions, and six averages. The measurement time for the sodium density weighted images was 30 min. In addition, gradient echo proton images (TE = 5 ms, TR = 200 ms) were acquired within 1 min for anatomical reference. The in-plane resolution and the slice thickness of these images were 1.4×1.4 mm^2 and 2.5 mm, respectively. The imaging protocols for the phantom and in vivo measurements were identical.

Non-Cartesian imaging sequences are susceptible to hardware imperfections such as gradient delays, but also to concomitant eddy currents generated by oscillating gradient waveforms in the conducting materials of the coils and the scanner. As has been shown previously (16), image quality can be significantly improved by measuring the actual trajectory taken in k-space. This measurement was performed using the proton signal with the method proposed by Duyn et al (17) on a spherical oil phantom placed inside the sodium coil. The gradient waveforms were multiplied by $\gamma_{23Na}/\gamma_{1H}$ to account for the different Larmor constants.

The image reconstruction of the nonuniformly sampled raw data was carried out in several steps on a standard PC using Matlab (The Mathworks, Natick, MA). First, Kaiser-Bessel gridding was performed for each partition (18). Then, a three-dimensional (3D) Hanning window was applied to the resampled signal to suppress high-frequency noise components. Finally, the filtered images were reconstructed by applying a 3D Fast Fourier transformation to the k-space.

Field Mapping and Correction

Although off-resonance artifacts are less severe for sodium than for proton imaging due to the lower gyromagnetic ratio, they can still degrade image quality significantly at ultrahigh field strength. Hence, B_0 shimming was performed based on the proton signal using the automatic shimming interface of the scanner. The resulting B_0 field distribution was mapped with a standard 2D Cartesian double-echo gradient echo proton sequence with $TE_1 = 3.1$ ms and $TE_2 = 3.9$ ms. Other acquisition parameters were: FOV 265×265 mm^2, bandwidth 500 Hz/pixel, acquisition time 2 min, slices 45, slice thickness 2.5 mm, and in-plane resolution 2×2 mm^2. Due to the lower gyromagnetic ratio of the sodium nucleus, the obtained frequency differences ($\Delta\omega$) had to be multiplied by $\gamma_{23Na}/\gamma_{1H}$.

Inhomogeneities of the local static magnetic field and concomitant gradient fields cause an unwanted phase accrual and lead to image blurring. Neglecting relaxation, the signal equation for an object with spin density $m(\boldsymbol{r})$ is given in this case by:

$$s(t) = \int m(\boldsymbol{r}) exp(-i2\pi \boldsymbol{k}(t) \cdot \boldsymbol{r} - i\Delta\omega(\boldsymbol{r})t - i\varphi_c(\boldsymbol{r}, \boldsymbol{G}(t), B_0))d\boldsymbol{r}, \quad [1]$$

where $\boldsymbol{k}(t)$ represents the k-space trajectory, $\boldsymbol{G}(t)$ the encoding gradients and φ_c the additional phase generated by concomitant fields. Because concomitant gradients and consequently φ_c are in a first order approximation inversely proportional to B_0, their contribution to the global phase can be neglected at ultrahigh field strength (19). The remaining off-resonance factor $exp(-i\Delta\omega(\boldsymbol{r})t)$ was approximated by a linear combination of Chebyshev polynomials, which allowed performing a retrospective correction of blurring artifacts for all images acquired with non-Cartesian imaging sequences (20).

The coil load dependent reference voltage (V_{90°), defined as the voltage required to achieve a 90° flip angle with a rectangular pulse within 500 μs, was estimated at the beginning of each scanning session by acquiring several free induction decays (FID) with different transmitter voltages (V) and a constant pulse duration (τ). These FIDs were then Fourier transformed and the absolute value of a sine was fitted to the central peak of the spectra:

$$S(V) = A\left|\sin\left(\frac{\pi}{2}\frac{V \cdot \tau}{V_{90^\circ} \cdot 500\ \mu s}\right)\right| + C, \quad [2]$$

where A and C are additional fitting parameters. Based on this reference voltage, the required power for all the pulses in the following experiments could be calculated by the scanner software. The actual spatial distribution of the B_1 field was mapped with the double-angle method (21) for retrospective correction. For this

purpose, two images with nominal flip angles of $\alpha = 45^\circ$ and $2\alpha = 90^\circ$ were acquired with the non-Cartesian sequence described above. The spatial resolution was reduced to $5 \times 5 \times 5$ mm^3 as the B_1 field is expected to vary smoothly across the imaged volume. The readout duration was 8 ms in this case and the acquisition time for each image was 5 min. Other parameters such as FOV, number of partitions, and TR remained unchanged. The actual flip angle map was calculated as follows:

$$\alpha_{actual}(\boldsymbol{r}) = \cos^{-1}\frac{I_2(\boldsymbol{r})}{2I_1(\boldsymbol{r})}, \quad [3]$$

where $I_1(\boldsymbol{r})$ and $I_2(\boldsymbol{r})$ are the signal intensities of the images acquired with flip angles of α and 2α, respectively. The signal intensity was corrected by multiplying the sodium density weighted images with the following scaling factor:

$$f_{B1} = \left(\sin\left(FA \cdot \frac{\alpha_{actual}}{\alpha}\right) \cdot \alpha_{actual}\right)^{-1}, \quad [4]$$

where FA is the nominal flip angle used for the acquisition of the TSC maps. The first factor in Eq. [4] describes the distribution of the actual flip angle and the second factor accounts for spatial differences in receive sensitivity of the birdcage coil, assuming that the transmit sensitivity is a good approximation of the receive sensitivity according to the principle of reciprocity (22).

The influence of the patch antenna on the performance of the sodium coil was evaluated by mapping the B_1 field produced by the latter in a large cylindrical phantom containing an aqueous solution of sodium chloride (75 mM) with and without the presence of the patch antenna. Six images were acquired for different transmitter voltages and a sine (Eq. [2]) was fitted to the signal intensity on a voxel-by-voxel basis. The advantage of this approach over the double angle method is that it works for a much larger range of flip angles. However, it requires a longer acquisition time, which makes it less suitable for in vivo measurements. The TR was set to 250 ms resulting in a measurement time of 5 min per image. In the first setting the antenna was present and used to calculate optimal shim currents. The same shim currents were also used for the second setting without the antenna.

Point-Spread Function

The resolution of an MR image is determined by many factors such as the filters which are applied to the raw images, the PSF given by the k-space sampling pattern, and the blurring introduced by the T_2* decay of the received signal itself. As a matter of fact, the spatial resolution depends not only on the sequence parameters but also on the physical properties of the matter contained in the voxel. The effective PSF, incorporating all the aforementioned contributions, was simulated for different T_2* values including the used Hanning filter to estimate the expected final resolution. The following biexponential model function was used to mimic the relaxation properties of sodium in tissue (5):

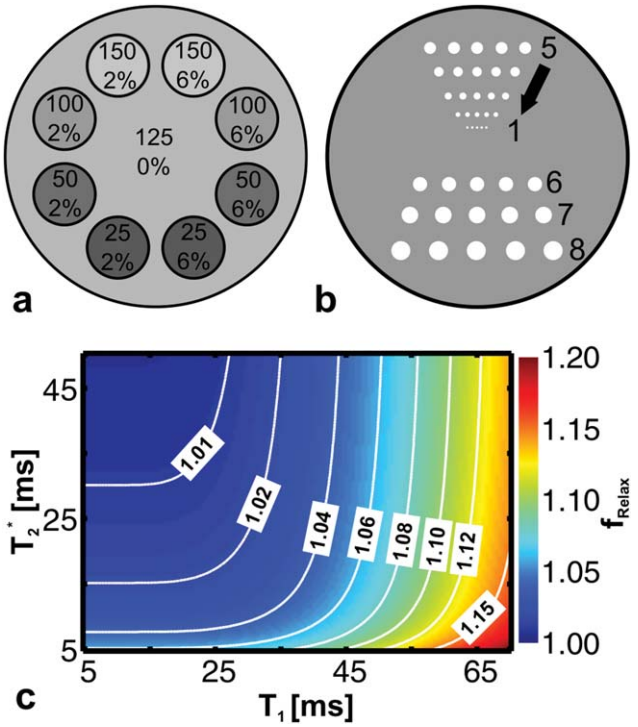

FIG. 1. **a**: Schematic representation of the phantom with sodium concentrations given in mM and agarose content in percent. **b:** Resolution plate with hole diameters ranging from 1 to 8 mm. **c:** Relaxation correction factor (Eq. [7]) for different T_1 and T_2* values assuming $\theta = 90^\circ$, TE = 0.3 ms, and TR = 150 ms.

$$R(t) = 0.6\ \exp\left(-\frac{t}{T_{2f}}\right) + 0.4\ \exp\left(-\frac{t}{T_{2s}}\right), \quad [5]$$

where T_{2f} and T_{2s} are the fast and slow components of the transverse relaxation.

The function *deconvblind* provided by Matlab (R2010a) (see Matlab documentation for more details) was used to perform a blind deconvolution of an image slice and obtain experimentally a 2D estimate of the effective PSF, which was then compared with the simulations.

MRI Phantoms and Human Subjects

The validation of the methods used for sodium quantification was performed on a phantom containing two sets of four tubes each filled with 2% and 6% w/w agarose (Sigma-Aldrich) gels, respectively (Fig. 1a). The gels were prepared by adding agarose crystals to aqueous solutions of sodium chloride with concentrations of 25, 50, 100, and 150 mM. The solutions were heated in an autoclave before being poured into the tubes, which were then immersed in a cylindrical container filled with a 125 mM solution of sodium chloride. Moreover, a 1-cm-thick Plexiglas plate with holes of different diameters was added to assess the achieved resolution (Fig. 1b).

Sodium density weighted images can only be converted to meaningful TSC maps if an adequate reference standard is available. In this study, the subjects' head rested on a cushion which was made of silicone-

caoutchouc and contained six compartments filled with agarose gels. These gels (2% w/w agarose) were prepared as described above and had the following sodium concentrations: 25, 50, 75, 100, 125, and 150 mM NaCl.

The T_1 relaxation times of the gels and the aqueous NaCl solution were measured by an inversion recovery experiment using the non-Cartesian sampling pattern described above and the following inversion times (TI): 6, 12, 18,..., 66 ms. The duration of the inversion pulse was set to 1.0 ms to stay within SAR limits. The TR was TI+200 ms and the total scanning time was 45 min for a spatial resolution of $3 \times 3 \times 5$ mm^3. Although the longitudinal relaxation is expected to be biexponential in the agarose gels, only a monoexponential fit was performed on a voxel-by-voxel basis, because the theoretical ratio of the fast and slow component is merely 1/4 (5) and the minimal achievable TIs do not allow for accurate determination of the value of the short component. The measured longitudinal relaxation times were 56.5 ± 1.0 ms for the NaCl solution, 45.7 ± 1.5 ms for the 2% agrarose gels and 31.0 ± 2.1 ms for the 6% agrarose gels.

The T_2* relaxation times were estimated by acquiring 11 sets of images with a multiecho AWSOS sequence. Each set consisted of five echoes spaced by 8.53 ms. The TEs of the first echo for each set were: 0.3, 1, 2, 3,..., 10 ms. The resolution was the same as for the T_1 measurement and the TR was 200 ms, which led to a measurement time of 38 min. A monoexponential fit was used to estimate the transverse relaxation time of sodium in aqueous solution ($T_2^* = 55.1 \pm 1.3$ ms), while a biexponential fit allowed determining T_{2f} and T_{2s} of the gels (2% agarose gels: $T_{2f} = 9.8 \pm 0.7$ ms, $T_{2s} = 32.5 \pm 2.7$ ms; 6% agarose gels: $T_{2f} = 4.0 \pm 0.2$ ms, $T_{2s} = 26.3 \pm 1.3$ ms). The ratio of the slow and fast component was fixed (Eq. [5]) because biexponential fitting is very error-prone, especially if many free parameters are available.

In accordance with local research ethics policies and procedures, the five healthy volunteers (4 males, 1 female, average age: 29 ± 4 years) underwent a physical health check performed by a local physician before being recruited for this study. Each of them provided written informed consent before the MR examination.

SNR Measurement

The SNR for a region of interest (ROI) was calculated by the following formula:

$$\mathrm{SNR} = 0.655 \ \frac{S}{\sigma} \ , \qquad [6]$$

where S is the mean signal intensity in the ROI and σ the apparent standard deviation (SD) of the noise in multiple regions in the background. The correction factor of 0.655 accounts for the fact that the SNR was determined from magnitude images (23).

In Vivo TSC Maps

To perform a signal calibration, a ROI spanning over several image slices was drawn in each compartment of the reference cushion and the mean signal intensity was calculated. Based on the previously determined values for T_1, T_{2f}, and T_{2s}, the signal intensities of the gels were corrected for relaxation effects with the following factor (24):

$$f_{Relax} = \left(\frac{1 - exp\left(-\frac{TR}{T_1}\right)}{1 - \cos\theta \cdot exp\left(-\frac{TR}{T_1}\right)} \cdot \left(0.6 \ \exp\left(-\frac{TE}{T_{2f}}\right) + 0.4 \ \exp\left(-\frac{TE}{T_{2s}}\right)\right)\right)^{-1}, \qquad [7]$$

where θ is the actual flip angle achieved during the acquisition of the sodium density weighted images.

A linear calibration was performed to relate the corrected signal intensity to the sodium concentration (C) and vice versa:

$$\mathrm{I} = a \cdot \mathrm{C} + b. \qquad [8]$$

Caution was taken that all the reference samples used for the calibration exhibited a sufficient SNR, because the magnitude operation will reduce the apparent SD of the signal intensity in a ROI in case of low SNR and artificially increase the mean signal intensity. In general, sodium concentrations can only be calibrated or quantified if the SNR is sufficiently high ($\gtrsim$5). The parameter b in Eq. [8] was set to zero, because there should be no offset if the aforementioned condition is fulfilled.

If the T_1 and T_2* values of the human tissue were known for each voxel, the signal intensity could be corrected for relaxation effects to improve the accuracy of the TSC maps. However, such measurements require an unacceptable long scanning time and were therefore not performed. Instead, the images were directly converted to TSC maps based on the calibration parameter from Eq. [8]. The factor f_{Relax} given in Eq. [7] was calculated for different values of T_1 and T_2* (monoexponential) to estimate the quantification error caused by omitting the intensity correction for relaxation effects. According to Figure 1c, the relative error is well below 10% for typical values of T_1 (25–40 ms) and T_2* ($T_{2f} = 2$–5 ms, $T_{2s} = 15$–25 ms) found in human brain tissue (25). For cerebrospinal fluid (CSF) or vitreous humor ($T_1 \approx T_2^* \approx 55$ ms), however, the relative error can reach up to 8%.

RESULTS

PSF and Resolution

Figures 2a,b show the simulated PSF with the sequence parameters used for the acquisition of the sodium density weighted images in case of no, mono-, and biexponential relaxation. T_{2f} and T_{2s} were chosen to be comparable to values found in human brain. The measured full width at half maximum (FWHM) is equal to twice the voxel size in each direction if the signal is not affected by relaxation. The width of the effective PSF is determined in this case only by the k-space sampling pattern and the Hanning filter. If a monoexponential decay is assumed, the FWHM in the plane of highest resolution, defined as the xy-plane, increases to 2.3 ($T_2^* = 15$ ms) or 2.9 ($T_2^* = 5$ ms) voxels, respectively. A biexponential relaxation ($T_{2f} = 5$ ms, $T_{2s} = 15$ ms)

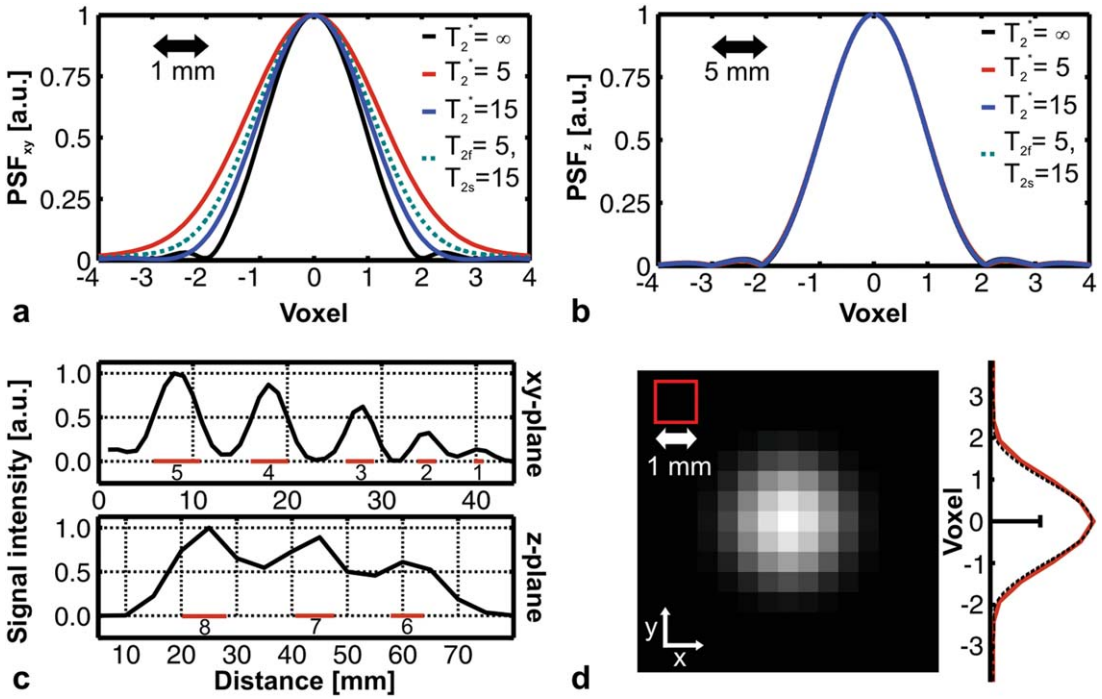

FIG. 2. **a**: Simulated PSF in the plane of highest resolution in case of no, mono-, and biexponential relaxation. **b:** PSF in the z-plane. The FWHM is only slightly influenced by relaxation effects. **c:** Profiles of the signal intensity through holes of different diameters in the xy- and z-plane. The bars below the peaks indicate the expected diameter in millimeter. **d:** Interpolated estimate of the PSF_{xy} obtained by blind-deconvolution. The PSF is symmetric and has a FWHM of 2.3 mm, which is slightly higher than the width of the simulated PSF (dashed line) for $T_2^* = 55$ ms.

results in a FWHM of 2.5 voxels. Owing to the short encoding time in partition-direction, the FWHM of the PSF is only marginally broadened due relaxation effects and predominantly determined by the k-space filter.

Profiles along the holes with diameters ranging from 1 to 5 mm in the xy-plane and 6 to 8 mm in the z-plane are shown in Figure 2c. All holes with diameters down to 2 mm could be easily resolved in the plane of highest resolution. However, the smallest holes with a diameter of only 1 mm are significantly blurred, indicating that the actual spatial resolution was approximately two times lower ($2 \times 2 \times 10$ mm^3) than defined by the sequence parameters. The same holds true for the observed resolution in the z-plane, where the spacing of the holes was insufficient to obtain well separated peaks. Figure 2d shows the estimated PSF_{xy} obtained by blindly deconvolving a slice containing the resolution plate. The FWHM (2.3 mm) of the PSF is slightly higher than would be expected from the simulations for sodium in aqueous solution with a transverse relaxation time of approximately 55 ms.

Field Mapping and Calibration

Figure 3a depicts the B_1 field distribution of the sodium birdcage coil with and without the presence of the patch antenna. The difference image (Fig. 3b) demonstrates that the observed patterns are similar except for regions close to the patch antenna. Because the shim currents could not be recalculated after the removal of the patch antenna, it is likely that large frequency shifts occurred at the bottom of the phantom once facing the antenna and lead to a reduction of the flip angle is these areas. Moreover, the patch antenna might act as an endcap to the birdcage and increase its efficiency, which would explain the higher B_1 seen in the map made with the patch antenna present (26). Inaccurate repositioning of the phantom after removing the patch antenna is another source of error, which should, however, only contribute slightly to the observed differences. Nevertheless, the field distributions are similar enough to conclude that the patch antenna has only a slight influence on the B_1 field of the birdcage or might even improve the latter.

Figure 4a shows the B_0 map for the phantom and the reference cushion. The largest frequency shifts occur in the

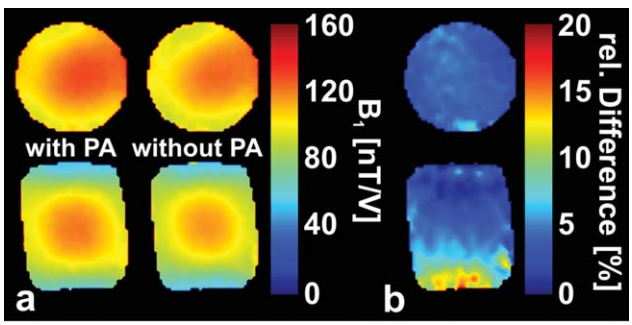

FIG. 3. **a**: B_1 maps of the sodium birdcage coil with and without the patch antenna (PA) present. **b:** Difference image demonstrating that the field distribution is similar in both settings except for regions close to the patch antenna (bottom of the phantom).

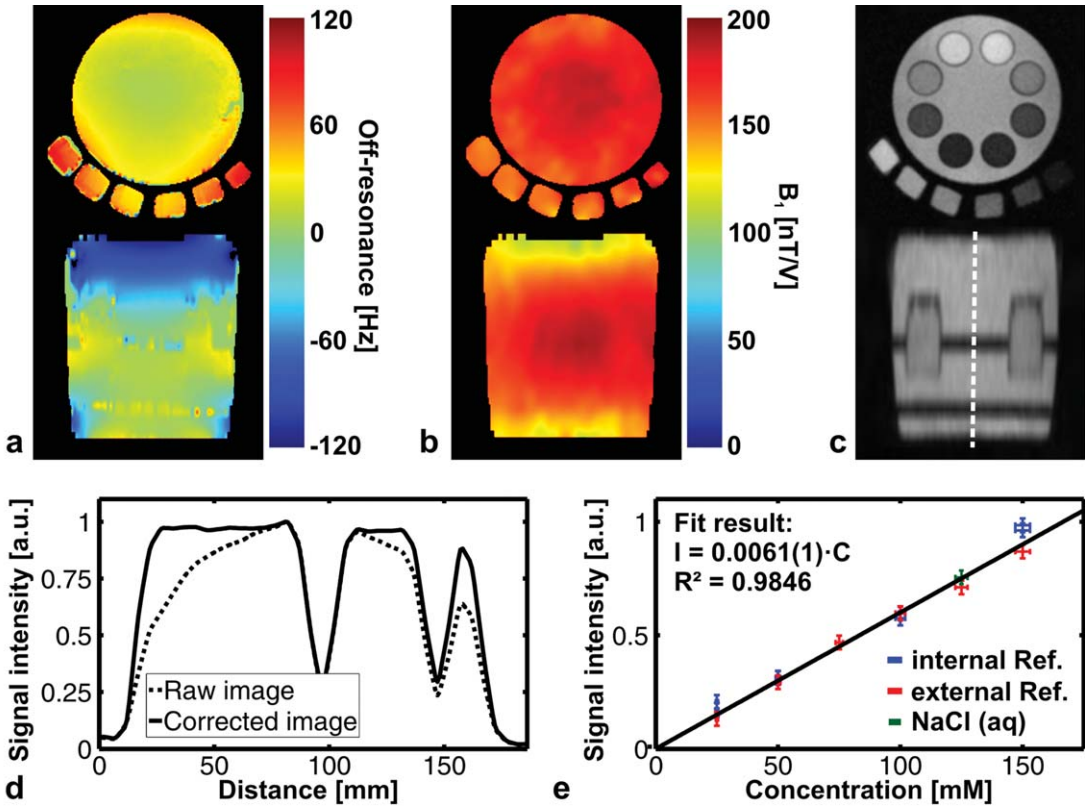

FIG. 4. **a**: B_0 map showing the off-resonance frequency for the sodium nuclei in Hz. **b:** Spatial distribution of the B_1 field produced by the sodium birdcage coil. **c:** Sodium density weighted images after combined B_0 and B_1 correction. The images were interpolated along the partition-encoding direction (bottom) to match the in-plane resolution. **d:** Profile through the phantom corresponding to the dashed line shown in (c) before and after intensity correction. **e:** Relaxation corrected signal intensities of the aqueous solution, the internal (phantom), and the external (cushion) reference samples versus known sodium concentration.

gels of the reference cushion and at the top of the phantom. The range of measured off-resonance frequencies for the sodium nuclei is approximately 240 Hz after shimming. The B_1 field produced by the birdcage is highest in the center of the phantom and slowly falls off toward both ends of the coil (Fig. 4b). Sodium density weighted images after B_0 and B_1 correction are shown in Figure 4c. A profile through the phantom before and after intensity correction demonstrates its effectiveness (Fig. 4d). The signal intensities of 15 ROIs selected in the aqueous NaCl solution and the gels of the phantom and the reference cushion were corrected for relaxation effects according to Eq. [7] and plotted against the known sodium concentrations. The error on the concentration values was assumed to be 2% to account for possible inaccuracies which occurred during the preparation of the gels. The error on the signal intensity was estimated by the standard deviation measured in the selected ROIs. A linear regression was performed to obtain the slope of the calibration line (Eq. [8]). The coefficient of determination $R^2 = 0.9846$ indicates that the data is well approximated by a linear model (Fig. 4e). B_0 inhomogeneity as seen at the edge of the FOV and imperfect B_1 correction can affect the signal intensity and increase the spread of the data points along the regression line. If the calibration parameter was determined based on the reference samples in the cushion and used to transform the image shown in Figure 4c into a sodium concentration map, then the mean relative error on the concentration of the gels in the cylindrical phantom would be around 8%.

In Vivo Measurements

For consistency, all in vivo images presented in the figures are taken from the first of the five healthy human subjects if not stated otherwise. Figure 5a shows gradient echo proton images acquired with the patch antenna. The spatial distribution of the B_1 field produced by the birdcage coil is depicted in Figure 5b. A Gaussian filter was applied to smooth the maps for the B_1 correction. Note that the double-angle method was not able to accurately determine the B_1 value below the cerebellum, because the achieved flip angle in these areas was below the limit of resolvability of the mapping method. Shimming allowed to homogenize the B_0 field (Fig. 5c) over the brain and reduced the range of off-resonances to 10–30 Hz within the upper brain and to approximately 100 Hz in the lower brain and areas close to the sinuses. The conjugate phase reconstruction could improve image quality in certain areas even further as demonstrated in Figure 5d,e, where off-resonance artifacts around the subject's eyes and in the brain were mitigated.

Figure 6 shows transverse, coronal, and sagittal sodium images of the five subjects before B_0 and B_1

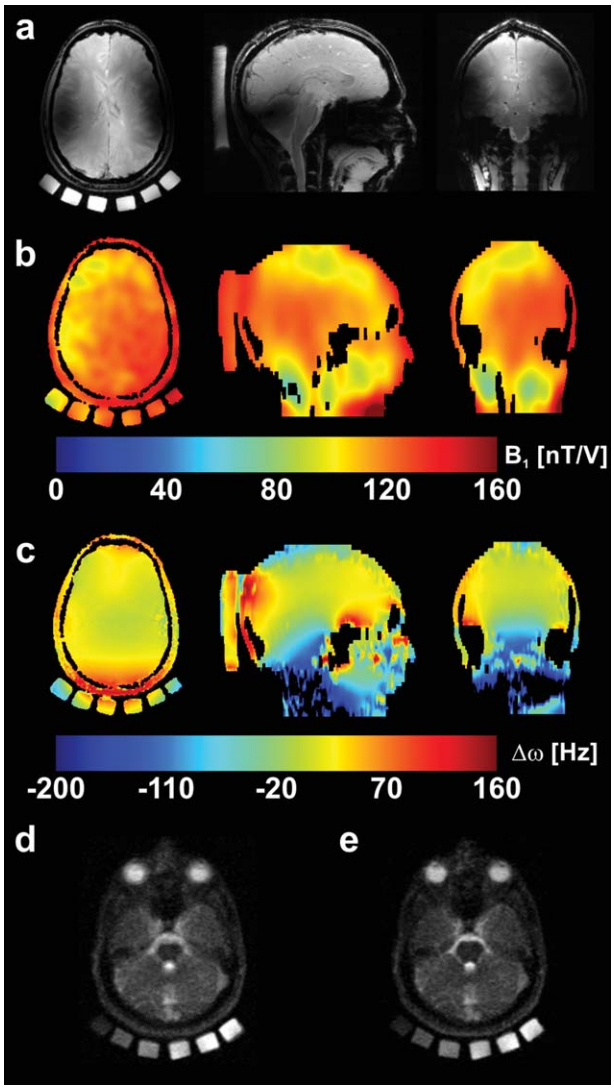

FIG. 5. **a**: Proton images serving as anatomical reference. **b:** Spatial B_1 field distribution produced by the ^{23}Na birdcage coil. **c:** B_0 field maps showing the off-resonance frequency for the sodium nucleus in Hz. **d**: Sodium raw image before B_0 field correction. **e:** Blurring artifacts around the eyes and in the brain could be reduced by the fast conjugate phase reconstruction.

correction. Based on these images, the SNR was determined according to Eq. [6] for seven ROIs: white and gray matter in the prefrontal cortex, CSF, vitreous humor, and three gels of the reference cushion (25, 50, and 75 mM). The corresponding values as well as the mean, minimum, and maximum values found across the subjects are summarized in Table 1. Similar results are found in the different ROIs for all the subjects. Due to its high sodium concentration and its location in the center of the brain, the CSF exhibits the highest SNR with an average value of 35. White and gray matter only reach a SNR of 8 and 9, respectively.

TSC maps were calculated for each of the five volunteers using the six reference samples contained in the cushion. The TSC maps for the first volunteer are shown in Figure 7. The CSF in the ventricles and the sulci of the brain can be well discerned due to its high sodium concentration. Table 2 summarizes the sodium concentrations measured in four ROIs: white and gray matter in the prefrontal cortex, CSF, and vitreous humor. The concentrations of CSF and vitreous humor given in Table 2 were corrected for relaxation effects according to Eq. [7] assuming T_1 and T_2 to be identical to the values determined for the 125 mM NaCl solution of the phantom. The average sodium concentration in white matter, gray matter, CSF and vitreous humor was 31 ± 1, 36 ± 2, 125 ± 6, and 134 ± 5 mmol/L of wet tissue, respectively. The error on the values reported in Table 2 was estimated to be 10% considering the standard deviation of the signal in the selected ROIs, the error caused by omitting the correction for relaxation effects, and other possible inaccuracies due to not entirely corrected B_0 and B_1 inhomogeneities.

DISCUSSION

In this study, we have shown that it is possible to obtain TSC maps with a high spatial resolution at ultrahigh field strength. In the phantom experiment, the real resolution was estimated to be up to two times lower than specified by the sequence parameters. The resolution achieved in vivo is difficult to assess quantitatively, but will be in most cases lower than predicted by the phantom measurement due to through-plane partial volume effects, shorter transverse relaxation times, and possible motion of the subject's head during the measurement.

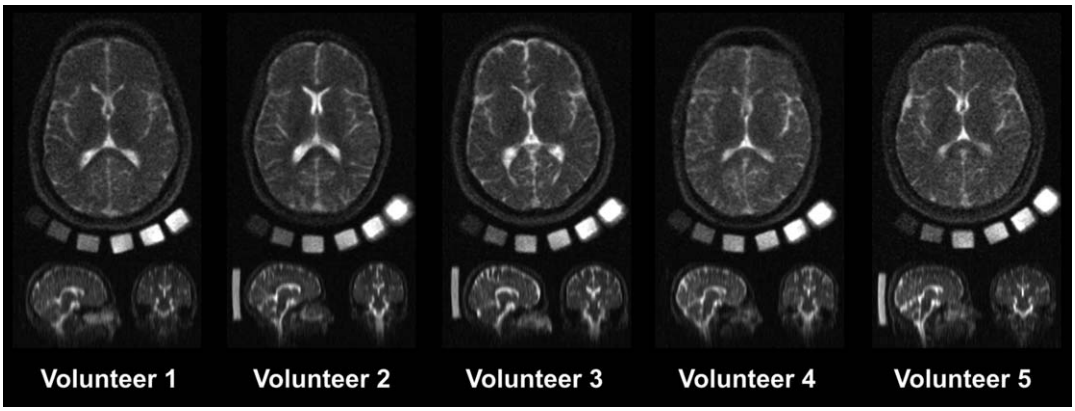

FIG. 6. Transverse, sagittal, and coronal sodium images of the five subjects before B_0 and B_1 correction.

Table 1
SNR of Gray Matter, White Matter, CSF, Vitreous Humor, and Three Gels of the Reference Cushion[a]

Volunteer	Gray matter	White matter	CSF	Vitreous humor	Ref.25 mM	Ref.50 mM	Ref.75 mM
1	8	8	32	24	7	12	18
2	11	10	43	37	8	16	25
3	9	8	35	28	7	14	22
4	11	9	37	33	8	15	24
5	8	7	30	23	6	12	19
Minimum	8	7	30	23	6	12	18
Maximum	11	10	43	37	8	16	25
Mean±SD	9±2	8±1	35±5	29±6	7±1	14±2	22±3

[a]The calculated standard deviation for all SNR values is approximately one. The lowest, highest, and mean values are given at the bottom of the table.

The long acquisition time for the sodium images could be shortened up to a certain degree without decreasing the SNR by adding a receive-array to the birdcage coil to increase the sensitivity (27).

Although the real voxel size was roughly 40 μL, partial volume effects in the partition-encoding direction could still lead to considerable quantification errors as can be seen from the CSF values reported in Table 2, which are outside the normal range (135–150 mM). Due to the large concentration difference between CSF and tissue, already small partial volume effects can lead to a significant drop of the measured signal intensity. The same problem arises when determining the sodium concentration of the gray matter on the highly convoluted cortex. In this case, the value of the TSC is overestimated. The sodium concentrations measured in vitreous humor are approximately in the expected range owing to the size of the eye. Moreover, note that the B_1 correction leads to systematically lower sodium concentrations for fluids, because the double angle method overestimates the achieved flip angle for nuclei affected by saturation. As has been shown previously (15), a high spatial resolution is essential for accurate TSC mapping, because the measured sodium concentrations increase significantly with increasing voxel size due to partial volume effects. The same effect was also noted in the present study when the images were reconstructed with a smaller spatial resolution. If the in-plane resolution was decreased by a factor of two in each direction, the TSC for gray matter increased by more than 30%.

TSC and SNR values from several previous studies performed over the last ten years are listed in Table 3. The improved sensitivity at higher field strength permitted increasing the spatial resolution considerably. The highest actual resolution was achieved in a study at 7T (15) at the expense of the available SNR. Taking the

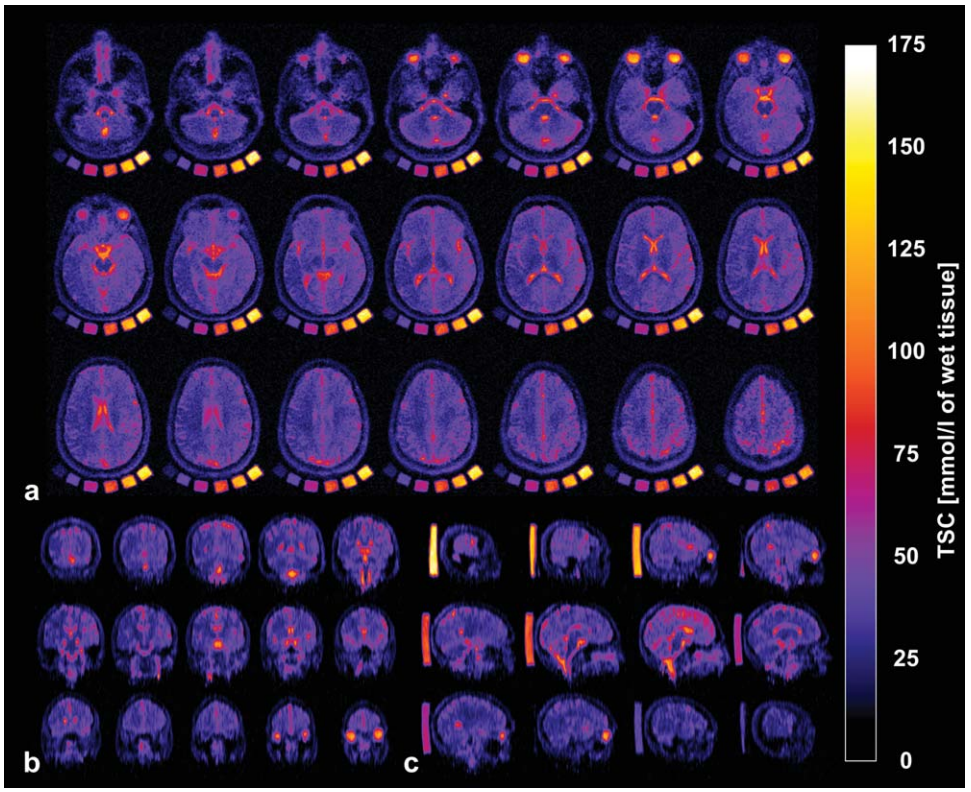

FIG. 7. TSC maps. Note that no correction for relaxation effects has been performed for the TSC values. The transverse slices (**a**) exhibit a higher spatial resolution than the coronal (**b**) and sagittal (**c**) ones because of the asymmetric voxel size used for the acquisition.

Table 2
Mean Sodium Concentration in Four ROIs in Millimoles per Liter Voxel Volume: White and Gray Matter in the Prefrontal Cortex, CSF, and Vitreous Humor [a]

	[years]	[mmol/L of wet tissue]		[mmol/L]	
Volunteer	Age	White matter	Gray matter	CSF	Vitreous humor
1	27	30 ± 3	34 ± 3	124 ± 12	134 ± 13
2	24	31 ± 3	35 ± 4	128 ± 13	135 ± 14
3	34	31 ± 3	38 ± 4	131 ± 13	127 ± 13
4	28	29 ± 3	36 ± 4	115 ± 12	136 ± 14
5	30	32 ± 3	37 ± 4	127 ± 13	140 ± 14
Mean ± SD	29 ± 4	31 ± 1	36 ± 2	125 ± 6	134 ± 6

[a]The ROIs were selected based on the proton images acquired for each subject. The concentrations of the CSF and the vitreous humor given in this table were corrected for relaxation effects assuming $T_1 = 56.5$ ms and $T_2 = 55.1$ ms.

differences in voxel volume into account, the SNR per unit time reached for CSF was in the current study more than 50% higher. The TSC values measured here are, although somewhat lower, close to the theoretical value of approximately 34 mmol/L of wet tissue (28) and are comparable to values reported in previous studies at high and ultrahigh field strength. The slightly lower values may in part be due to the fact that no correction for relaxation effects was performed. Although independent validation of the sodium concentrations found in the human brain would be desirable, the invasive nature of the available chemical and physical methods makes their application challenging.

If external reference samples placed at the edge of the FOV are used for calibration, B_0 and B_1 inhomogeneities can cause quantification errors, which can be mitigated by adequate correction methods. Internal references, such as CSF, are far less affected by these problems. However they suffer from different shortcomings such a partial volume effects, limited number of samples, and perhaps imprecisely known relaxation times and ^{23}Na concentrations. It is for these reasons that no internal references were used for signal calibration in this study. A third possibility to perform a signal calibration is to run a separate scan with a phantom mimicking the electrical properties of a human head and containing an adequate number of reference samples (29). This method relies on the assumption that the loading of the coil is the same for the phantom and the in vivo measurement, which might be difficult to achieve in all cases.

The use of the patch antenna and the proton instead of the sodium signal should not have a significant influence on the accuracy of the trajectory measurements, because the gradient delays do not depend on the coil or the nucleus used for measuring them as long as the entire coil setup remains unchanged. Moreover, the trajectory measurement provides a valid first order approximation of trajectory deviations caused by eddy currents, even if the gradients used during the actual sodium measurements are approximately four ($\gamma_{1H}/\gamma_{23Na}$) times stronger. Trajectory

Table 3
TSC and SNR Values Measured in Previous Studies Performed over the Past 10 Years

		[min]	[mm^3]	[μL]		[mmol/L of wet tissue]		[mmol/L]	
Year	[T] Field	Scan time	Nominal resolution (Actual res.)	Voxel volume (Actual vol.)	SNR	Gray matter	White matter	CSF	Ref.
Present study	9.4	30	1.0 × 1.0 × 5.0 (2.0 × 2.0 × 10.0)	5 (40)	9[a], 35[b]	36 ± 2	31 ± 1	125 ± 6	-
2012	7	32	0.9 × 0.9 × 4.0 (1.6 × 1.6 × 5.4)[c]	3 (14)	7[b]	47 ± 7	37 ± 3	145[d]	(15)
2011	9.4	10	5.0 × 5.0 × 5.0 (7.9 × 7.9 × 7.9)[e]	125 (493)	-	-	31 ± 6	128 ± 5	(29)
		10	2.9 × 2.9 × 2.9 (5.7 × 5.7 × 5.7)[e]	24 (185)			31 ± 6	142 ± 6	
2011	3	8	5.0 × 5.0 × 5.0 (8.7 × 8.7 × 8.7)[e]	125 (659)	-	-	30 ± 7	135 ± 15	(29)
		8	3.9 × 3.9 × 3.9 (8.0 × 8.0 × 8.0)[e]	59 (512)			31 ± 7	136 ± 10	
2010	3	8	5.0 × 5.0 × 5.0 (7.5 × 7.5 × 7.5)[e]	125 (512)	-	29 ± 1	38 ± 1	-	(28)
2010	3	16	4.0 × 4.0 × 4.0	64	-	30 ± 5[f]	19 ± 5[f]	-	(30)
2008	4.7	11	3.0 × 3.0 × 3.0	27	22[a]	-	-	-	(31)
2007	9.4	6	3.0 × 3.0 × 3.0	27	-	-	-	-	(32)
2007	1.5	10	4.0 × 4.0 × 4.0	64	32[a],43[b]	-	-	-	(33)
			4.0 × 8.0 × 10.0	320	19[a],34[b]				
2006	4	30	7.5 × 7.5 × 7.5	422	17[a],23[b]	-	-	-	(34)
2003	1.5	15	3.4 × 3.4 × 3.4 (5.8 × 5.8 × 5.8)	39 (200)	-	62 ± 6	72 ± 11	135 ± 10	(2)

[a]Brain tissue.
[b]CSF.
[c]In-plane resolution measured, slice thickness estimated.
[d]Literature value used for calibration.
[e]Estimated true resolution for brain parenchyma based on the FWHM of the PSF.
[f]Frontal lobe of healthy subjects.

measurements of the unscaled gradients strongly dephased the proton spins and resulted in measured k-space trajectories of poor quality. The possibility to use the sodium signal directly for the trajectory measurement was not investigated in this study because of the short T_2* values and low SNR compared with protons.

CONCLUSIONS

This study has demonstrated that ultrahigh field MRI offers a great potential for sodium imaging due to the higher available SNR. The small voxel size permitted to reduce partial volume effects and should allow a more accurate quantification of the TSC of the human brain. Nevertheless, the achieved resolution is still too low to resolve the minute structures in the human brain. Because B_0 and B_1 homogeneity decrease with increasing field strength, suitable correction methods are indispensable at 9.4T to obtain images of acceptable quality. As ultrahigh field systems do not normally possess a body coil, which could be used for proton imaging, the usage of a patch antenna in conjunction with a sodium birdcage coil provided a convenient solution to combine proton and X-nucleus imaging without having to make any modification to either appliance.

ACKNOWLEDGMENTS

This work was funded in part by the Helmholtz Alliance ICEMED - Imaging and Curing Environmental Metabolic Diseases, through the Initiative and Networking Fund of the Helmholtz Association.

REFERENCES

1. Walker HK, Hall WD, Hurst JW. Clinical methods: the history, physical, and laboratory examinations. Boston: Butterworths; 1990.
2. Ouwerkerk R, Bleich KB, Gillen JS, Pomper MG, Bottomley PA. Tissue sodium concentration in human brain tumors as measured with 23Na MR imaging. Radiology 2003;227:529–537.
3. Borthakur A, Shapiro EM, Beers J, Kudchodkar S, Kneeland JB, Reddy R. Sensitivity of MRI to proteoglycan depletion in cartilage: comparison of sodium and proton MRI. Osteoarthr Cartil 2000;8:288–293.
4. Borthakur A, Mellon E, Niyogi S, Witschey W, Kneeland JB, Reddy R. Sodium and T1rho MRI for molecular and diagnostic imaging of articular cartilage. NMR Biomed 2006;19:781–821.
5. Rooney WD, Springer CS. A comprehensive approach to the analysis and interpretation of the resonances of spins 3/2 from living systems. NMR Biomed 1991;4:209–226.
6. Boada FE, Gillen JS, Shen GX, Chang SY, Thulborn KR. Fast three dimensional sodium imaging. Magn Reson Med 1997;37:706–715.
7. Nagel AM, Laun FB, Weber MA, Matthies C, Semmler W, Schad LR. Sodium MRI using a density-adapted 3D radial acquisition technique. Magn Reson Med 2009;62:1565–1573.
8. Qian Y, Zhao T, Hue YK, Ibrahim TS, Boada FE. High-resolution spiral imaging on a whole-body 7T scanner with minimized image blurring. Magn Reson Med 2010;63:543–552.
9. Atkinson IC, Lu A, Thulborn KR. Preserving the accuracy and resolution of the sodium bioscale from quantitative sodium MRI during intrasubject alignment across longitudinal studies. Magn Reson Med 2012;68:751–761.
10. Shen GX, Boada FE, Thulborn KR. Dual-frequency, dual-quadrature, birdcage RF coil design with identical b1 pattern for sodium and proton imaging of the human brain at 1.5 T. Magn Reson Med 1997;38:717–725.
11. Wiggins GC, Brown R, Fleysher L, Zhang B, Stoeckel B, Inglese M, Sodickson DK. A nested dual frequency birdcage/stripline coil for sodium/proton brain imaging at 7T. In Proceedings of the 18th Annual Meeting of ISMRM, Stockholm, Sweden, 2010. Abstract 1500.
12. Hoffmann J, Shajan G, Scheffler K, Pohmann R. Numerical and experimental evaluation of RF shimming in the human brain at 9.4 T using a dual-row transmit array. MAGMA 2014;27:373–386.
13. Hoffmann J, Shajan G, Budde J, Scheffler K, Pohmann R. Human brain imaging at 9.4 T using a tunable patch antenna for transmission. Magn Reson Med 2013;69:1494–1500.
14. Mirkes CC, Hoffmann J, Shajan G, Pohmann R, Scheffler K. Combination of a sodium birdcage coil with a tunable patch antenna for B0 shimming and anatomical localization at 9.4 T. In Proceedings of the 21st Annual Meeting of ISMRM, Salt Lake City, Utah, USA, 2013. Abstract 1982.
15. Qian Y, Zhao T, Zheng H, Weimer J, Boada FE. High-resolution sodium imaging of human brain at 7 T. Magn Reson Med 2012;68:227–233.
16. Lu A, Atkinson IC, Vaughn JT, Thulborn KR. Impact of gradient timing error on the tissue sodium concentration bioscale measured using flexible twisted projection imaging. J Magn Reson 2011;213:176–181.
17. Duyn JH, Yang Y, Frank JA, van der Veen JW. Simple Correction Method for k-Space Trajectory Deviations in MRI. J Magn Reson 1998;132:150–153.
18. Jackson JI, Meyer CH, Nishimura DG, Macovski A. Selection of a convolution function for Fourier inversion using gridding. IEEE Trans Med Imaging 1991;10:473–478.
19. Norris DG, Hutchison JMS. Concomitant magnetic field gradients and their effects on imaging at low magnetic field strengths. Magn Reson Imaging 1990;8:33–37.
20. Chen W, Sica CT, Meyer CH. Fast conjugate phase image reconstruction based on a Chebyshev approximation to correct for B0 field inhomogeneity and concomitant gradients. Magn Reson Med 2008;60:1104–1111.
21. Stollberger R, Wach P, McKinnon G, Justich E, Ebner F. Rf-field mapping in vivo. In Proceedings of the 7th Annual Meeting of ISMRM, San Francisco, California, USA, 1988. Abstract 106.
22. Hoult DI. The principle of reciprocity in signal strength calculations–a mathematical guide. Concepts Magn Reson 2000;12:173–187.
23. Henkelman RM. Measurement of signal intensities in the presence of noise in MR images. Med Phys 1985;12:232–233.
24. Madelin G, Lee JS, Inati S, Jerschow A, Regatte RR. Sodium inversion recovery MRI of the knee joint in vivo at 7T. J Magn Reson 2010;207:42–52.
25. Ouwerkerk R. Magnetic resonance neuroimaging. Methods Mol Biol 2011;711:175–201.
26. Alecci M, Collins CM, Wilson J, Liu W, Smith MB, Jezzard P. Theoretical and experimental evaluation of detached endcaps for 3 T birdcage coil. Magn Reson Med 2003;49:363–370.
27. Qian Y, Zhao T, Wiggins GC, Wald LL, Zheng H, Weimer J, Boada FE. Sodium imaging of human brain at 7 T with 15-channel array coil. Magn Reson Med 2012;68:1807–1814.
28. Lu A, Atkinson IC, Claiborne TC, Damen FC, Thulborn KR. Quantitative sodium imaging with a flexible twisted projection pulse sequence. Magn Reson Med 2010;63:1583–1593.
29. Atkinson IC, Lu A, Thulborn KR. Clinically constrained optimization of flexTPI acquisition parameters for the tissue sodium concentration bioscale. Magn Reson Med 2011;66:1089–1099.
30. Inglese M, Madelin G, Oesingmann N, Babb JS, Wu W, Stoeckel B, Herbert J, Johnson G. Brain tissue sodium concentration in multiple sclerosis: a sodium imaging study at 3 tesla. Brain 2010;133:847–857.
31. Stobbe R, Beaulieu C. Advantage of sampling density weighted apodization over postacquisition filtering apodization for sodium MRI of the human brain. Magn Reson Med 2008;60:981–986.
32. Atkinson IC, Renteria L, Burd H, Pliskin NH, Thulborn KR. Safety of human MRI at static fields above the FDA 8T guideline: sodium imaging at 9.4T does not affect vital signs or cognitive ability. J Magn Reson Imaging 2007;26:1222–1227.
33. Nielles-Vallespin S, Weber M-A, Bock M, Bongers A, Speier P, Combs SE, Wohrle J, Lehmann-Horn F, Essig M, Schad LR. 3D radial projection technique with ultrashort echo times for sodium MRI: clinical applications in human brain and skeletal muscle. Magn Reson Med 2007;57:74–81.
34. Romanzetti S, Halse M, Kaffanke J, Zilles K, Balcom BJ, Shah NJ. A comparison of three SPRITE techniques for the quantitative 3D imaging of the 23Na spin density on a 4T whole-body machine. J Magn Reson 2006;179:64–72.

PUBLICATION 2

FULL PAPER

Magnetic Resonance in Medicine 00:00–00 (2015)

Three-layered Radio Frequency Coil Arrangement for Sodium MRI of the Human Brain at 9.4 Tesla

G. Shajan,[1]* Christian Mirkes,[1,2] Kai Buckenmaier,[1] Jens Hoffmann,[1] Rolf Pohmann,[1] and Klaus Scheffler[1,2]

Purpose: A multinuclei imaging setup with the capability to acquire both sodium (^{23}Na) and proton (^{1}H) signals at 9.4 Tesla is presented. The main objective was to optimize coil performance at the ^{23}Na frequency while still having the ability to acquire satisfactory ^{1}H images.

Methods: The setup consisted of a combination of three radio frequency (RF) coils arranged in three layers: the innermost layer was a 27-channel ^{23}Na receive helmet which was surrounded by a four-channel ^{23}Na transceiver array. The outer layer consisted of a four-channel ^{1}H dipole array for B_0 shimming and anatomical localization. Transmit and receive performance of the ^{23}Na arrays was compared to a single-tuned ^{23}Na birdcage resonator.

Results: While the transmit efficiency of the ^{23}Na transceiver array was comparable to the birdcage, the ^{23}Na receive array provided substantial signal-to-noise ratio (SNR) gain near the surface and comparable SNR in the center. The utility of this customized setup was demonstrated by ^{23}Na images of excellent quality.

Conclusion: High SNR, efficient transmit excitation and B_0 shimming capability can be achieved for ^{23}Na MRI at 9.4T using novel coil combination. This RF configuration is easily adaptable to other multinuclei applications at ultra high field ($\geq$ 7T). **Magn Reson Med 000:000–000, 2015. © 2015 Wiley Periodicals, Inc.**

Key words: receive array; 9.4T; dual tuned coils; ^{23}Na MRI

INTRODUCTION

Sodium (^{23}Na) MRI can be used to gain complementary information about cellular viability and metabolism to proton (^{1}H) imaging (1–4). However, the low in vivo concentration and the small gyromagnetic ratio of the ^{23}Na nucleus lead to an inherently low signal-to-noise ratio (SNR). ^{23}Na MRI at ultra high field (UHF, $\geq$ 7 Tesla (T)) is highly beneficial because of the more than linear increase in SNR with respect to the strength of the static magnetic field (B_0) (5–8). This article focuses on the design of a radio frequency (RF) coil setup custom-built for ^{23}Na MRI at 9.4T.

B_0 shimming capability, efficient transmit sensitivity and high SNR are some of the desirable aspects of an RF coil meant for ^{23}Na imaging. Shimming to maximize B_0 homogeneity is an essential requirement at UHF because the inhomogeneity increases with field strength. Enabling ^{1}H and ^{23}Na imaging in an integrated dual-frequency RF coil configuration avoids the need to switch between ^{1}H and ^{23}Na coils to determine the values of adequate shim currents (9,10). Furthermore, shimming at ^{1}H frequency is accomplished in a considerably shorter time compared to shimming at the ^{23}Na frequency (11,12).

B_0 shimming and anatomical localization in dual-frequency applications at clinical field strengths (1.5T and 3T) were accomplished in the past using dual-tuned RF coils which produced identical current distributions at two different frequencies (13,14). However, these dual-tuned coils suffer from a loss in transmit efficiency introduced by the high impedance trap circuits that are part of the design. Moreover, due to the shorter ^{1}H RF wavelength, this type of coil is not well suited to provide whole brain excitation for the ^{1}H frequency at 9.4T. Instead, transmit arrays must be used to provide sufficient spatial coverage for ^{1}H imaging and B_0 mapping (15). Combining a ^{1}H array with a head sized ^{23}Na resonator is difficult because the birdcage rungs can significantly shield the local ^{1}H array surrounding the birdcage.

Another important design consideration is maximizing the SNR at the ^{23}Na frequency. As has been shown previously, phased array coils can be used to accomplish this task (16,17). Experimental SNR comparisons for proton imaging at 3T, which is close to the ^{23}Na frequency (105.7 MHz) at 9.4T, presented by Keil et al (18) demonstrated that increasing the number of coil elements, even up to 64 channels, allows retaining the central SNR while increasing the SNR in the periphery. Only a marginal drop in central SNR was reported (using optimum SNR combination) for a 96-channel head array, while achieving a higher SNR close to the coil elements (19).

It is a challenging task to incorporate all the desired features discussed above into one coil setup. Nevertheless, the principal design criterion remains the optimization of the coil performance at the ^{23}Na frequency while maintaining adequate spatial coverage and sensitivity at the ^{1}H frequency. Nested (20,21) and composite (22) ^{23}Na/^{1}H arrays are some of the coil configurations that have already been used successfully at 3T and 7T. We aimed to meet the various needs of ^{23}Na imaging at 9.4T

[1]High Field MR Center, Max Planck Institute for Biological Cybernetics, Tübingen, Germany.

[2]Department for Biomedical Magnetic Resonance, University of Tübingen, Tübingen, Germany.

*Correspondence to: G. Shajan, M.E., High Field MR Center, Max Planck Institute for Biological Cybernetics, Spemannstr. 41, 72076 Tübingen, Germany.
E-mail: shajan.gunamony@tuebingen.mpg.de

Received 25 September 2014; revised 22 January 2015; accepted 2 February 2015

DOI 10.1002/mrm.25666
Published online 00 Month 2015 in Wiley Online Library (wileyonlinelibrary.com).

by integrating three different RF coil arrays onto a single structure. The outermost layer consisted of a four-element transceiver ^{1}H dipole array providing large longitudinal coverage for anatomical localization and B_0 shimming. In the middle layer, a four-element ^{23}Na loop array that could be operated in transmit-only or transceive mode was inserted. The received signal from the four ^{23}Na loops was combined and routed to a single receiver. The innermost layer consisted of a 27-channel receive array constructed on a tight fitting helmet and making use of the remaining available receive channels of the MR system.

The performance of the three layered coil setup was evaluated by comparing the transmit efficiency and SNR to a single tuned ^{23}Na quadrature birdcage coil. Moreover, the ability to acquire whole brain ^{1}H images at 399.7 MHz in the presence of the ^{23}Na transmit and receive arrays is demonstrated.

METHODS

All measurements were performed on a 9.4T whole-body human MR scanner (Siemens Healthcare, Erlangen, Germany), equipped with a SC72 gradient system having a maximal amplitude of 40 mT/m and a maximum slew rate of 200 T/m/s. A narrowband amplifier with a maximum output of 7.5 kW was used for ^{1}H excitation while a broadband amplifier capable of delivering 4 kW covered the frequency range needed for ^{23}Na MRI (105.7 MHz). Signal reception was enabled by 32 independent broadband receive channels. Bench measurements were performed using a calibrated network analyzer (4396B, Agilent Technologies Inc., CA) together with an 85046A S-parameter test set. The electrical properties of phantom solutions were measured at room temperature using a dielectric probe kit (DAK-12, SPEAG, Zurich, Switzerland).

^{1}H Transceiver Array

The objective of the ^{1}H coil was to provide whole brain excitation in the presence of the ^{23}Na transceiver and receive arrays without having a negative influence on the performance of the ^{23}Na coils. We have shown previously that a combination of a ^{1}H patch antenna and a single tuned ^{23}Na high pass birdcage coil provides whole brain excitation at the ^{1}H frequency without influencing the ^{23}Na coil performance (23). However, the performance of such a patch antenna would be compromised when combined with a multichannel ^{23}Na receive array due to the numerous cables and receive electronics that have to be placed between the antenna and the subject's head.

In this work, dipole elements, which have been proposed as a promising alternative for UHF applications, were used because they are much simpler to construct than phased arrays and offer extended longitudinal coverage (24). A dipole for the ^{1}H frequency at 9.4T is 37.5 cm long in free space. To accommodate the dipole in the head sized coil, the dipoles were shortened to 22 cm by adding tuning inductors (24). Four dipole elements were assembled on 25 mm spacers fixed on to a fiber glass tube (inner diameter: 26 cm, wall thickness: 3 mm, length: 30 cm). The dipole elements were equally spaced around the cylinder with an angular separation of 90°. A shielded cable trap was formed in the coaxial cable that fed the dipoles. For transceive mode operation, the dipole elements were interfaced to the scanner through a separate TR switch on each channel. The TR switches were miniaturized version of the TR switch design presented by Shajan et al (25).

The dipoles were tuned and matched inside the magnet bore to a head and shoulder phantom filled with tissue-equivalent solution ($\varepsilon_r = 58.6$ and $\sigma = 0.64$ S/m) (26). The four-element ^{1}H dipole array formed the outermost layer of the RF coil setup. To compensate for the frequency shift introduced by the ^{23}Na coils in the inner layers and the coil cover that surrounds the dipole array, tuning adjustments on the dipoles were carried out in the magnet bore on the fully assembled coil setup. This tuning step was performed once and was not repeated for individual subjects.

^{23}Na Transceiver Array

One of the main considerations for a ^{23}Na transceiver coil design, in addition to transmit efficiency and uniformity of the RF field, was to adopt a design that has minimal influence on the ^{1}H array. Birdcage coils are the most commonly used volume resonator for spin excitation (27) at low frequencies. Head sized birdcage resonators are typically designed with 12 or 16 rungs. If a birdcage coil was placed inside the ^{1}H dipole array, the performance of the latter would be greatly reduced due to shielding by the rungs of the birdcage. To mitigate this problem, several identical high impedance ^{1}H traps can be added to make the birdcage transparent at the ^{1}H frequency. However, these additional passive components not only reduce transmit efficiency, but would also make coil-tuning an arduous task. Alternatively, the number of rungs can be reduced or the birdcage can be replaced by a loop array to limit the shielding effect on the coil in the outer layer.

In this work, we adopted the loop array approach and constructed a four-channel ^{23}Na transceiver array on the 26 cm fiber-glass tube. Four large loops (15 cm × 18 cm) were symmetrically arranged on the tube, aligning the center of the loops with the dipoles. The copper tracks for the loops were etched on a flexible printed circuit laminate with 35 μm copper on a polyimide film (Krempel GmbH, Vaihingen, Germany). The gap between adjacent loops and hence the width of the individual loops was chosen based on coupling to non-neighboring elements and the inhomogeneity of the transmit field caused by the gaps. A 2D view of the transceiver array is shown in Figure 1. Each loop had a total of 12 capacitors of 39 pF and a variable capacitor in parallel with one of the fixed capacitors for frequency adjustment. The neighboring elements were inductively decoupled. Coupling between the non-neighboring elements was 4.7 dB due to the low frequency and the large size of the transmit elements. Hence, decoupling inductors were implemented in the non-neighboring coils and the inductors were connected using a 180° (cable + pi network) line. A shielded dual-tuned cable trap (105.7 MHz and 399.7

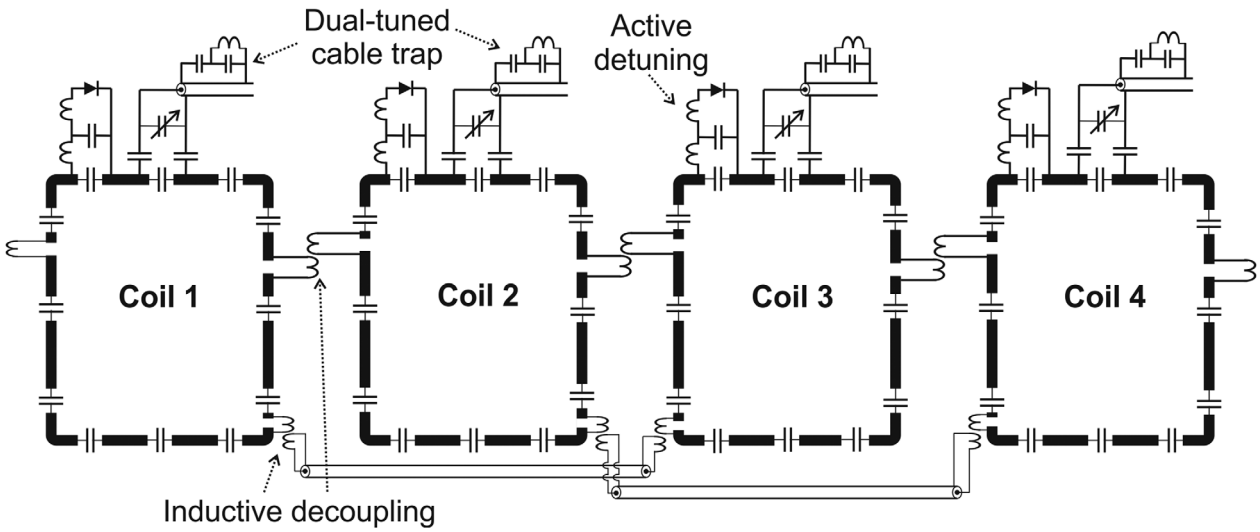

FIG. 1. 2D representation of the ^{23}Na transceiver array: The layout consists of four actively detunable loops of size 18 × 15 cm. The layout is scaled proportionately to show the large gaps between the loops with respect to the loop size.

MHz) was used at the coil input to reduce common mode currents (28). An active detuning circuit was implemented on a 100 Ω 90° T-network as shown in the schematic (Fig. 1) (29,30). An inside view of the implementation showing the ^{1}H dipole array and the ^{23}Na transceiver array is depicted in Figure 2. Coupling between the ^{23}Na loops and the ^{1}H dipoles was less than −43 dB.

To drive the coil in circularly polarized (CP) mode, four outputs of equal amplitude with relative phase offsets of 90° were generated using three quadrature hybrids as shown in the block diagram (Fig. 3a). A picture of the 1 × 4 hybrid splitter is shown in Figure 3b. A separate TR switch on each channel for transceive mode operation would occupy four receive channels and reduce the available number of channels for the receive array. Hence, the signal received from the transceiver array was added in phase before pre-amplification and fed to a single "combined-signal" channel (Fig. 3a). The additional loss in the receive path due to the signal combination before the pre-amplifier stage was approximately −0.5 dB. The subsequent reduction in SNR was of less concern because the receive mode of the transceiver coil was mainly implemented to acquire a reference image for intensity correction (9). The "combined-signal" port of hybrid-4 (Fig. 3a) was terminated to 50 ohms during high power RF transmission and a protection circuit was added in front of the preamplifier to prevent high RF power from damaging it (Fig. 3c). The 1 × 4 hybrid splitter/combiner was realized on a RO4003C laminate (Rogers Corporation, AZ).

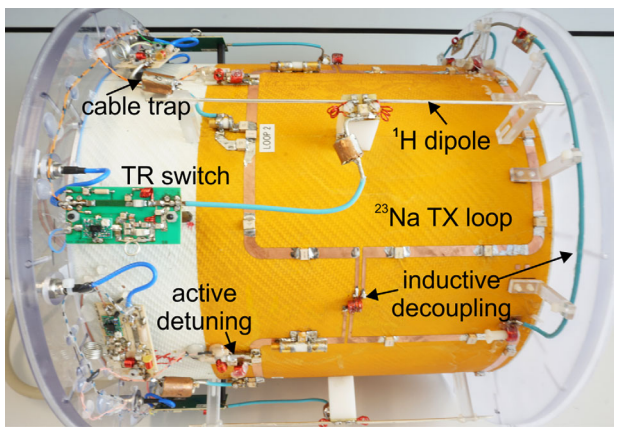

FIG. 2. ^{23}Na transceive loops and ^{1}H dipoles: The dipoles are assembled above the ^{23}Na transceive loops on 25 mm spacers.

^{23}Na Receive Array

An SNR comparison for proton imaging at 3T between two size-matched 64-channel and 32-channel head coils demonstrated that central SNR remains unaffected when

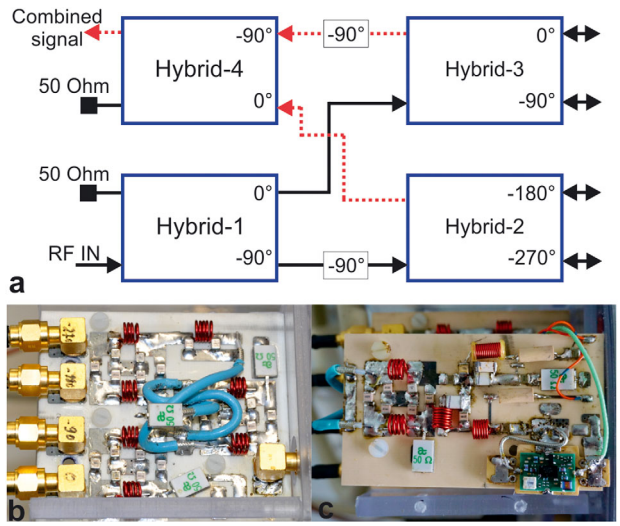

FIG. 3. The 1 × 4 hybrid splitter/combiner. **a**: Functional block diagram shows the combination of quadrature hybrids to generate four outputs with 90° phase offsets. The dotted line represents the received signal path. **b**: Implementation of the hybrid splitter. **c**: Picture of the hybrid combiner and preamplifier protection circuit.

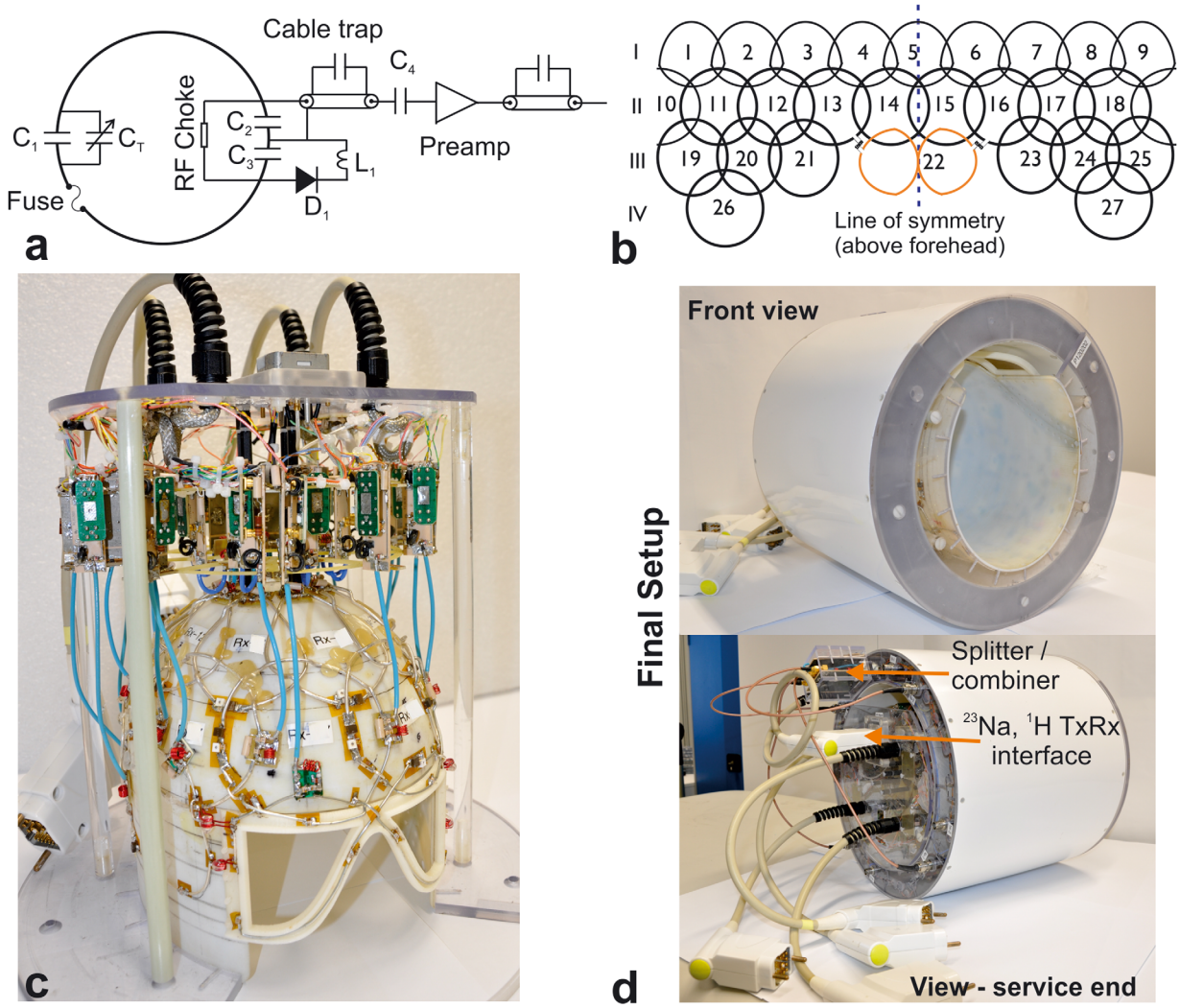

FIG. 4. a: Equivalent circuit of a single receive element. **b**: A 2-dimensional view of the receive coil layout. There are 26 circular loops and one "figure-8" coil (number 22) **c**: A photograph of the constructed receive array. The space inside the "figure-8" was used as eye cut-outs. **d**: Front view and view from the service-end of the fully assembled three layered coil. The service-end view shows the interfacing of the ^{23}Na and ^{1}H transceiver arrays to the scanner through the receive array assembly.

going to a higher number of receive channels even though the penetration depth of the individual loop elements decreases (18). Furthermore, it has been shown that a 32-channel receive array built on a tight fitting helmet can provide significant SNR improvement in the entire brain volume compared with a CP volume coil (17). These results are a motivation to build receive arrays with a higher number of receive elements, provided that sample noise dominance is maintained.

A 27-channel ^{23}Na receive array was constructed on a tight-fitting helmet (left/right: 185 mm, anterior/posterior: 220 mm, head/foot: 200 mm) fabricated using a 3D printer (Eden 250, Objet GmbH, Germany). The equivalent circuit of one receive element is shown in Figure 4a. The loops were constructed using 2 mm diameter silver plated copper wire (APX, Sarrians, France) and tuned to 105.7 MHz using two equally spaced fixed capacitors connected in series. For frequency adjustment, a variable capacitor C_T (2320-2, Johanson Manufacturing Corporation, NJ) was connected in parallel to a fixed capacitor (C_1). The input capacitor was split further in series for impedance matching (C_2) and active detuning (C_3). Capacitor C_4 was used to adjust preamplifier decoupling. A PIN diode (MA4P7470F-1072T, M/A-COM, MA) in series with a hand wound inductor across C_3 completed the active detuning circuit. For secondary safety, in case of malfunction of the detuning circuitry, a protection fuse (Siemens Healthcare) was included.

Using the single receive element as a building block, 26 circular elements and a "figure-8" coil were arranged on the helmet as per the 2D view shown in Figure 4b. The 27 receive elements were arranged in four rows covering 180 mm along the z-direction. In each of the first two rows, nine elements formed two complete rings around the helmet. The 3rd row consisted of six loops and a "figure-8" coil above the eyes. The inner space in the "figure-8" coil acted as eye cut-outs (Fig. 4c). The "figure-8" coil was critically overlapped with two coils of the 2nd row (coils 14 and 15 in Figure 4b) and inductively decoupled with two more coils (coils 13 and 16 in

Figure 4b). There were two loops in the 4th row. The neighboring coils were critically overlapped as per the 2D scheme in Figure 4b to cancel mutual inductance (16). Coil tuning, impedance matching and adjacent element overlap were adjusted by loading the receive helmet with the head and shoulder phantom. While adjusting the impedance or the critical overlap between adjacent coils, all other elements were detuned. A pair of decoupled flux probes was used for measuring preamplifier decoupling, quality factor (Q) and active detuning.

The receive elements were connected to low input impedance preamplifiers (WanTcom Inc., MN). A pair of PIN diodes (MPP4203, Microsemi, MN) was added across the input of the high electron mobility transistor (HEMT) for high voltage protection. A cable trap was installed at the input as well as the output of the preamplifier. The control signal to actively detune the receive loops was fed through the RF cable using a bias-tee. The circuit boards with the receive electronics were mounted on a holder placed on top of the helmet, clearing the field of view (FOV) of the transceiver coil (Fig. 4c). This resulted in longer cables between the preamplifier and the input match capacitor for lower row elements. While additional cable length does not affect the impedance match, it shifts the preamplifier decoupling to lower frequencies. Reducing the value of capacitor C_4 compensated for this frequency shift. Furthermore, the long cables, especially the ones from the lower row elements to the preamplifiers were carefully routed away from the edges of the ^{23}Na transmit loops to minimize the interaction between the two ^{23}Na arrays.

Scanner Interface

Four of the 32 available receive channels were dedicated for ^{1}H imaging and the two ^{23}Na coils used the remaining 28 channels. In the standard configuration, the three arrays were assembled together and the coil was operated as a 32-channel coil. Alternatively, the ^{1}H dipole array could be plugged to the scanner together with the ^{23}Na transceiver array after demounting the ^{23}Na receive array. This modular feature was essential to quantify the influence of the receive array on the transmit efficiency of the ^{23}Na and ^{1}H transceive arrays. A photograph of the complete coil assembly is shown in Figure 4d.

Comparison Study

To validate the transmit and receive performance of the multinuclei imaging setup a conventional single tuned ^{23}Na birdcage coil was used as reference. The length and diameter of the 16-rung high pass birdcage coil were 21 cm and 25 cm, respectively. The birdcage coil was driven in quadrature using a home-built quadrature hybrid. The receive port of the quadrature hybrid was terminated to 50 ohms. Reception of the induced signal was accomplished by means of two TR switches installed between the outputs of the quadrature hybrid and the two feed points of the coil (31).

A head-only phantom filled with 2% w/w agar and 75 mM NaH_2PO_4 was built for the ^{23}Na SNR and transmit efficiency comparison study. The measured electrical properties were: permittivity (ε_r) = 80 and conductivity (σ) = 0.60 S/m. The same phantom was also constructed in the numerical domain.

Coil Simulation

Detailed models of the ^{23}Na transceiver array together with the ^{1}H dipole array and also of the reference birdcage coil was created and numerical simulations were performed using CST Studio Suite 2012 (CST, Darmstadt, Germany). The workflow presented in (32) was adopted for the numerical computation. The transmit coils were tuned in the RF circuit domain and the electromagnetic field distribution together with specific absorption rate (SAR) maps were calculated in the 3D EM domain. Peak averaged SAR over 10 g of tissue (SAR_{10g}) and safety excitation efficiency (SEE) ($B_1{}^{+}{}_{avg}/\sqrt{SAR_{10g}}$) were calculated for the two setups using the virtual family's "Duke" model (33). For in vivo measurements, the transmit power was limited based on the estimated SAR_{10g} with an additional safety margin of 100%. Due to the geometrical complexity of the receive array and limitations in the 3D EM meshing, the receive array model was not incorporated in the numerical domain.

Transmit Field Characterization

The transmit field ($B_1{}^{+}$) of the ^{1}H dipoles was mapped using the actual flip angle imaging (AFI) technique (34) (FOV: 240 × 240 × 240 mm^3, matrix: 64 × 64 × 80, repetition times TR_1/TR_2: 12/100 ms, echo time (TE): 4 ms, bandwidth: 500 Hz/pixel, acquisition time: 7 min). $B_1{}^{+}$ mapping for ^{23}Na was performed with a phase sensitive mapping sequence (35). The sampling scheme was a stack of spirals with a nominal resolution of 3 × 3 × 3 mm^3. The k-space trajectories were calculated on the scanner by a time-optimal gradient design algorithm (36). The FOV was 250 mm and the acquisition time (TA) was 8 min. The field maps (simulated and measured) were normalized to the root-mean-square voltage measured by the scanner's RF supervision module. To assess the perturbation caused by the presence of the receive array, $B_1{}^{+}$ maps were acquired with and without the receive array in the transmit FOV. Because the tuning and matching condition of the ^{1}H and ^{23}Na transceiver arrays change when the ^{23}Na receive helmet is inserted or removed, the impedance match of the ^{1}H/^{23}Na transceive elements had to be adjusted for the two scan conditions. In both cases a match of better than −20 dB was achieved.

SNR Comparison

A pseudo multiple replica approach was used to estimate the achieved SNR (37). Noise data was acquired from each coil element without RF excitation and the standard deviation and correlation of the noise were determined. Based on these parameters synthetic correlated noise was generated and added to the k-space of a standard image acquisition, which consisted of a stack-of-spirals with the following imaging parameters: TE = 0.4 ms, TR = 50 ms, dwell time 5.5 μs, readout time 8 ms, 13 averages, 15 spiral interleaves per partition, 64

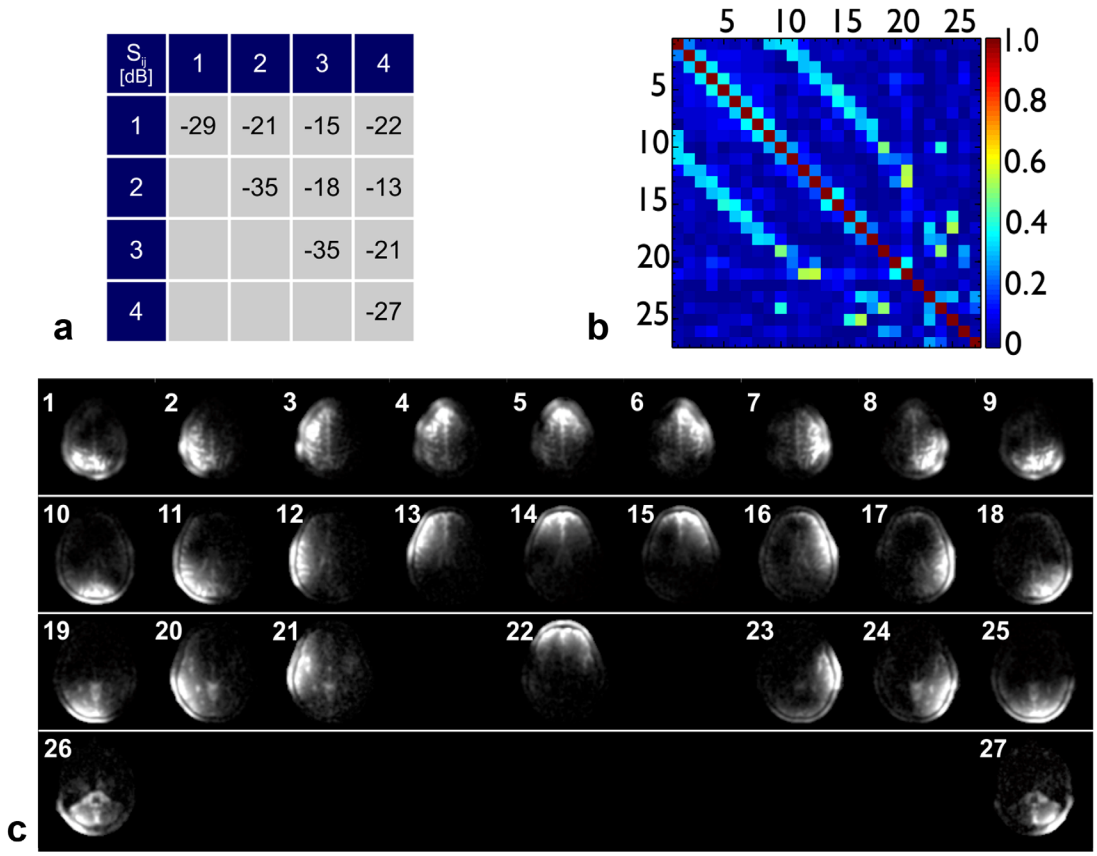

FIG. 5. a: S-parameter matrix of the four-channel ^{23}Na transceiver array measured in the presence of the actively detuned receive array. **b**: Noise correlation matrix of the ^{23}Na receive array. Average of all the off-diagonal values are 0.093 with maximum value of 0.54. **c**: Individual channel images acquired when all elements are active. The axial slices displayed pass through the middle of each row of coils on the receive helmet. The number on each image corresponds to the coil number displayed in Figure 4b.

partitions, resolution = 4 × 4 × 4 mm^3, FOV = 240 × 240 × 256 mm^3, nominal flip angle 40°, TA = 10 min. Once the image was reconstructed, the process was repeated with a new set of synthetic noise. The standard deviation for each voxel through a stack of 500 replicas was calculated and used to generate SNR maps. Additionally, B_1^+ maps were acquired to correct for signal variations caused by deviations from the nominal flip angle. SNR differences due to signal saturation were neglected.

Imaging

Images acquired with phased arrays are degraded by the inhomogeneous sensitivity profile of the array elements. This modulation can be removed using the sensitivity encoding (SENSE) reconstruction formalism. The required coil sensitivity maps can be either obtained through self-calibration or preferentially deduced from a more homogenous reference image (9). In this study, the ^{23}Na coil sensitivity maps were calculated by dividing a low resolution image acquired with the receive array by a reference image from the transceiver array. The acquisition parameters for both images were identical: TE = 0.4 ms, TR = 45 ms, dwell time 3.6 μs, readout time 5 ms, 2 averages, 15 spiral interleaves per partition, 44 partitions, resolution = 4 × 4 × 5 mm^3, TA = 1 min. Smoothness of the sensitivity maps was enforced by locally fitting a low degree polynomial.

For ^{23}Na in vivo measurements, we scanned two healthy male volunteers (average age: 32 years) who had signed a written consent form approved by the institutional review board of the University of Tübingen. A 3D balanced steady state free precession (bSSFP) sequence with spiral readout was used to image the subject's brain. The sequence parameters were chosen as follows: TE = 2 ms, TR = 11 ms, dwell time 3 μs, readout time 3 ms, 10 averages, 100 spiral interleaves per partition, 56 partitions, FA = 40°, Res = 2 × 2 × 4 mm^3, FOV = 240 × 240 × 224 mm^3 and TA = 10 min. The images were reconstructed on a standard PC using Matlab (The Mathworks, Natick, MA) by first performing Kaiser-Bessel gridding for each partition (38). Then, a 3D Hanning window was applied to the resampled signal to suppress high-frequency noise components. Finally, the filtered images were obtained by applying a 3D Fast Fourier transformation to the k-space.

To assess image quality achieved by the ^{1}H dipole array, gradient echo images were acquired with the following scan parameters: TE = 5 ms, TR = 1 s, 1.1 mm in-plane resolution, slice thickness = 2 mm, FOV = 220 × 220 mm^2, 30 slices and acquisition time of 3 min in each orientation.

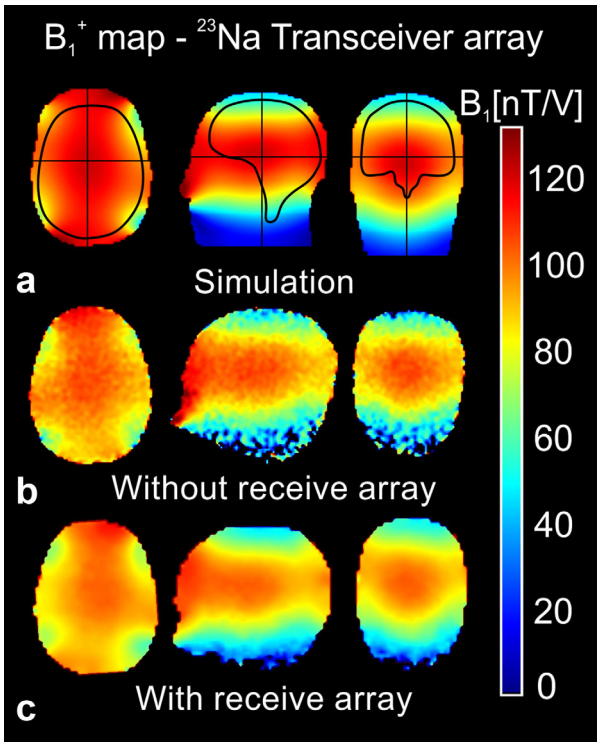

FIG. 6. ^{23}Na B_1^+ maps. **a**: Central axial, sagittal and coronal slices of the simulated field maps. A brain mask is superimposed to estimate the transmit efficiency. **b**: Measured field maps in the transceiver mode acquired without the receive array. In the superimposed volume, the measured mean B_1^+ is 13% weaker than in simulation. **c**: Field maps acquired in the presence of the 27-channel receive array. Measured B_1^+ in the center of the coil reduced from 105 nT/V to 100 nT/V with the receive array in the transmit FOV.

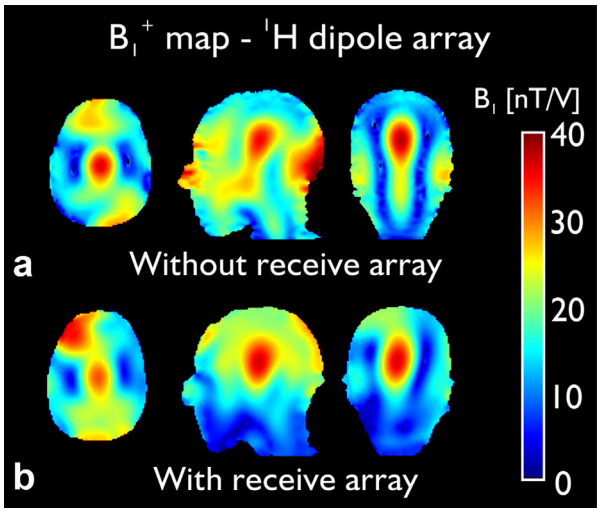

FIG. 7. ^{1}H B_1^+ maps. **a**: Measured B_1^+ map of the ^{1}H dipole array measured in presence of the actively detuned ^{23}Na transceive array, but without the 27-channel receive array. The B_1^+ profile is symmetric and the longitudinal coverage is sufficient to excite the whole brain. **b**: Addition of the ^{23}Na receive array leads to an altered B_1^+ distribution.

RESULTS

^{23}Na Transceiver Array

The unloaded Q (Q_{UL}) of a single ^{23}Na transceive loop with 12 series capacitors and the decoupling inductors was 248. Loaded Q (Q_L), measured by loading the transmit element with the head and shoulder phantom, was 147. Active detuning was −36 dB with 50 mA of DC. The S-parameter matrix of the four-element ^{23}Na transceiver array is shown in Figure 5a. Inductive decoupling circuits between the nonadjacent coils improved the isolation from −4.7 dB to at least −12 dB.

The phase error in the 1 × 4 hybrid splitter, designed to drive the array in CP mode, was within ± 1.5° and the insertion loss was 0.3 dB at 105.7 MHz. In transmit mode, the preamplifier protection circuit in the combined-signal port (Fig. 3a) provided better than 40 dB isolation.

Receive Array

Q_{UL}, measured on a 90 mm diameter representative circular loop constructed with components as shown in Figure 4a, was 224. For Q measurements, the coaxial cable attached to the coil input was removed. Q_L was 48 when the coil was loaded with the head and shoulder phantom placed at 8 mm from the coil. An impedance match of at least −15 dB was achieved on each coil element and active detuning was better than 35 dB. The isolation, measured in loaded condition, between adjacent overlapping coils was between −9 and −12 dB. The low input impedance preamplifiers provided an additional 15 to 18 dB decoupling. A single capacitor placed in parallel across the input for matching (Fig. 4a) resulted in a large capacitor value ($C_2 = 120$ pF) and a subsequent lower preamplifier decoupling. The noise correlation matrix of the receive array is shown in Figure 5b. The average of all the off-diagonal values was 0.093 and the maximum value in the matrix was 0.54. Uncombined bSSFP in vivo images, acquired with all receive elements active, are shown in Figure 5c to demonstrate the isolation between coil elements. The number on the individual images corresponds to the coil element numbering displayed in Figure 4b. Because the coil elements are arranged in multiple rows on the helmet, an axial slice through the middle of each row is shown.

Transmit Field Characterization

Figure 6a shows the simulated field maps for the ^{23}Na transceiver array in the head-only phantom. The crosshairs in the individual maps represent the displayed slices through the center of the coil in each scan plane. A brain mask was superimposed on the 3D B_1^+ map and the transmit efficiency was estimated in this volume. The numerical model predicted a mean transmit efficiency of 92 nT/V inside the brain mask. The actual field strength (Fig. 6b), measured without the receive array present, was approximately 13% weaker (80 nT/V) than predicted by the simulations. Except for this scaling factor, the simulated and measured B_1^+ field distributions match well. When the ^{23}Na receive array was added (Fig. 6c), the B_1^+ distribution remained nearly unaffected. In the center of the coil, the peak value was 105 nT/V in

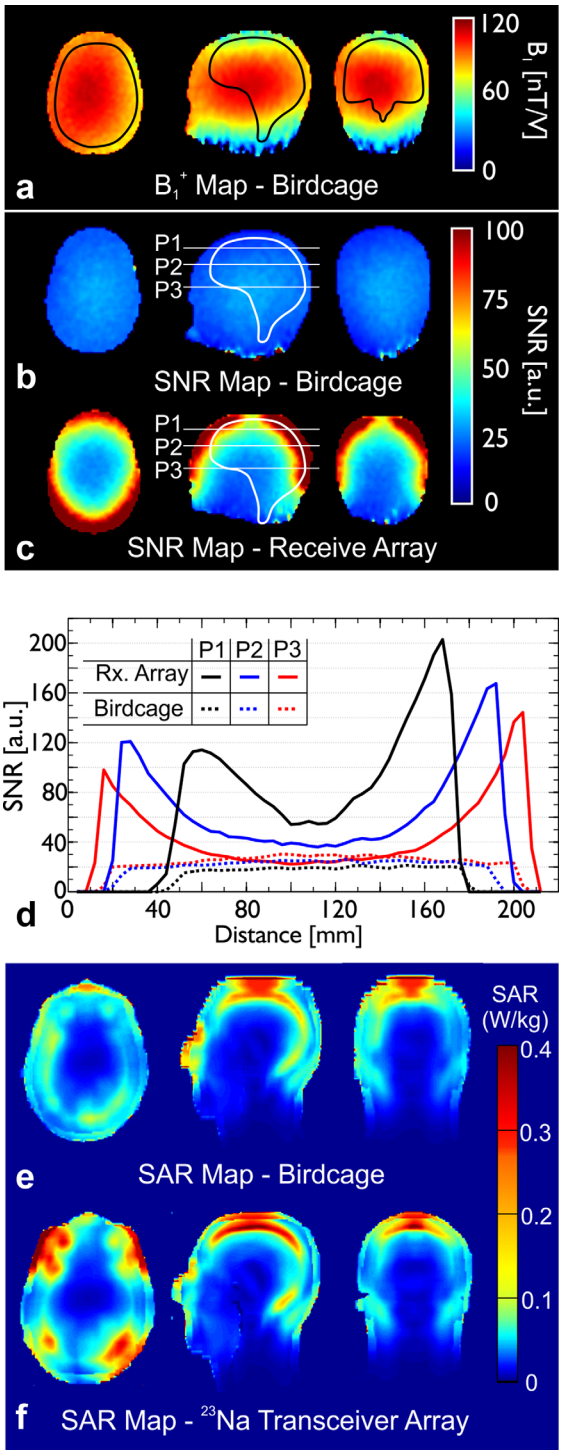

FIG. 8. **a**: Measured B_1^+ maps of the ^{23}Na birdcage coil. ^{23}Na transmit efficiency of the three layered coil is 17% weaker than the birdcage in the superimposed brain volume. For direct comparison to Figure 6, the same color map is used. **b**: SNR map of the ^{23}Na birdcage coil. **c**: SNR maps for the 27-channel receive array acquired with the same phantom. **d**: SNR profiles passing approximately through the middle of the top three rows of the receive array. In P1and P2, the central SNR gain is a factor of 2.75 and 1.48, respectively. In P3, the maximum SNR for the birdcage is 28 and the minimum SNR for the array is 23. **e**: Estimated SAR_{10g} map for the birdcage in the "Duke" model. Maximum value: 0.34 W/kg. **f**: Estimated SAR_{10g} for ^{23}Na transceive array. Maximum value: 0.6 W/kg.

the transceive mode and 100 nT/V when the receive array was in place. In the brain mask the mean transmit efficiency was 80 nT/V demonstrating minimal loss due to the addition of the receive array. Note that the B_1^+ maps shown in the Figure 6c were acquired with the 27-channel receive array and hence exhibit higher SNR.

Figure 7a shows the B_1^+ distribution of the ^{1}H dipole array in the head and shoulder phantom. The AFI maps acquired in the presence of ^{23}Na transceiver array demonstrate sufficient longitudinal coverage and exhibited symmetric distribution as shown in the axial and coronal orientations. However, when the ^{23}Na receive array was inserted, the distribution was altered due to the low impedance ^{23}Na receive array elements and cables inside the transmit FOV (Fig. 7b). Altering the individual cable routing to minimize the influence on the ^{1}H transmit field is not only a laborious task, but can also compromise the performance of the ^{23}Na transceiver coil. Nevertheless, the image quality and coverage offered by the dipole array was sufficient for the intended purpose.

Comparison to Birdcage Coil

Figure 8a shows the B_1^+ map acquired with the reference birdcage coil using the head-only phantom. In the volume inside the brain mask, transmit efficiency of the three-layered coil is 17% weaker than the birdcage. Note that the birdcage is slightly smaller in diameter (25 cm versus 26 cm) and does not have loss contributions from the active detuning circuitry or from the presence of the ^{23}Na receive array in the transmit FOV.

The SNR maps shown in Figure 8b and 8c demonstrate the superior receive performance of the 27-channel ^{23}Na receive array compared with the single-tuned birdcage coil. The SNR gain was quantified using SNR profiles passing through the middle of each of the top three rows of the receive array (Fig. 8d). Profile P1, through the middle of the top row covering the dome of the helmet, revealed a 2.8-fold SNR improvement in the center of the slice. The SNR gain in profile P2, through the middle of the second row, was 1.5-fold in the center of the slice and significantly higher close to the surface coils. Along profile P3, the peak central SNR for the birdcage was 28. The minimum SNR for the receive array along profile P3 was 23 and the maximum SNR in the periphery was more than five times higher than the SNR achieved by the birdcage.

The estimated SAR_{10g} maps for the Duke model are shown in Figures 8e and 8f. Note that the maximum electric field is along the end-ring for the birdcage and along the edges of the loops for the ^{23}Na transceiver array. The peak SAR_{10g} and SEE (in the whole head of Duke model) for the birdcage and the ^{23}Na transceiver array were 0.34 W/kg; 1.46 $\mu T/\sqrt{(W/kg)}$ and 0.6 W/kg; 1.21 $\mu T/\sqrt{(W/kg)}$, respectively.

In Vivo Results

In vivo ^{23}Na images acquired using this coil configuration are shown in Figure 9. The homogeneous reference image from the ^{23}Na transceiver array and the corresponding slice acquired with identical parameters using the ^{23}Na receive array are shown in Figures 9a and 9b,

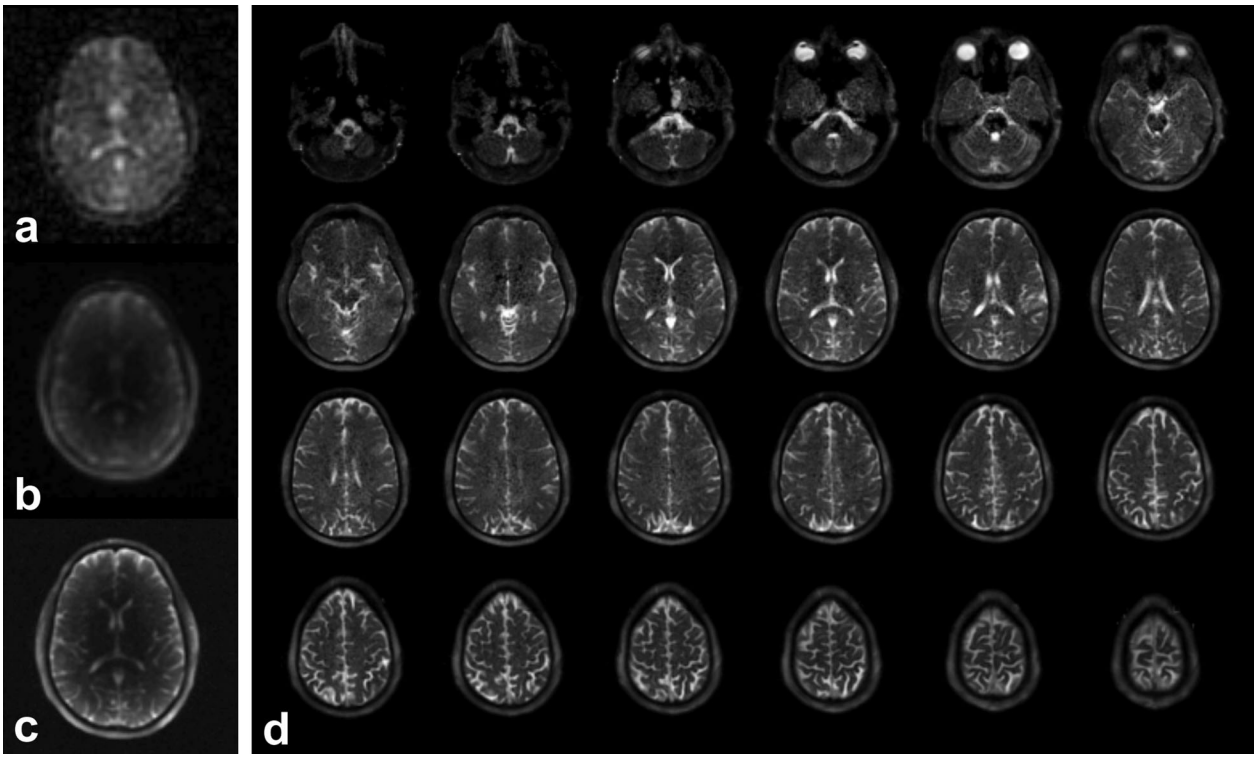

FIG. 9. In vivo ^{23}Na images. **a**: Reference image acquired with the four-channel ^{23}Na transceiver array. **b**: The same image as in (a), but acquired with the 27-channel receive array. **c**: bSSFP acquisition without intensity correction. (d) Sensitivity corrected bSSFP images. Scan parameters: TE = 2 ms, TR = 11 ms, FA = 40°, Resolution = 2 × 2 × 4 mm^3 and acquisition time = 10 min.

respectively. Even though the SNR of the reference images was moderate, they still provided sufficient information to calculate coil sensitivity maps. A single slice, without intensity correction, from the bSSFP acquisition using the receive array and reconstructed using root sum-of-squares is shown in Figure 9c. As expected, the signal intensity is higher close to the surface coils and weaker in the center.

Figure 9d shows multiple slices of the sensitivity corrected bSSFP image acquired in 10 min with a resolution of 2 × 2 × 4 mm^3. The intensity variation due to the coil sensitivity profile could be eliminated. Excellent spatial resolution with good SNR could be achieved, especially in the cortical brain. In the center of the brain, the reduced sensitivity of the 27-channel array and the SENSE reconstruction led to moderate but still acceptable noise enhancement.

In vivo ^{1}H images acquired with the dipole array in the presence of the two ^{23}Na arrays is shown in Figure 10. The asymmetry introduced by the ^{23}Na receive array

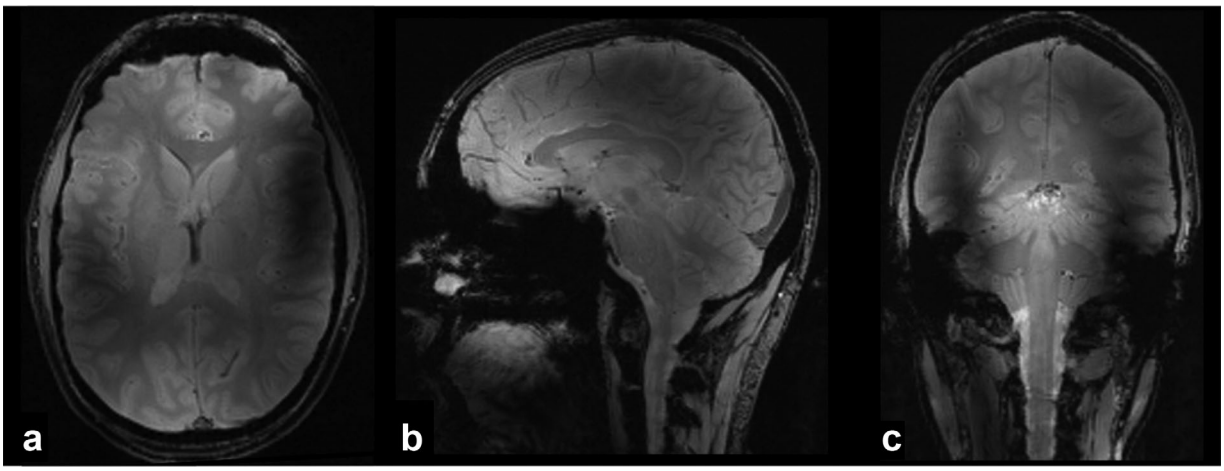

FIG. 10. **a–c**: In vivo gradient echo images acquired with the four-channel ^{1}H dipole array in the presence of the ^{23}Na transmit and receive arrays. In-plane resolution: 1.1 mm, slice thickness: 2 mm acquisition time: 3 min for each orientation.

as noticed in Figure 7b can be seen on the axial slice shown in Figure 10a. The ^{1}H dipoles provided whole brain coverage at 399.7 MHz as shown in the sagittal (Fig. 10b) and coronal slices (Fig. 10c). These results demonstrate the utility of the ^{1}H dipole array for the intended purpose of fast B_0 mapping and anatomical localization in the presence of the ^{23}Na transmit and receive arrays.

DISCUSSION AND CONCLUSION

The coil arrangement presented in the current work was conceived to fulfill design criteria such as maximizing coil performance at ^{23}Na frequency, acquire a homogeneous ^{23}Na reference image for intensity correction and ensuring whole brain coverage at the ^{1}H frequency for B_0 shimming and anatomical localization. Several alternatives were investigated to meet these requirements. Initial experiments using a combination of a 16-rung ^{23}Na birdcage coil and a four-element ^{1}H dipole array resulted in an almost total loss of the ^{1}H signal in the center of the birdcage due to the shielding effect of the rungs.

Ultimate SNR in center of a sphere was achieved with four coils evenly surrounding the volume (at 64 MHz) (39). More coils were required to reach the ultimate SNR in the center of the sphere at higher frequencies. Furthermore, the peripheral SNR approaches the ultimate achievable SNR with higher number of coils (39). As demonstrated in the SNR maps (Fig. 8d), significant gain in ^{23}Na SNR was achieved in almost the entire brain volume. In the center of the 27-channel receive array, the SNR was only marginally lower than the peak SNR of the birdcage. The coil elements in the receive array were arranged on the helmet surface to follow the contours of the brain anatomy, resulting in just two elements in the fourth row. Although it is impractical to build receive arrays covering spherical volumes, more coil elements covering the helmet surface in the fourth row, either by adding more receive channels or by rearranging the 27 coil elements should boost the central SNR.

The performance of the three-layered coil was validated and the experimental results show that the proof-of-concept coil meets the various demands of a multinuclei imaging setup. Transmit and receive performance of the coil at the ^{23}Na frequency was not compromised. The in vivo ^{23}Na images, acquired in only ten minutes, show level of detail not previously achieved. The challenging task of whole brain coverage for ^{1}H images, despite the high frequency and the presence of the ^{23}Na arrays, could be accomplished. Last but not least, this combination of three coil arrays can be readily adapted for other nuclei at 9.4T or for multinuclei applications at UHF.

ACKNOWLEDGMENT

The authors most gratefully acknowledge the contribution of Dr. Nikolai Avdievich in building the dual tuned cable trap and the inductive decoupling between non-neighboring coils. This work was funded in part by the Helmholtz Alliance ICEMED – Imaging and Curing Environmental Metabolic Diseases, through the Initiative and Networking Fund of the Helmholtz Association.

REFERENCES

1. Ouwerkerk R, Bleich KB, Gillen JS, Pomper MG, Bottomley PA. Tissue sodium concentration in human brain tumors as measured with ^{23}Na MR imaging. Radiology 2003;227:529–537.
2. Thulborn KR, Davis D, Adams H, Gindin T, Zhou J. Quantitative tissue sodium concentration mapping of the growth of focal cerebral tumors with sodium magnetic resonance magnetic resonance imaging. Magn Reson Med 1999;41:351–359.
3. Pilkinton DT, Clark CM, Elliott MA, Witschey WR, Borthakur A, Reddy R. Sodium MR imaging detection of mild Alzheimer disease: preliminary study. J Neuroradiol 2009;30:978–984.
4. Thulborn KR, Gindin T, Davis D, Erb P. Comprehensive MR imaging protocol for stroke management: tissue sodium concentration as a measure of tissue viability in nonhuman primate studies and in human studies. Radiology 1999;213:156–166.
5. Keltner JR, Carlson W, Roos MS, Wong TS, Wong TL, Budinger TF. Electromagnetic fields of surface coil in vivo NMR at high frequencies. Magn Reson Med 1991;22:467–480.
6. Wiesinger F, Boesiger P, Pruesmann KP. Electrodynamics and ultimate SNR in parallel MR imaging. Magn Reson Med 2004;52:376–390.
7. Vaughan JT, Garwood M, Collins CM, et al. 7T vs. 4T: RF power, homogeneity and signal-to-noise comparison in head images. Magn Reson Med 2001;46:24–30.
8. Pohmann R, Scheffler K. Brain imaging with 7T vs. 9.4T: a direct comparison of MR parameters and SNR. In Proceedings of the 22nd Annual Meeting of ISMRM, Milan, Italy, 2014. Abstract 1421.
9. Qian Y, Zhao T, Wiggins GC, Wald LL, Zheng H, Weimer J, Boada FE. Sodium imaging of the human brain at 7T with 15-channel array coil. Magn Reson Med 2012;68:1808–1814.
10. Lu A, Atkinson IC, Claiborne TC, Damen FC, Thulborn KR. Quantitative sodium imaging with a flexible twisted projection pulse sequence. Magn Reson Med 2010;63:1583–1593.
11. Atkinson IC, Lu A, Thulborn KR. Preserving the accuracy and resolution of the sodium bioscale from quantitative sodium MRI during intrasubject alignment across longitudinal studies. Magn Reson Med 2012;68:751–761.
12. Romanzetti S, Mirkes CC, Fiege DP, Celik A, Felder J, Shah NJ. Mapping tissue sodium concentration in the human brain: a comparison of MR sequences at 9.4 Tesla. Neuroimage 2014;96:44–53.
13. Shen GX, Wu JF, Boada FE, Thulborn KR. Experimentally verified, theoretical design of dual-tuned, low-pass birdcage radiofrequency resonators for magnetic resonance imaging and magnetic resonance spectroscopy of human brain at 3.0 Tesla. Magn Reson Med 1999;41:268–275.
14. Shen GX, Boada FE, Thulborn KR. Dual-frequency, dual-quadrature, birdcage design with identical B1 pattern for sodium imaging of the human brain at 1.5 T. Magn Reson Med 1997;38:717–725.
15. Van de Moortele PF, Akgun C, Adriany G, Moeller S, Ritter J, Collins CM, Smith MB, Vaughan JT, Ugurbil K. B1 destructive interferences and spatial phase patterns at 7T with a head transceiver array coil. Magn Reson Med 2005;54:1503–1518.
16. Roemer PB, Edelstein WA, Hayes CE, Souza SP, Mueller OM. The NMR phased array. Magn Reson Med 1990;16:192–225.
17. Wiggins GC, Triantafyllou C, Potthast A, Reykowski A, Nittka M, Wald LL. 32-channel 3 Tesla receive-only phased array head coil with soccer-ball element geometry. Magn Reson Med 2006;56:216–223.
18. Keil B, Blau JN, Biber S, Hoecht P, Tountcheva V, Setsompop K, Triantafyllou C, Wald LL. A 64-channel 3T array coil for accelerated brain MRI. Magn Reson Med 2013;70:248–258.
19. Wiggins GC, Polimeni JR, Potthast A, Schmitt M, Alagappan V, Wald LL. 96-channel receive-only head coil for 3 Tesla: design, optimization and evaluation. Magn Reson Med 2009;62:754–762.
20. Wiggins GC, Brown R, Fleysher L, Zhang B, Stoeckel B, Inglese M, Sodickson DK. A nested dual frequency birdcage/stripline coil for sodium/proton brain imaging at 7T. In Proceedings of the 18th Annual Meeting of ISMRM, Stockholm, Sweden, 2010. Abstract 1500.
21. Brown R, Madelin G, Lattanzi R, Chang G, Regatte RR, Sodickson DK, Wiggins GC. Design of a nested eight-channel sodium and four-channel proton coil for 7T knee imaging. Magn Reson Med 2013;70:259–268.
22. Kaggie JD, Hadley R, Badal J, Campbell JR, Park DJ, Parker DL, Morell G, Newbould RD, Wood AF, Bangerter NK. A 3T sodium

and proton composite array breast coil. Magn Reson Med 2014;71: 2231–2242.
23. Mirkes CC, Hoffmann J, Shajan G, Pohmann R, Scheffler K. High resolution quantitative sodium imaging at 9.4 Tesla. Magn Reson Med 2015;73:342–351.
24. Wiggins GC, Zhang B, Lattanzi R, Chen G, Sodickson D. The electric dipole arrray: an attempt to match the ideal current pattern for central SNR at 7 Tesla. In Proceedings of the 2oth Annual Meeting of ISMRM, Melbourne, Australia, 2012. Abstract 541.
25. Shajan G, Hoffmann J, Budde J, Adriany G, Ugurbil K, Pohmann R. Design and evaluation of an RF front-end for 9.4T human MRI. Magn Reson Med 2011;66:596–604.
26. Beck BL, Jenkins KA, Rocca JR, Fitzsimmons JR. Tissue-equivalent phantoms for high frequencies. Concepts Magn Reson Part B 2004;20: 30–33.
27. Hayes CE, Edelstein WA, Schenk JF, Mueller OM, Eash M. An efficient, highly homogeneous radiofrequency coil for whole-body NMR imaging at 1.5T. J Magn Reson 1985;63:622–628.
28. Avdievich NI. Transceiver-phased arrays for human brain studies at 7T. Appl Magn Reson 2011;41:483–506.
29. Nabetani A, Watkins RD. Dynamic disabling switch development for 7T self-shielded birdcage coil. In Proceedings of the 12th Annual Meeting of ISMRM, Kyoto, Japan, 2004. Abstract 1574.
30. Avdievich NI, Bradshaw K, Kuznetzov AM, Hetherington HP. High-field actively detunable transverse electromagnetic (TEM) Coil with low bias voltage for high power RF transmission. In Proceedings of the 22nd Annual Meeting of ISMRM, Berlin, Germany, 2007. Abstract 238.
31. Sorgenfrei BL, Edelstein WA. Optimizing MRI signal-to-noise ratio for quadrature unmatched RF coils: two preamplifiers are better than one. Magn Reson Med 1996;36:104–110.
32. Hoffmann J, Shajan G, Scheffler K, Pohmann R. Numerical and experimental evaluation of RF shimming in the human brain at 9.4T using a dual-row transmit array. Magn Reson Mater Phys 2014;27:373–386.
33. Christ A, Kainz W, Hahn EG, et al. The virtual family–development of surfacebased anatomical models of two adults and two children for dosimetric simulations. Phys Med Biol 2010;55:N23–N38.
34. Yarnykh VL. Actual flip-angle imaging in the pulsed steady state: a method for rapid three-dimensional mapping of the transmitted radiofrequency field. Magn Reson Med 2007;57:192–200.
35. Allen SP, Morrell GR, Peterson B, Park D, Gold GE, Kaggie JD, Bangerter NK. Phase-sensitive sodium B_1 mapping. Magn Reson Med 2011;65:1126–1131.
36. Lustig M, Kim SJ, Pauly JM. A fast method for designing time-optimal gradient waveforms for arbitrary k-space trajectories. IEEE Trans Med Imaging 2008;27:866–873.
37. Robson PM, Grant AK, Madhuranthakam AJ, Lattanzi R, Sodickson DK, McKenzie CA. Comprehensive quantification of signal-to-noise ratio and g-factor for image-based and k-space-based parallel imaging reconstructions. Magn Reson Med 2008;60:895–907.
38. Jackson JI, Meyer CH, Nishimura DG, Macovski A. Selection of a convolution function for Fourier inversion using gridding. IEEE Trans Med Imaging 1991;10:473–478.
39. Wiesinger F, De Zanche N, Pruessmann KP. Approaching ultimate SNR with finite coil arrays. In Proceedings of the 22nd Annual Meeting of ISMRM, Miami Beach, Florida, USA, 2005. Abstract 672.

PUBLICATION 3

FULL PAPER

Magnetic Resonance in Medicine 00:00–00 (2015)

Triple-Quantum-Filtered Sodium Imaging at 9.4 Tesla

Christian Mirkes,[1,2]* G. Shajan,[2] Jonas Bause,[2,3] Kai Buckenmaier,[2] Jens Hoffmann,[2,3] and Klaus Scheffler[1,2]

Purpose: Efficient acquisition of triple-quantum-filtered (TQF) sodium images at ultra-high field (UHF) strength.

Methods: A three-pulse preparation and a stack of double-spirals were used for the acquisition of TQF images at 9.4 Tesla. The flip angles of the TQ preparation were smoothly reduced toward the edge of k-space along the partition-encoding direction. In doing so, the specific absorption rate could be reduced while preserving the maximal signal intensity for the partitions most relevant for image contrast in the center of k-space. Simulations, phantom and in vivo measurements were used to demonstrate the usefulness of the proposed method.

Results: A higher sensitivity (~20%) was achieved compared to the standard acquisition without flip angle apodization. Signals from free sodium ions were successfully suppressed irrespective of the amount of apodization used. B_0 corrected TQF images with a nominal resolution of $5 \times 5 \times 5$ mm^3 and an acceptable signal-to-noise ratio could be acquired in vivo within 21 min.

Conclusion: Conventional TQF in combination with flip angle apodization permits to exploit more efficiently the increased sensitivity available at 9.4T. **Magn Reson Med 000:000–000, 2015. © 2015 Wiley Periodicals, Inc.**

Key words: Sodium MRI; ultra-high field; triple-quantum filtering

INTRODUCTION

The interesting physical properties of the sodium (^{23}Na) nucleus and the additional information which can be gained from it have always provided an incentive to further develop the existing imaging techniques. The availability of ultra-high field (UHF) scanners and the concomitant increase in signal-to-noise ratio (SNR) allowed reducing the scanning times and thus increased the applicability of sodium MRI (sMRI). Nevertheless, sMRI remains challenging due to the low in vivo concentrations (human brain tissue: 30–35 mM) (1) and the short transverse relaxation times (human brain tissue: fast component: $T_{2f} = 2$–5 ms, slow component $T_{2s} = 15$–25 ms) (2). Unlike protons, the sodium nucleus possesses an electric quadrupole moment which makes it sensitive to electric field gradients in its molecular environment. Thus, free and motion restricted sodium ions exhibit a different physical behavior in the human body (3). Differentiation between extra- and intracellular sodium can provide useful information in case of many pathologies such as tumors, ischemia or articular cartilage degeneration (4–6).

Shift reagents allow to efficiently discriminate signals from intra- and extracellular sodium (7–9). However, their use is limited to animal studies either due to their toxicity or the lack of a clinical approval for their application in humans. Nevertheless, they can be used to assess the performance of other noninvasive methods such as multiple-quantum filtering. One of the most commonly used technique among those is triple-quantum-filtered (TQF) imaging (5,10–13) for which animal studies using shift reagents have shown that at least 60% of the observed TQ signal originates from intracellular sodium (14,15). The remainder of the TQ signal is probably due to interactions of sodium ions in the extracellular compartment with macromolecules.

The most frequently used TQ preparation for human imaging requires three 90° radio-frequency (RF) pulses and results in high specific absorption rates (SAR), which is problematic especially at ultra-high field strength because SAR scales approximately quadratically with the main static magnetic field (B_0). Nevertheless, high and ultra-high field scanners combined with optimized sequence parameters such as pulse duration (TD), flip angle (FA), and repetition time (TR) permit to noticeably increase the inherently low SNR of the acquired images (10). Moreover, new sequences using combinations of single-quantum and spin-density imaging with, in part, lower SAR values have been reported at 3 and 7 T (16,17).

Recently a method relying on the acquisition of two sodium images at very-short and short echo times ($TE = 0.5$ and 5 ms) and the subtraction thereof has been proposed for the quantification of motion restricted sodium (18). Compared with TQF imaging, this method leads to lower SAR and achieves higher SNR. Unfortunately, the signal from sodium nuclei with long T_2 values is only partly suppressed, which may limit the applicability of this method to high concentrations (>45 mM) of intracellular sodium. Moreover, the method is susceptible to off-resonance artefacts caused by B_0 inhomogeneities, which is problematic especially at UHF.

Inversion recovery (19–21) is another viable option to null unwanted signal from sodium ions in free motion

[1]Department for Biomedical Magnetic Resonance, University of Tübingen, Tübingen, Germany.

[2]High-Field MR Center, Max Planck Institute for Biological Cybernetics, Tübingen, Germany.

[3]Graduate School of Neural & Behavioural Sciences, University of Tübingen, Tübingen, Germany.

*Correspondence to: Christian C. Mirkes, Dipl.-Phys., High-Field MR Center, Max Planck Institute for Biological Cybernetics, Spemannstr. 41, 72076 Tuebingen, Germany. E-mail: christian.mirkes@tuebingen.mpg.de

Received 3 November 2014; revised 16 February 2015; accepted 17 February 2015

DOI 10.1002/mrm.25688

Published online 00 Month 2015 in Wiley Online Library (wileyonlinelibrary.com).

by exploiting the fact that the longitudinal relaxation times of, e.g., brain tissue and cerebrospinal fluid are different. The associated SAR can be reduced by using long rectangular inversion pulses. However, it has been shown that a more uniform fluid suppression can be achieved with adiabatic inversion pulses at the expense of a considerably higher power deposition (22). The latter would again require an increase of the repetition time and lead to a lower sensitivity (SNR per unit time).

In this study, the feasibility to acquire conventional TQF images with a state-of-the-art multi-channel phased array coil was investigated at 9.4T. Spiral and double-spiral sampling patterns were used to time-efficiently acquire spin-density weighted (SDW) and TQF images. To reduce SAR while keeping an acceptable TR for an efficient data acquisition, the FA for the TQ preparation was modulated along the partition-encoding direction. The impact of this approach on SNR and spatial resolution was evaluated by means of simulations and phantom measurements. Optimal sequence parameters were determined for in vivo imaging and used on six healthy volunteers.

METHODS

Technical Setup

All measurements were performed on a Siemens (Siemens Healthcare, Erlangen, Germany) 9.4T whole-body MRI scanner equipped with a SC72 gradient system having a maximal amplitude of 70 mT/m and a maximal slew rate of 200 T/m/s. A triple-layered proton/sodium coil was used for the acquisition of the proton (399.7 MHz) and sodium (105.7 MHz) signal (23). The innermost layer consisted of a 3D printed helmet (Dimensions: left/right 185 mm, anterior/posterior 220 mm, head/foot 200 mm) on which a 27-channel sodium receive array was constructed (Fig. 1a). The helmet was fixed inside a four-channel sodium transceiver array with a diameter of 26 cm and a length of 18 cm (Fig. 1b). The latter was used for RF transmission and the acquisition of a homogeneous reference image, which allowed estimating the sensitivity profiles of the receiver array. For anatomical localization and B_0 shimming, four dipoles tuned to the proton frequency were placed 2.5 cm above each element of the four-channel sodium array (Fig. 1b).

MRI Phantoms

Sequence performance was evaluated using an ellipsoidal-shaped MR phantom containing 16 tubes filled with aqueous solutions and agar (2.5–10%) gels of different NaCl concentrations (25–150 mM) (Fig. 1d). The gels were prepared by adding agarose crystals (Sigma-Aldrich) to aqueous solutions of sodium chloride, which were then heated in an autoclave before being poured into the tubes. Once the tubes were fixed inside the phantom, the latter was filled up with a 75 mM solution of NaCl. Another cylindrical phantom (Fig. 1e) containing a 2-cm-thick Plexiglas plate and filled with 4% agar gel and 75 mM NaCl (Slow and fast transverse relaxation times: $T^*_{2s} = 28$ ms, $T^*_{2f} = 4$ ms) was built for assessing the spatial resolution achieved by the used sampling patterns.

Imaging Sequences

A standard three-pulse preparation with flip angles FA_1, FA_2, and FA_3, and phases ϕ_1, ϕ_2, and ϕ_3 was used to generate multiple-quantum coherences (24). The basic sequence diagram is shown in Figure 2a. The TQ coherences were filtered out with a two-times-six step phase cycling scheme to allow for B_0 correction. The RF transmit and receive phases (θ) for the two sets were varied as follows (25,26):

$$\begin{aligned}
&\text{Set A}: \phi_{1,k} = \frac{\pi}{3}k,\ \phi_{2,k} = \frac{\pi}{3}k,\\
&\phi_{3,k} = 0,\ \theta_{1,k} = \phi_{1,k},\ \theta_{2,k} = \pi k,\\
&\text{Set B}: \phi_{1,k} = \frac{\pi}{2} + \frac{\pi}{3}k,\quad \phi_{2,k} = \frac{\pi}{3}k,\\
&\phi_{3,k} = 0,\ \theta_{1,k} = \phi_{1,k},\ \theta_{2,k} = \pi k,\\
&\text{for } k = 0,\ 1, \ldots 5.
\end{aligned} \qquad [1]$$

As has been shown previously (5), SDW images can be acquired during the preparation time (τ) between the first and the second RF pulse. To limit the impact of the short transverse relaxation on these images an ultra-short echo time sequence was used (24,27–29). In this study, the chosen sampling scheme consisted of a stack of spirals (1,30). The corresponding gradient waveforms were calculated with a time optimal-gradient algorithm for which a Matlab (The Mathworks, Natick, MA) and C implementation can be found online (http://www.eecs.berkeley.edu/~mlustig/) (31). All gradient moments were rewound after the end of the readout to prevent any perturbation of the TQ preparation. The second and third pulse were implemented as a single phase-modulated pulse, which avoided adding an additional delay for coil detuning and tuning. The durations of the first (TD_1) and second phase-modulated pulse ($TD_2 = TD_3 = TD_{2/3}$) could be varied independently because their values determine the amount of observable TQ signal and the associated SAR (12). A double-spiral was used to time-efficiently acquire the TQ signal with only a few spiral interleaves per partition. The number of partitions and the field-of-view (FoV) were the same as for the SDW images. The gradient waveforms were designed such that the second echo time (TE_2) coincided with the maximum of the TQ signal, which was determined as described below.

The highest TQ contrast is achieved if the flip angle of all RF pulses is 90°. However, the increased SAR at ultra-high field strength requires either a reduction of the flip angle or an increase of the pulse duration. Alternatively the TR of the sequence can be lengthened. The first two options lead to a reduced TQ contrast (10,12), while the third option results in a long and SNR-inefficient acquisition. In this study, a different approach was investigated, which consisted of reducing the flip angle toward the edge of k-space along the partition-encoding direction according to a Hann window function:

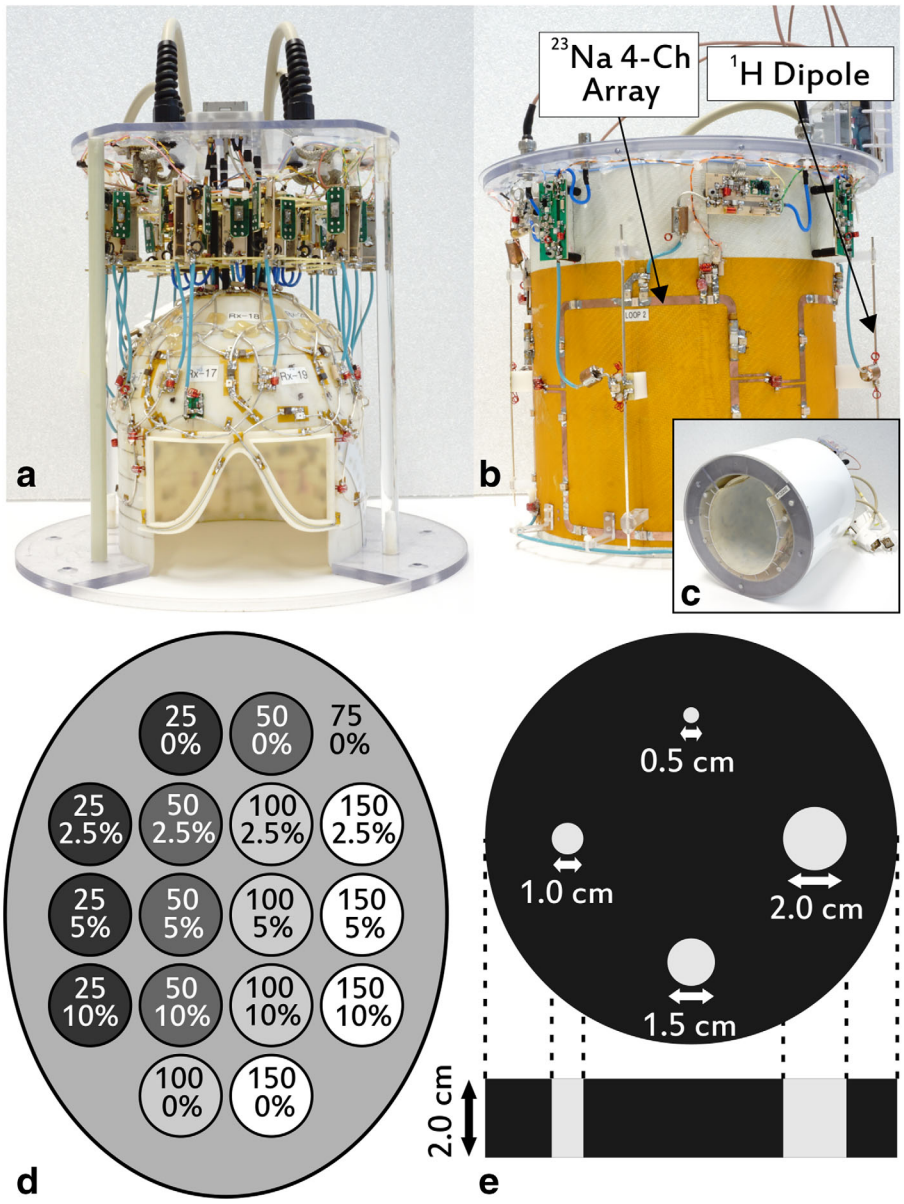

FIG. 1. **a:** Tightly fitting 27-channel sodium receiver array. **b:** Four-channel sodium transceiver array and four-channel proton dipole array. **c:** Fully assembled coil setup. **d:** Ellipsoidal-shaped MR phantom containing 16 tubes with sodium concentrations given in mM and agarose in percent. **e:** Plexiglas plate which was placed in a cylindrical phantom containing 75 mM NaCl and 4% agar to estimate the achieved resolution.

$$\alpha_{1,2,3}(p) = FA_{1,2,3}\left[\cos^2\left(\frac{\pi}{2}\left(\frac{2p}{N_{Par}} - 1\right)\right)R + (1-R)\right] \quad [2]$$
$$\text{for } p = 0 \ldots N_{Par} - 1,$$

where R controls the amount of apodization, p is the partition index, and N_{Par} the total number of partitions. As given by [2], the highest flip angle was used for the central partitions, which are most relevant for image contrast and a lower flip angle for the outer partitions (Fig. 2b). Intervals of high energy deposition were followed by periods of low RF power, which allowed staying below the prescribe SAR limit (3.2 W/kg averaged over 6 min, IEC 60601). The SDW images normally require a larger number of interleaves (N_{Int}) per partition than the TQF images due to the higher in-plane resolution. Therefore the interleaves were reordered in such a way that a smooth signal modulation was achieved for the spin density weighted images as well. To do so, the original linear reordering of the SDW acquisition was divided up into 12 segments corresponding to the 12 phase cycling steps of the TQ acquisition (Fig. 2b).

Optimal sequence parameters for the TQ preparation were determined on one human volunteer by acquiring free induction decays (FIDs) preceded by a TQ preparation with different preparation times and pulse durations. To reduce the required scanning time a 6 step phase cycling scheme was used. Further imaging parameters were: number of samples 128, readout duration (RO) 30 ms, TR 500 ms, number of τ values 40, τ range 1–20 ms, $TD_1 = TD_{2/3} = 0.7$, 1.0, 1.5, and 2.0 ms, measurement time 32 min.

B_0 shimming was performed using the proton signal and the automatic shimming interface of the scanner. The resulting B_0 field distribution was mapped with a standard 2D Cartesian double-echo gradient echo proton

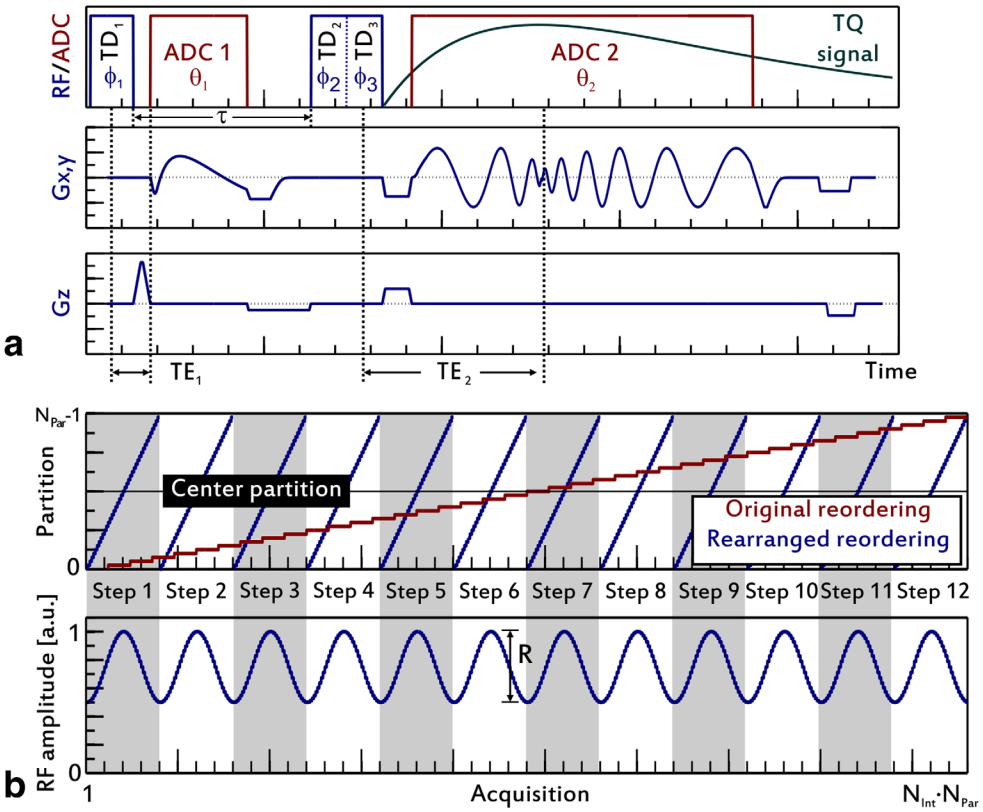

FIG. 2. **a:** Basic sequence diagram for the acquisition of SDW images (ADC 1) and TQF images (ADC 2). **b:** Reordering of the SDW spiral interleaves insuring a smooth modulation of the flip angle along the partition-encoding direction.

sequence with $TE_1 = 3.6$ ms and $TE_2 = 4.3$ ms. Other acquisition parameters were: resolution 2.0 × 2.0 × 2.5 mm^3, FoV 240 × 240 mm^2, slices 40, bandwidth 500 Hz/Pixel, and acquisition time (TA) 2 min.

The actual transmit field (B_1^+) distribution of the sodium coil was mapped with a phase sensitive method (32). It consisted of two acquisitions for which a hard 180° pulse rotating the magnetization either clock- or anticlockwise around the x-axis was followed by a 90° pulse around the y-axis. The used sampling scheme was a stack of spiral having the following imaging parameters: resolution 4 × 4 × 5 mm^3, FoV 240 mm, 44 partitions, TE 3 ms, TR 200 ms, RO 5 ms, TA 5 min. The B_1^+ map was calculated based on a B_0 map and the phase difference of the two acquisitions.

To estimate the sensitivity profile of the 27-channel array, a low resolution sodium image was acquired as a reference with both, the 4- and the 27-channel sodium array. The imaging parameters of the used stack of spirals were: resolution 5 × 5 × 5 mm^3, FoV 240 mm, 44 partitions, TE 0.3 ms, TR 80 ms, FA 50°, rectangular excitation pulse, RO 10 ms, TA 1 min.

Proton gradient echo images were acquired for anatomical localization with the following imaging parameters: slice thickness 1 mm, in-plane resolution 1 mm^2, FoV 192 × 156 mm^2, 100 slices, TE 5 ms, repetition time (TR) 2 s, nominal FA 60°, bandwidth 500 Hz/Pixel, TA 5 min.

Image Reconstruction

Image reconstruction was performed offline using a standard PC and in-house developed Matlab routines. The first step of the reconstruction pipeline consisted of a noise decorrelation of the multi-channel data to allow for an SNR optimized coil combination (33,34). The required receiver noise levels and correlations were determined by a noise prescan at the very beginning of each imaging sequence. Kaiser-Bessel gridding (35) was performed for each partition of the nonuniformly sampled data before a 3D Hanning window was applied to the resampled k-space. The individual channel images I_j were obtained by applying a 3D Fast Fourier transformation (FFT).

Coil combination was not performed with the standard sum-of-squares method because sensitivity variations of the 27-channel array would lead to large intensity variations in the combined images. Instead, sensitivity maps of the 27-channel array were obtained by dividing the individual low resolution reference coil images by the image of the 4-channel array, which was already combined on the coil. Because these maps are usually corrupted by noise, a polynomial was fitted locally on a pixel-by-pixel basis for smoothing (33). The intensity corrected images (I_{Corr}) were reconstructed based on the smoothed sensitivity maps S as given by the following equation (36):

$$I_{Corr} = \sum_{j=1}^{27} \frac{I_j \cdot S_j^*}{\sum_{i=1}^{27} S_i^* S_i}. \quad [3]$$

As has been shown previously (25), the two phase cycling sets A and B (Eq. [1]) can be combined with (Eq. [4]) or without (Eq. [5]) an ancillary B_0 map to yield B_0 corrected TQF images. For this purpose, the complex signals C_A and C_B, corresponding to the complex sums of

the signals from each phase cycling set, have to be added up according to either of the two following formulas and then fed to the image reconstruction pipeline:

$$S_{TQ} \approx \left((C_A + iC_B)e^{+i\Omega\tau_{\text{eff}}} - (C_A - iC_B)e^{-i\Omega\tau_{\text{eff}}}\right)e^{-i\Omega t} \quad [4]$$

$$S_{TQ} \approx |C_A + iC_B| + |C_A - iC_B| \quad [5]$$

where S_{TQ} is the B_0 corrected TQF signal, t is the measurement time, $\tau_{\text{eff}} = 0.5\ TD_1 + \tau + 0.5\ TD_2$ the effective preparation time and $\Omega = \omega_0 - \omega$ represents the deviation of the Larmor frequency $\omega_0 = \gamma B_0$ from the RF excitation frequency ω. In this study, Equation [5] was used to combine both phase cycling sets of all phantom and in vivo measurements without an additional B_0 map.

Point-Spread Function

The flip angle apodization acts like a filter on k-space and influences the spatial resolution along the partition-encoding direction. Therefore, the impact of the variable flip angle on the shape of the point spread function (PSF) was evaluated by simulations and phantom measurements. The PSF in case of a constant flip angle was simulated by setting a unit signal intensity for all sampling points and performing a nonuniform FFT. To estimate the shape of the PSF in case of flip angle apodization the signal for each partition was replaced by the sine of the used flip angle for the SDW images and the fifth power of the sine for the TQF images, because the TQ signal is proportional to $\sin\alpha_1 \sin^2\alpha_2 \sin^2\alpha_3$ (24). Moreover, it was assumed for the simulations that all three flip angles were $\alpha_{1,2,3}(N_{Par}/2) = FA_{1,2,3} = 90^\circ$ for the central partition irrespective of the amount of apodization. The impact of the transverse relaxation was taken into account by multiplying the SDW and TQ signals by the corresponding factor (22,24):

$$F_{SQ} = 0.6\ \exp\left(-\frac{t}{T_{2f}}\right) + 0.4\ \exp\left(-\frac{t}{T_{2s}}\right)$$
$$F_{TQ} = \exp\left(-\frac{t}{T_{2s}}\right) - \exp\left(-\frac{t}{T_{2f}}\right) \quad [6]$$

where t is the acquisition time and $T_{2\,s,f}$ are the slow and fast transverse relaxation times.

The simulations were compared with actual measurements in which the cylindrical phantom described above was imaged with different settings of the apodization factor (R=0.0, 0.25, 0.5, 0.75), while all other sequence parameters were left unchanged: TR 150 ms, resolution 4 × 4 × 3 mm^3, 64 partitions, 4 averages, τ 11.8 ms, TD_1 1.5 ms, $TD_{2/3}$ 1.5 ms, $FA_{1,2,3}$ 90°, 2 × 6 phase cycling steps and TA 77 min.

Signal-to-Noise Ratio

The flip angle apodization factor represents an additional degree of freedom and hence its value influences the optimal choice for the other imaging parameters. To reduce the optimization domain, several parameters were either linked to one another or fixed to practical values. As has been shown previously (12), the B_0-inhomogeneity correction (Eq. [1] and [4]) performs only well if the RF pulses are short. Therefore TD_1 and $TD_{2/3}$ were fixed to 1.5 ms and 1.0 ms, respectively. Moreover, the flip angle of the second and third pulse were constrained to have always identical values ($FA_2 = FA_3 = FA_{2/3}$). The simulations were performed for R values ranging from 0 to 1 and repetition times spanning from 150 to 300 ms. Owing to the long TR, saturation effects could be neglected. The impact of different transverse relaxation times was not investigated either. Under these assumptions the theoretical SNR can be easily estimated for a simulated object. The analytical phantom used in the study was a cube, whose representation in k-space is given by:

$$Cube(k_x, k_y, k_z) = \text{sinc}\ ak_x \cdot \text{sinc}\ ak_y \cdot \text{sinc}\ ak_z \quad [7]$$

where k_x, k_y and k_z are the k-space coordinates of the sampling points and a=10 cm is the edge length of the cube. Optimal values for FA_1 and $FA_{2/3}$ for a given repetition time and apodization factor were determined by maximizing the value of $\sin FA_1 \sin FA_{2/3}{}^4$ while staying below the prescribed SAR limit. Similar to the PSF simulations described above, the synthetic signal of the cube was multiplied with the partition-dependent scaling factor $\sin\alpha_1 \sin\alpha_{2/3}{}^4$ and fed to the image reconstruction algorithm, which included the same k-space filters as used for the real measurements. Using the signal intensity (S) from the reconstructed image and the full width at half maximum (FWHM) along the partition-encoding direction of the additionally simulated PSF, the sensitivity (SNR per unit time) for a given set of parameters can be calculated as follows:

$$\text{Sensitivity(R, TR)} \propto \frac{S}{FWHM_{\text{PSF}} \cdot \sqrt{TR}}\ . \quad [8]$$

The ellipsoidal phantom was scanned with four different apodization factors and a fixed TR of 200 ms to assess the resulting SNR and to compare it with the theoretical expectation. The used sequence parameters for the simulation and the experiment were: TE_1 0.4 ms, τ 13 ms, TE_2 11 ms, 44 partitions, TA 60 min, and nominal resolution $1.5 \times 1.5 \times 5.0$ mm^3 (SDW) and 4 × 4 × 5 mm^3 (TQF). Because the optimal values for FA_1 and $FA_{2/3}$ predicted by the simulation were almost identical, the same flip angle was used for all three RF pulses in the experiment. SNR maps were generated based on a pseudo multiple replica approach (37). A prescan was performed to acquire noise samples from each coil element and estimate the noise standard deviation and correlation. Synthetic correlated noise was generated and added to the k-space of a standard SDW/TQF image acquisition. Once the image was reconstructed, the process was repeated with a new set of synthetic noise. The standard deviation for each pixel value through a stack of 100 replicas was calculated and used to generate SNR maps.

In Vivo Measurements

The study was approved by the local ethics committee (University of Tuebingen). Each of the six participating

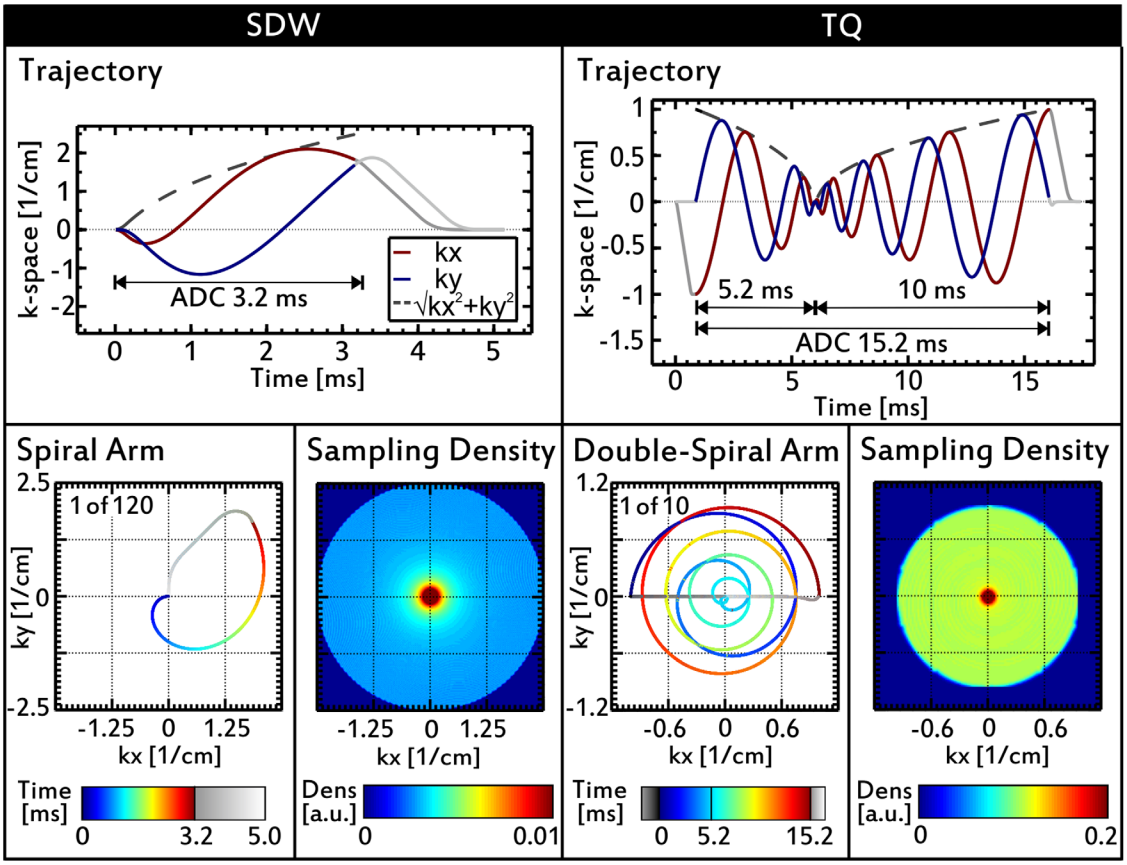

FIG. 3. One- and two-dimensional representations of the used k-space trajectory for the SDW and TQF in vivo images and the corresponding durations. The normalized sampling density is shown to assess the achieved homogeneity of the sampling pattern.

healthy subjects (mean age: 31 years) provided written informed consent before the MR examination. The optimal preparation time ($\tau = 5.5$ *ms*) and RF pulse durations ($TD_1 = 1.5$ ms and $TD_{2/3} = 1.0$ ms) were determined in one volunteer and used for all in vivo measurements. Imaging parameters making full use of the available time between the first and the second RF pulse were chosen for the SDW acquisition: nominal resolution $2 \times 2 \times 5$ mm^3, TE_1 0.8 ms, RO 3.2 ms, FoV 250 mm^2, 52 partitions, 120 spiral interleaves per partition, and 1 average. The nominal resolution of the TQ images was $5 \times 5 \times 5$ mm^3 and 10 double-spiral interleaves per partition were used. Based on the optimization results described below and the chosen values for τ and $TD_{1,2}$ the optimal value for TE_2 was 6.5 ms, which is close to the expected value of $TE_{2,\mathrm{exp}} = 0.5\ TD_1 + \tau + 0.5\ TD_2 = 6.75$ ms. The total readout duration for the TQF images was 15.2 ms of which 5.2 ms were spent to sample the signal before the formation of the TQ signal peak. One- and two-dimensional representations of the k-space trajectories used for the acquisition of the SDW and TQF images are shown in Figure 3. Both trajectories were designed to create a uniform k-space sampling density apart from the k-space center, which is highly oversampled due to the center-out acquisition. The corresponding normalized sampling densities are depicted Figure 3 as well. The total acquisition time for 12 phase cycling steps was 21 min using a TR of 200 ms.

RESULTS

PSF and Resolution

Figure 4 shows the simulated increase of the FWHM of the PSF along the partition-encoding direction as a function of the apodization factor for the SDW and TQF images. The measured data points indicated by circles (SDW) and triangles (TQF) represent the increase of FWHM of the second smallest hole (1 cm in diameter) in the plate. The smallest hole (0.5 cm in diameter) was broadened too much by the transverse relaxation and the image filter to be evaluated. Due to the stronger dependence of the TQ signal on the flip angle, the decrease in resolution is more pronounced for the TQF than the SDW images but still below 20% for $R = 0.5$.

Signal-to-Noise Ratio

The optimal flip angles FA_1 and $FA_{2/3}$ as a function of R and TR are shown in Figures 5a and 5b. They deviate only by a few degrees from each other at most. However, the flip angle of the first RF pulse is consistently smaller than the other ones. Once the choice of flip angles is not limited by SAR constraints any more, the optimal flip

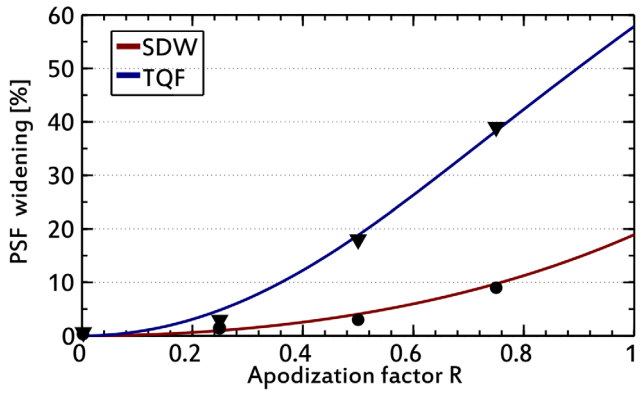

FIG. 4. Simulated PSF widening for the SDW and TQF images (red and blue lines) as a function of the apodization factor. The measured data points are indicated by circles (SDW) and triangles (TQF).

angle amounts to 90° as expected. As can be seen in Figure 5c, the width of the PSF for the TQF acquisition depends slightly on the flip angles. Moreover, even without flip angle apodization the resulting spatial resolution of the TQF images in partition-encoding direction is below its nominal value (5 mm). The reason for this is primarily the Hanning filter which was applied to k-space. Figure 5d demonstrates that a higher sensitivity compared to the standard acquisition (R = 0) can be achieved for each value of TR if flip angle apodization is used. The sensitivity for SDW acquisition shows a different behavior and exhibits a much smaller dependence on the amount of apodization (data not shown).

Figures 6a and 6b show SNR maps of the ellipsoidal phantom for the SDW and TQF acquisition, respectively. A region of interest (ROI) in the tube exhibiting the highest TQ signal was selected and the corresponding value is stated below each image. As predicted by the simulation, the highest SNR among the chosen apodization factors is achieved for R = 0.5. Compared with the standard acquisition (R = 0) there is an increase of 39% in SNR. However, this increase in SNR is partly due to the larger voxel size of approximately 20% in partition-encoding direction. If the measured SNR values are divided by the simulated FWHM, the obtained sensitivity exhibits a similar behavior with respect to the apodization factor as the simulated sensitivity. The original TQF images are shown in Figure 6c to demonstrate that signal from sodium ions in free motion is successfully suppressed irrespective of the amount of flip angle apodization used.

In Vivo Measurements

The normalized in vivo TQ signal intensity for 16 combinations of different TD_1 and $TD_{2/3}$ values is depicted in Figure 7a. The relative SAR values can be easily deduced from the pulse durations and are indicated in the figure as well:

$$\mathrm{SAR} \propto \frac{1}{TD_1} + \frac{2}{TD_{2/3}}, \qquad [9]$$

knowing that the flip angles used for the TQ preparation are the same for all pulses. If the maximal SAR value is not reached for a given set of pulse durations, then the sensitivity can be increased by reducing the TR accordingly. Assuming that the used TRs are not much shorter than five times the longitudinal relaxation time (≈150 ms for tissue) and that saturation effects are as a matter of fact negligible, optimal values for τ, TD, and TE_2 can be determined based on the normalized TQ signal intensity divided by the square root of the minimal TR still fulfilling the SAR constraints (Fig. 7b). However, long RF pulses reduce the effectiveness of the B_0 correction (12) and consequently compromise image quality. In this study, TD_1 and $TD_{2/3}$ were set for in vivo imaging to 1.5 ms and 1.0 ms, respectively, to satisfy both requirements. The optimal τ for this set of parameters was approximately 5.5 ms, which is identical to the value found in earlier studies at 3T and 4.7T (10,24). This value was used for all following in vivo measurements.

Figures 8a and 8c show SDW images acquired without (R = 0) and with (R = 0.5) flip angle apodization in one volunteer. Owing to the high in-plane resolution, fine anatomical details such as the cerebrospinal fluid-filled sulci can be discerned. The images have been corrected for B_1 inhomogeneities by dividing each pixel value by

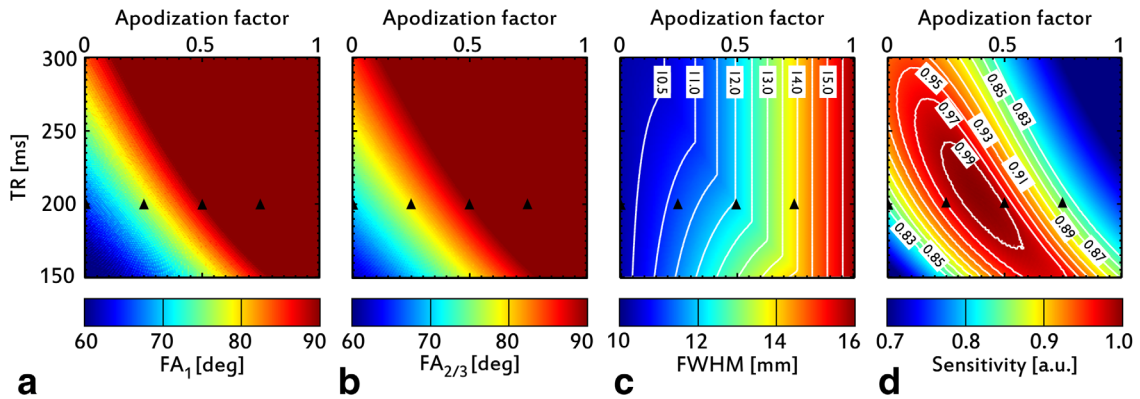

FIG. 5. **a:** Optimal flip angle for the first RF pulse. **b:** Optimal flip angle for the second and third RF pulse. **c:** FWHM along the partition-encoding direction of the PSF for the TQF acquisition. **d:** Sensitivity plot for the TQF acquisition. (The triangles indicate the chosen parameter values for the SNR measurements of Fig. 6.)

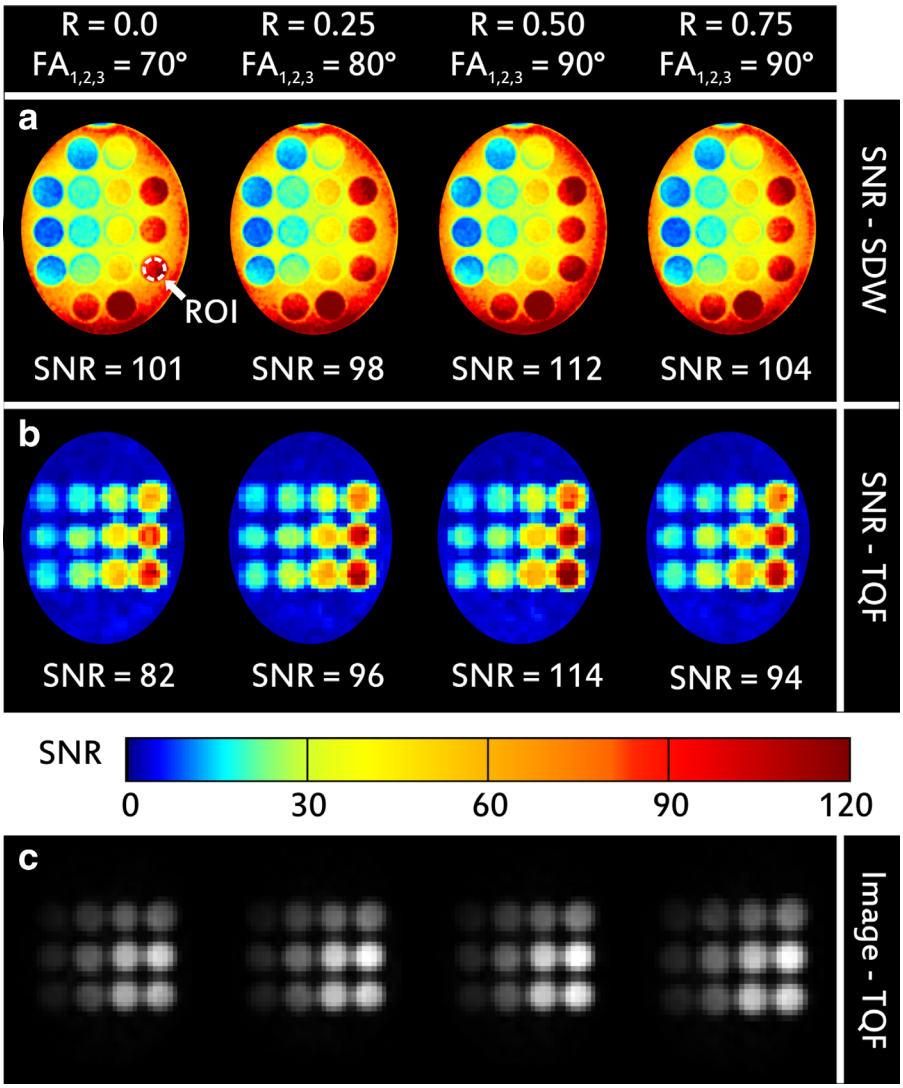

FIG. 6. SNR maps of the ellipsoidal phantom for different apodization factors. The SNR of the chosen ROI is indicated below each image for the SDW (**a**) and TQF (**b**) acquisition. The signal of the saline solution is suppressed irrespective of the used amount of flip angle apodization as demonstrated by the original TQF images (**c**). The nominal resolution of the images was 1.5 × 1.5 × 5.0 mm^3 (SDW) and 4 × 4 × 5 mm^3 (TQF), respectively.

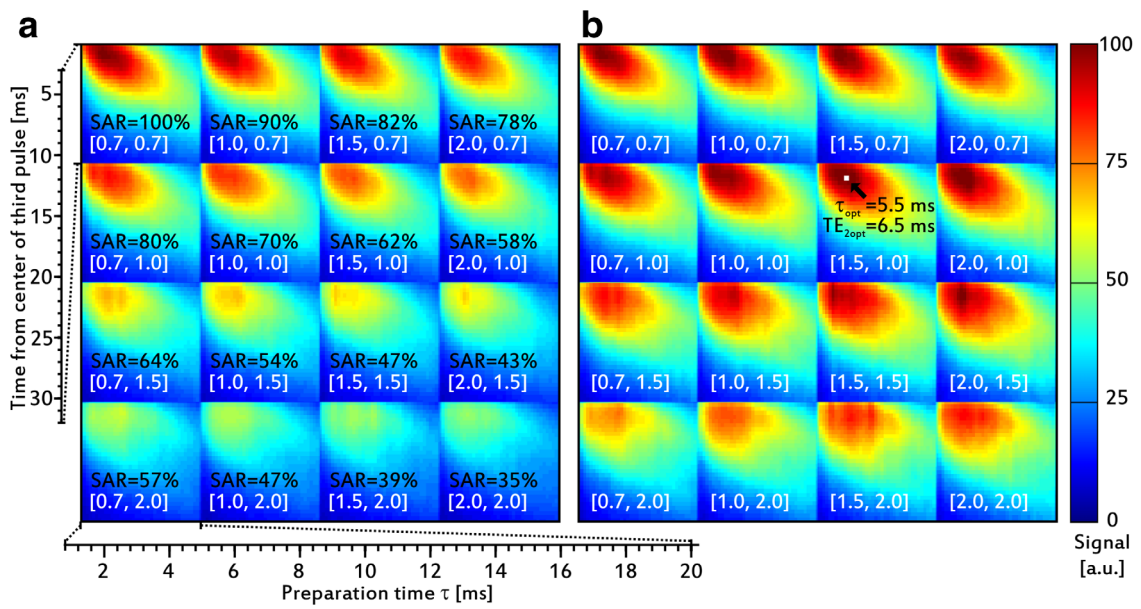

FIG. 7. In vivo sequence parameter optimization. **a:** Each subimage represents the normalized TQ signal intensity for one set of FIDs for a given value of TD_1 and $TD_{2/3}$ (indicated in square brackets). **b:** Sensitivity plots obtained by dividing the signal intensity from (a) by the square root of the minimal TR still fulfilling the SAR constraints. The used preparation and echo time for the in vivo measurements are indicated by a white square.

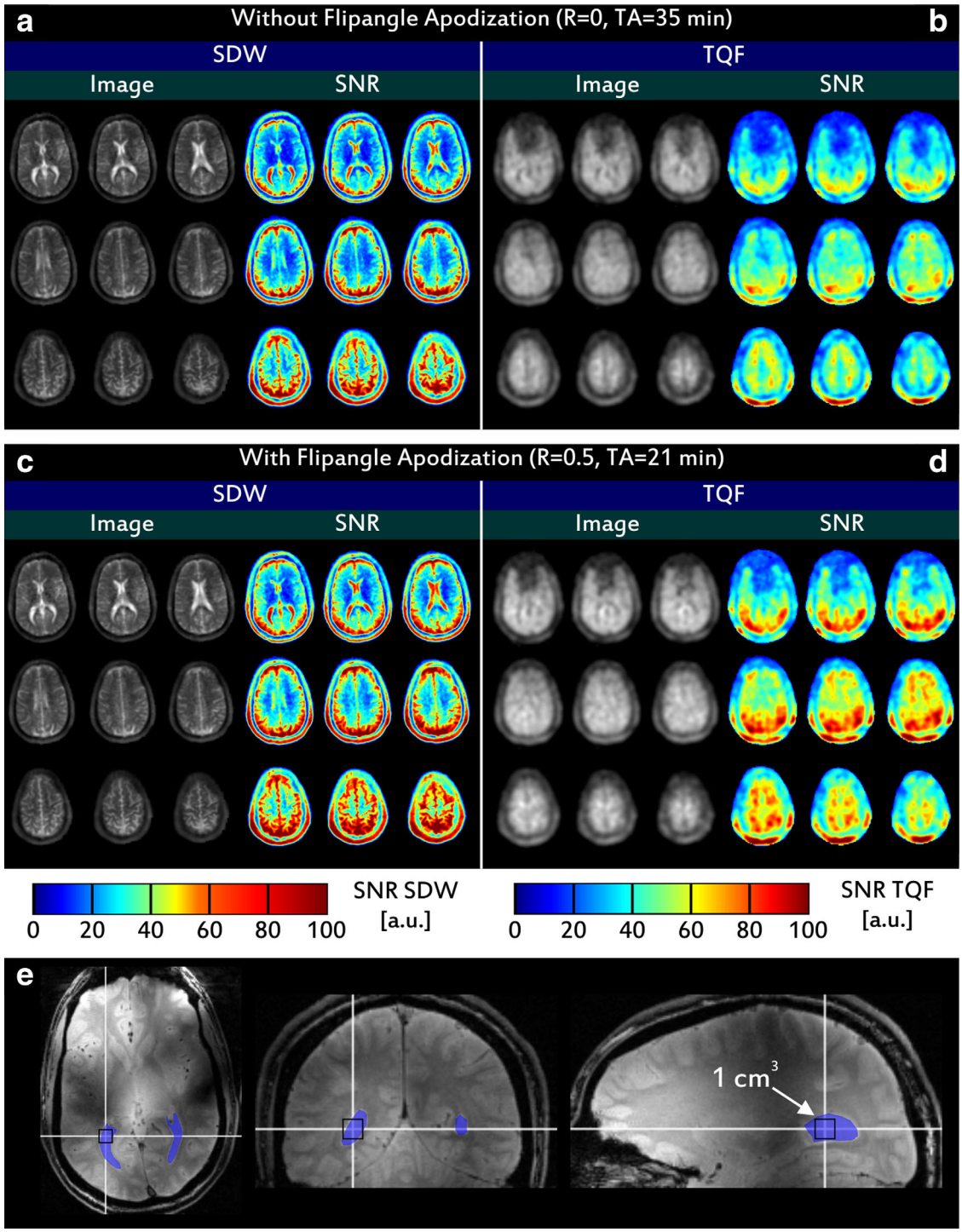

FIG. 8. **a:** SDW (**a,c**) and TQF (**b,d**) images with a nominal resolution of $2 \times 2 \times 5$ mm^3 and $5 \times 5 \times 5$ mm^3, respectively, and corresponding SNR maps of a healthy human volunteer after receive sensitivity and B_1 correction for $R = 0$ (**a,b**) and $R = 0.5$ (**c,d**). For easy comparison, the shown SNR maps have been scaled by the square root of the measurement time. Flip angle apodization resulted in a 20% and 32% increase in SNR for the SDW and TQF images, respectively. The ventricles (colored overlay in **e**) are not fully suppressed in the TQF images, which is probably due to their small size compared to the actual voxel size.

the sine of the achieved flip angle. The intensity correction (Eq. [3]) permitted to successfully eliminate the signal modulation caused by the inhomogeneous receive profile of the 27-channel sodium array. However, the reduced sensitivity of the array in the center of the brain led to a slight but still acceptable noise enhancement in that area. The repetition time for $R = 0$ had to be increased from 200 ms to 340 ms to stay below the allowed SAR limits, which increased the measurement time from 21 min to 35 min. All SNR maps shown in Figure 8 have been divided by the square root of the needed measurement time to allow for a fair comparison.

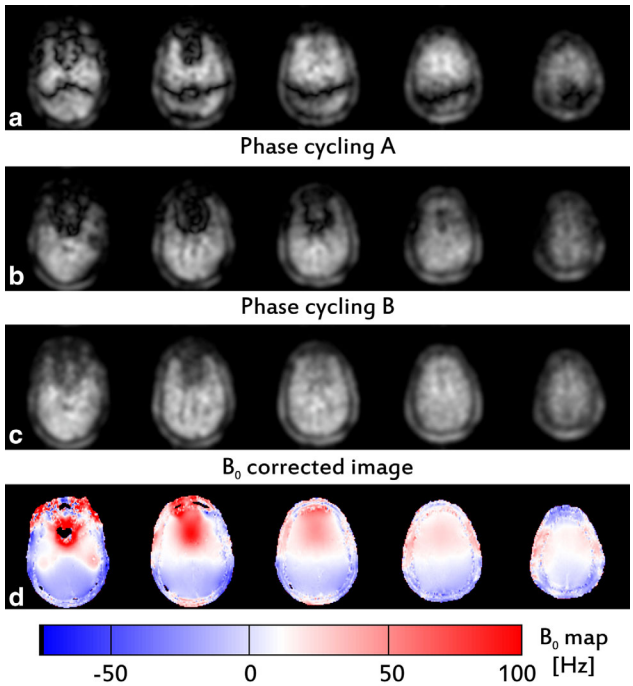

FIG. 9. Effectiveness of the B_0 correction. The two phase cycling sets A and B (**a,b**) were combined (Eq. [5]) to yield a B_0 corrected image (**c**) of improved quality. The B_0 map (**d**) is shown for reference but was not used for the combination of the two phase cycling sets.

As for the phantom measurements, a higher SNR (~20%) was achieved by using flip angle apodization.

The corresponding TQ images are shown in Figures 8b and 8d. Again, a higher SNR (~32%) was obtained by modulating the flip angle along the partition-encoding direction. In contrast to the SDW acquisition, the TQF images exhibit a much lower spatial resolution. The coarse nominal resolution is further reduced by the image filter, the usage of the flip angle apodization and/or the transverse relaxation of the received signal. Based on the phantom measurements and simulations, the nominal resolution can be inferred to be at least twice as large in each spatial direction compared with the nominal resolution. As a matter of fact, the expected signal dropouts in the ventricles are less pronounced due to partial volume effects. For reference, a proton gradient echo image with the ventricles highlighted is shown in Figure 8e. The outline of a voxel with a volume of 1 cm^3 in the inferior horn of the lateral ventricle, where the ventricular system is broadest for the shown subject, has been added to the figure to assess the proportions.

Signal dropouts near the nasal cavities could not be avoided even with B_0 correction. Nevertheless, it is still worthwhile to acquire 12 phase cycling steps at 9.4T as demonstrated by Figure 9. Figures 9a and 9b show images corresponding to the two phase cycling sets A and B. The complementary nature of the two phase cycling schemes allowed to generate a B_0 corrected image (Fig. 9c) of improved quality. However, signals from areas with pronounced magnetic field offsets (Fig. 9d) could not be recovered.

DISCUSSION AND CONCLUSIONS

This study has shown that it is possible to acquire B_0 corrected TQF images at 9.4T in a clinically acceptable measurement time of 21 min. To reduce the time needed to sample the entire k-space, a highly efficient double-spiral trajectory was used instead of a Cartesian or radial readout. For the same resolution and FoV, Cartesian imaging would have required 50 instead of 10 excitations per partition. This number could be reduced by using elliptical scanning (−25%) and/or partial Fourier encoding. Additionally, the double-spiral readout permitted to acquire data even before the delayed formation of the TQ signal peak, which would have been lost in case of a radial readout as used in previous studies (10,24,26). Due to the high field strength and the sensitive 27-channel coil array, images with acceptable SNR could be acquired in the prescribed measurement time. Prohibitively long TRs enforced by stringent SAR constraints were avoided by modulating the flip angles of the TQ preparation along the partition-encoding direction. The reduction of the TR permitted improving the sensitivity and efficiency of the SDW/TQF acquisition as demonstrated by the simulations. However, the nominal spatial resolution along the partition-encoding direction and the number of partitions might have to be increased to compensate for the broadening of the PSF due to the flip angle apodization. Doing so would again prolong the time needed to cover the entire k-space. The actual final resolution of the in vivo images is difficult to assess quantitatively but will be at least two times larger in each spatial direction due to the transverse relaxation, the used sampling pattern, the image filter, and the flip angle apodization. The current implementation of the sequence only allowed using the same number of partitions for the SDW and TQF images. However, the reordering of the SDW acquisition could be easily modified to allow for more partitions to be used while still ensuring a smooth signal modulation of k-space.

For the SNR evaluation, the impact of the sampling pattern and density were not considered. A homogenous sampling pattern was chosen for the both, the SDW and TQF images. Based on previous studies (38,39), the SNR could be increased further by directly integrating the image filter into the then inhomogeneous sampling pattern. Note that the flip angle apodization only changes the weighting of the NMR signal and does not affect the noise variance associated with each data sample.

Due to the low spatial resolution, TQF allows to discriminate only large anatomical structures even at 9.4T. If desired some of the SNR could be traded for higher spatial resolution, which could be achieved to a certain extent even without having to increase the number of spiral interleaves. The usefulness of the proposed flip angle apodization was only demonstrated for the standard TQF method but it could also be easily applied to other imaging schemes such as the phase-cycling difference image method (pcDIM) (16,17).

Air-tissue interfaces above the ear canals and nasal cavities cause large magnetic field offsets and are a serious problem at UHF for conventional TQF but also for the pcDIM or the double echo method. As demonstrated

above, an off-resonance correction is required to reduce at least partly signal dropouts in the affected areas. Although a B_0 map was acquired for each subject, it was not used for the combination of the two phase cycling sets (Eq. [4]) because it added artifacts at the periphery of the brain without improving image quality.

The SDW images were acquired with a short TE_1 and are consequently only slightly affected by the transverse relaxation. However, for the creation of tissue sodium concentration maps it would be advisable to use TEs shorter than 0.5 ms. Reducing the flip angle of the TQ preparation by a few degrees and accepting a slight decrease in SNR would permit reducing the duration of the first RF pulse sufficiently to achieve this goal. The latter was not done in this study because the main objective was to maximize the SNR of the TQ images.

In summary, TQF imaging at UHF suffers from the same shortcomings as known from low and high field MRI such as inherently low SNR, low spatial resolution, high SAR, marked susceptibility to off-resonance artefacts, and long measurements times. However, some of these issues could be mitigated to a certain extent, as demonstrated in this study, by reducing the flip angle of the TQ preparation along the partition-encoding direction and applying an off-resonance correction. Moreover, the application of the proposed method in tumor patients would be valuable future work. Even tough, it will not be possible to detect small pathologies given the achievable resolution, TQF imaging at 9.4T might still be useful on a slightly larger scale and provide additional information compared with conventional imaging techniques.

ACKNOWLEDGMENTS

This work was funded in part by the Helmholtz Alliance ICEMED – Imaging and Curing Environmental Metabolic Diseases, through the Initiative and Networking Fund of the Helmholtz Association.

REFERENCES

1. Mirkes CC, Hoffmann J, Shajan G, Pohmann R, Scheffler K. High-resolution quantitative sodium imaging at 9.4 Tesla. Magn Reson Med 2015;73:342–351.
2. Ouwerkerk R. Socium MRI. Methods Mol Biol 2011;711:175–201.
3. Rooney WD, Springer CS. A comprehensive approach to the analysis and interpretation of the resonances of spins 3/2 from living systems. NMR Biomed 1991;4:209–226.
4. Borthakur A, Hancu I, Boada FE, Shen GX, Shapiro EM, Reddy R. In vivo triple quantum filtered twisted projection sodium MRI of human articular cartilage. J Magn Reson 1999;141:286–290.
5. Fiege DP, Romanzetti S, Mirkes CC, Brenner D, Shah NJ. Simultaneous single-quantum and triple-quantum-filtered MRI of 23Na (SISTINA). Magn Reson Med 2013;69:1691–1696.
6. Boada FE, Laverde G, Jungreis C, Nemoto E, Tanase C. Triple/single qantum filtered sodium MRI of acute brain ischemia. In Proceedings of the 27th Annual IEEE Engineering in Medicine and Biology Conference, Shanghai, China. 2005. p 731–734.
7. Gupta RK, Gupta P. Direct observation of resolved resonances from intra- and extracellular sodium-23 ions in NMR studies of intact cells and tissues using dysprosium(III)tripolyphosphate as paramagnetic shift reagent. J Magn Reson 1982;47:344–350.
8. Winter PM, Bansal N. TmDOTP5 – as a 23Na shift reagent for the subcutaneously implanted 9L gliosarcoma in rats. Magn Reson Med 2001;45:436–442.
9. Dizon JM, Tauskela JS, Wise D, Burkhoff D, Cannon PJ, Katz J. Evaluation of triple-quantum-filtered 23Na NMR in monitoring of intracellular Na content in the perfused rat heart: comparison of intra- and extracellular transverse relaxation and spectral amplitudes. Magn Reson Med 1996;35:336–345.
10. Tsang A, Stobbe RW, Beaulieu C. Triple-quantum-filtered sodium imaging of the human brain at 4.7 T. Magn Reson Med 2012;67:1633–1643.
11. Tanase C, Boada FE. Triple-quantum-filtered imaging of sodium in presence of B(0) inhomogeneities. J Magn Reson 2005;174:270–278.
12. Tsang A, Stobbe RW, Beaulieu C. Evaluation of B0-inhomogeneity correction for triple-quantum-filtered sodium MRI of the human brain at 4.7 T. J Magn Reson 2013;230:134–144.
13. Hancu I, van der Maarel JR, Boada FE. A model for the dynamics of spins 3/2 in biological media: signal loss during radiofrequency excitation in triple-quantum-filtered sodium MRI. J Magn Reson 2000; 147:179–191.
14. Winter PM, Bansal N. Triple-quantum-filtered 23Na NMR spectroscopy of subcutaneously implanted 9L gliosarcoma in the rat in the presence of TmDOTP5. J Magn Reson 2001;152:70–78.
15. Seshan V, Sherry AD, Bansal N. Evaluation of triple quantum 23Na NMR spectroscopy in the in situ rat liver. Magn Reson Med 1997;38: 821–827.
16. Benkhedah N, Bachert P, Semmler W, Nagel AM. Three-dimensional biexponential weighted 23Na imaging of the human brain with higher SNR and shorter acquisition time. Magn Reson Med 2012;765: 754–765.
17. Benkhedah N, Bachert P, Nagel AM. Two-pulse biexponential-weighted 23Na imaging. J Magn Reson 2014;240:67–76.
18. Qian Y, Panigrahy A, Laymon CM, Lee VK, Drappatz J, Lieberman FS, Boada FE, Mountz JM. Short-T2 imaging for quantifying concentration of sodium (23Na) of bi-exponential T2 relaxation. Magn Reson Med 2014. doi: 10.1002/mrm.25393.
19. Stobbe R, Beaulieu C. In vivo sodium magnetic resonance imaging of the human brain using soft inversion recovery fluid attenuation. Magn Reson Med 2005;54:1305–1310.
20. Kline RP, Wu EX, Petrylak DP, Szabolcs M, Alderson PO, Weisfeldt ML, Cannon P, Katz J. Rapid in vivo monitoring of chemotherapeutic response using weighted sodium magnetic resonance imaging. Clin Cancer Res 2000;6:2146–2156.
21. Nagel AM, Bock M, Hartmann C, et al. The potential of relaxation-weighted sodium magnetic resonance imaging as demonstrated on brain tumors. Invest Radiol 2011;46:539–547.
22. Madelin G, Lee J-S, Inati S, Jerschow A, Regatte RR. Sodium inversion recovery MRI of the knee joint in vivo at 7T. J Magn Reson 2010;207:42–52.
23. Shajan G, Mirkes C, Buckenmaier K, Hoffmann J, Pohmann R, Scheffler K. Three-layered radiofrequency coil arrangement for sodium MRI of the human brain at 9.4 Tesla. Magn Reson Med. doi: 10.1002/mrm.25666.
24. Hancu I, Boada FE, Shen GX. Three-dimensional triple-quantum-filtered 23Na imaging of in vivo human brain. Magn Reson Med 1999;42:1146–1154.
25. Fleysher L, Oesingmann N, Inglese M. B0 inhomogeneity-insensitive triple-quantum-filtered sodium imaging using a 12-step phase-cycling scheme. NMR Biomed 2010;23:1191–1198.
26. Matthies C, Nagel AM, Schad LR, Bachert P. Reduction of B(0) inhomogeneity effects in triple-quantum-filtered sodium imaging. J Magn Reson 2010;202:239–244.
27. Qian Y, Zhao T, Zheng H, Weimer J, Boada FE. High-resolution sodium imaging of human brain at 7 T. Magn Reson Med 2012;68:227–233.
28. Nagel AM, Laun FB, Weber M-A, Matthies C, Semmler W, Schad LR. Sodium MRI using a density-adapted 3D radial acquisition technique. Magn Reson Med 2009;62:1565–1573.
29. Romanzetti S, Mirkes CC, Fiege DP, Celik A, Felder J, Shah NJ. Mapping tissue sodium concentration in the human brain: a comparison of MR sequences at 9.4Tesla. Neuroimage 2014;96:44–53.
30. Qian Y, Zhao T, Zheng H, Weimer J, Boada FE. High-resolution sodium imaging of human brain at 7 T. Magn Reson Med 2012;68:227–233.
31. Lustig M, Kim S-J, Pauly JM. A fast method for designing time-optimal gradient waveforms for arbitrary k-space trajectories. IEEE Trans Med Imaging 2008;27:866–873.
32. Allen SP, Morrell GR, Peterson B, Park D, Gold GE, Kaggie JD, Bangerter NK. Phase-sensitive sodium B1 mapping. Magn Reson Med 2011;65:1125–1130.

33. Pruessmann KP, Weiger M, Scheidegger MB, Boesiger P. SENSE: sensitivity encoding for fast MRI. Magn Reson Med 1999;42:952–962.
34. Roemer PB, Edelstein WA, Hayes CE, Souza SP, Mueller OM. The NMR phased array. Magn Reson Med 1990;16:192–225.
35. Jackson JI, Meyer CH, Nishimura DG, Macovski A. Selection of a convolution function for Fourier inversion using gridding. IEEE Trans Med Imaging 1991;10:473–478.
36. Larsson EG, Erdogmus D, Yan R, Principe JC, Fitzsimmons JR. SNR-optimality of sum-of-squares reconstruction for phased-array magnetic resonance imaging. J Magn Reson 2003;163:121–123.
37. Robson PM, Grant AK, Madhuranthakam AJ, Lattanzi R, Sodickson DK, McKenzie CA. Comprehensive quantification of signal-to-noise ratio and g-factor for image-based and k-space-based parallel imaging reconstructions. Magn Reson Med 2008;60:895–907.
38. Stobbe R, Beaulieu C. Advantage of sampling density weighted apodization over postacquisition filtering apodization for sodium MRI of the human brain. Magn Reson Med 2008;60:981–986.
39. Konstandin S, Nagel AM. Performance of sampling density-weighted and postfiltered density-adapted projection reconstruction in sodium magnetic resonance imaging. Magn Reson Med 2013;69:495–502.